National Technical University of Athens
School of Civil Engineering
Geotechnical Division

Εθνικό Μετσόβιο Πολυτεχνείο
Σχολή Πολιτικών Μηχανικών
Τομέας Γεωτεχνικής

Diploma Thesis by

Dimitrios Aidinis

Supervised by

N. Gerolymos

SEISMIC FRAGILITY ANALYSIS OF MULTI-BLOCK GRAVITY QUAY WALLS: APPLICATION TO PIRAEUS PORT

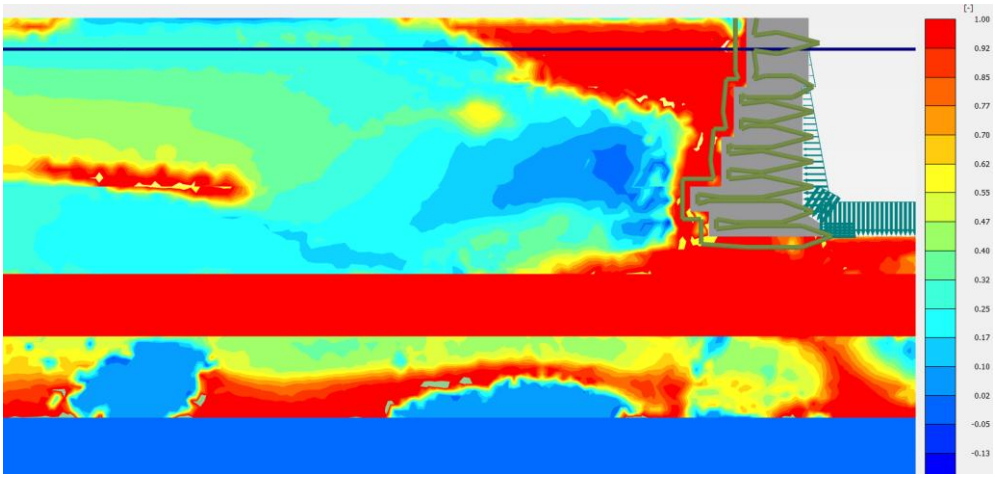

ΑΝΑΛΥΣΗ ΣΕΙΣΜΙΚΗΣ ΤΡΩΤΟΤΗΤΑΣ ΛΙΜΕΝΙΚΟΥ ΚΡΗΠΙΔΟΤΟΙΧΟΥ ΠΟΛΛΑΠΛΩΝ ΤΕΜΑΧΩΝ : ΕΦΑΡΜΟΓΗ ΣΤΟ ΛΙΜΑΝΙ ΤΟΥ ΠΕΙΡΑΙΑ

Διπλωματική Εργασία

Δημητρίου Αϊδίνη

Επιβλέπων

Ν. Γερόλυμος

Νοέμβριος 2015

Acknowledgements

To begin with, I would like to express my sincere gratitude to my supervisor, Assistant Professor N. Gerolymos, who appointed me to undertake this noteworthy diploma thesis and whose guidance, motivation and profound knowledge provided me with the appropriate experience to complete it successfully.

Besides my supervisor, I would like to thank Professor G. Gazetas for his inspirational teaching of Geotechnical Engineering, during my undergraduate years, which arguably has transmitted me the passion and interest for this magnificent section of Engineering.

Last but not the least, I would like to thank my family, my colleagues and my friends for supporting me throughout my academic path.

Table of Contents

1. Introduction 7
1.1 Gravity Quay Walls in seismic incidents 7
1.2 Scope 11
2. Aspects of Earthquake engineering 15
2.1 Type of Dynamic Loading on Soils 15
2.1.1 Intoduction 15
2.1.2 Ground vibration 19
2.1.3 Response Spectrum Analysis 23
2.2 Liquefaction 28
2.2.1 *Introduction* 28
2.2.2 Fundamental Concept of Liquefaction 29
2.2.3 Laboratory Studies to Simulate Field Conditions for Soil Liquefaction 31
2.2.4 Cyclic Simple Shear Test 32
2.2.5 Zone of Initial Liquefaction in the Field 37
2.2.6 Liquefaction Analysis from Standard Penetration Resistance 38
2.3 Interaction of Soil and caisson quay wall 43
2.3.1 Mononobe-Okabe Active Earth Pressure Theory 43
2.3.2 Effective Stress Numerical Analysis 48
2.4 Fragility Curves 53
2.4.1 Fragility definition 53
2.4.2 Fragility criteria for Quay Walls 54
3. Numerical Modeling 57
3.1 Finite Element Program 57
3.2 Boundaries 67
3.3 Constitutive Model 73
3.3.1 UBCSAND 73
3.3.2 Parameters 77
3.3.3 Undrained behavior 79
3.3.4 Rayleigh 81
3.4 Interfaces 82
3.4.1 Interfaces between the blocks of the quay wall 82

3.4.2 Interfaces at the back and the base of the quay wall 82
3.4.3 Interfaces on the frontage of the quay wall 84
4. Quay wall at Piraeus Port.....88
4.1 Geometry – Profile.....88
4.2 Input values.....91
4.2.1 Material properties.....91
4.2.2 Parameters.....91
5. Excitation.....99
5.1 Input excitations.....101
5.2 Reduction of excitations.....106
5.3 Direction of base excitation.....108
6. Numerical results.....113
6.1 Fragility Curves.....113
6.1.1 Introduction.....113
6.1.2 Fragility curves according to PIANC criteria.....114
6.1.2.1 Backfill soil with Dr=40%.....114
6.1.2.2 Backfill soil with Dr=65%.....115
6.1.2.3 Backfill soil with Dr=80%.....117
6.1.3 Fragility Curves with lower fragility levels.....118
6.1.3.1 Backfill soil with Dr=40%.....118
6.1.3.2 Backfill soil with Dr=65%.....119
6.1.3.3 Backfill soil with Dr=80%.....121
6.2 Results of dynamic analysis and discussion.....122
6.2.1 Displacements.....122
6.2.2 Influence of Relative Density.....126
6.2.4 Influence of excitation.....130
6.3 General notes 134
6.3.1 Influence of boundaries' type.....134
6.3.2 Quay wall's tilt for dense backfill soil..... 136
7. Conclusion..... 139
References.....140

Chapter 1

Introduction

1.1 Gravity Quay Walls in seismic incidents

Watching and analyzing the devastating effects on constructions of Civil Engineers, which large earthquakes caused during the preceding decades, it could be easily noticed that there have been many cases of failure of gravity quay walls. These failures are often associated with significant horizontal spreading of liquefiable soil deposits.

Gravity quay walls are the most common type of construction for docks because of their durability, ease of construction and capacity to reach deep seabed levels. The design of gravity quay walls requires sufficient capacity for three design criteria; sliding, overturning and allowable bearing stress under the base of the wall. Although the design of gravity quay walls is reasonably well understood for static loads, analysis under seismic loads is still being developed. Throughout strong ground shaking, the pore water pressure of cohesionless saturated soils builds up. This increase in pressure not only causes the lateral forces on the walls to increase, but also reduces the effective stress of the soil foundation and backfill, which may result in liquefaction.

The occurrence of liquefaction in both the saturated backfill and in the foundation was the main reason for the devastating effects to gravity quay walls in a number of past earthquakes . Damage to port facilities in *Kobe*, Japan during the 1995 *Hyogoken-Nanbu* earthquake, is another example of failure of gravity quay walls due to liquefaction. Furthermore, observations of 24 marine structures in the 1999 *Kocaeli* earthquake in Turkey revealed that the backfill of quay walls liquefied resulting in seaward displacements of the quay walls. The same observations were reported during the 1999 *Chi Chi* earthquake in Taiwan.

The seismic coefficient method consisting of the *Mononobe-Okabe's* formula is usually adopted in the structural design of gravity type quay walls to resist earthquake damage, but this design method does not take into account the liquefaction of the backfill soil or the foundations. Gravity quay walls failures have stimulated much progress in the development of a deformation-based design method of geotechnical structures. Significant experimental and theoretical research work (Sugano et al. 1996; Inagaki et al. 1996; Iai 1998; Iai et al. 1998; Iai and Sugano 2000; Ichii et al. 2000; Inoue et al. 2003; Nozu et al. 2004; Mostafavi Moghadam et al. 2009 and 2011).

Predicting the response of a structure retained a liquefiable soil during an earthquake is highly dependent on adequately accounting for the effects of pore water pressure development, stress-strain softening and strength reduction in the soil on the system behavior. Thus, it is required to perform dynamic analyses that account for the saturated soil-structure interaction effects using numerical modeling techniques.

[M. Alyami, M. Rouainia, S.M. Wilkinson]

Figure 1.1 : Quay walls displacement and incline to the sea at Kobe, Japan 1995 earthquake

Figure 1.2 : Substantial damages in the pavement, placed in the foot of quay walls during Kobe, Japan 1995 earthquake

Figure 1.3 : Large settlement of embankments behind quay walls at Kobe, Japan 1995 earthquake

Figure 1.4 : Overturn and great extent of quay wall's incline in Kobe 1995 earthquake

Figure 1.5 : Settlement behind caisson-type quay wall in the port of Taichung, who suffered large displacement in 1999 Chi Chi earthquake

Figure 1.4 : Damaged quay walls at Navy Seals' base of Gölcük in the 1999 Kocaeli earthquake in Turkey

Figure 1.5 : Soil deformation behind quay wall at the port of Taichung during the 1999 Chi Chi earthquake

Figure 1.6 : Damages at the waterfront because of quay wall's displacement in 1999 Chi Chi earthquake

1.2 Scope

In this diploma thesis, the effort is concentrated at the study of dynamic response of a typical caisson-type quay wall section at Piraeus port in Greece and the development of vulnerability curves based on numerical analysis.

Utilizing the Byrne's elastoplastic constitutive model, an effective stress dynamic analysis is performed using as seismic excitation fifteen recorded motions of the seismic environment throughout the world. These excitations are applied to three different types of the backfill soil regarding the relative density (Dr). Primarily, the results emphasize the role of relative density and time history of excitation on the horizontal displacement and the tilt of a typical caisson-type quay wall. Supplementary results demonstrate secondary deformations of a caisson-type quay wall, like the settlement of the backfill soil and the heave of the soil surface at the sea bottom, in front of the toe of the wall. The excess pore-water pressure, positive or negative, build-up during shaking is also examined in extent, shedding light on the liquefied or non-liquefied regions of the soil profile and the ensuing deformation of the adjacent quay-wall, in sight of interaction.

The numerical modeling is performed using the two-dimensional finite element program Plaxis2D in order to extract the results that are of our interest in this thesis, either it is the time histories of some variables or the ultimate values of others.

Chapter 2

Aspects of earthquake engineering

2.1 *Type of Dynamic Loading on Soils*

2.1.1 Intoduction

The type of dynamic loading in soil or the foundation of a structure depends on the nature of the source producing it. Dynamic loads vary in their magnitude, direction or position with time. More than one type of variation of forces may coexist. Periodic load is a special type of load that varies in magnitude with time and repeats itself at regular intervals, for example, operation of reciprocating or a rotary machine. Non periodic loads are those loads that do not show any periodicity, for example, wind loading on a building. Deterministic loads are those loads that can be specified as define functions of time, irrespective of whether the time variation is regular, for example, the harmonic load imposed by unbalanced rotating machinery. Nondeterministic loads are those loads that can be described as define functions of time because of their inherent uncertainty in their magnitude and form of variation with time, for example, earthquake loads (Humar 2001). Cyclic loads are those loads which exhibit a degree of regularity both in its magnitude and frequency. Static loads are those loads that build up gradually over time, or with negligible dynamic effects. They are also known as monotonic loads. Stress reversals, rate effects and dynamic effects are the important factors, which distinguishes cyclic loads from static loads (Reilly and Brown 1991).

The operation of a reciprocating or a rotary machine typically produces a dynamic load pattern, as as shown in Figure 2.1a. This dynamic load is more or less sinusoidal in nature and may be idealized, as shown in Figure 2.1b.

The impact of a hammer on a foundation produces a transient loading condition in soil, as shown in Figure 2.2a. The load typically increases with time up to a maximum value at time $t = t1$ and drops to zero after that. The case shown in Figure 2.2a is a single-pulse load. A typical loading pattern (vertical acceleration) due to a pile-driving operation is shown in Figure 2.2b.

Dynamic loading associated with an earthquake is random in nature. A load that varies in a highly irregular fashion with time is sometimes referred to as a random load. Figure 1.3 shows the accelerogram of the E1 Centro, California, and earthquake of May 18, 1940 (north-south component).

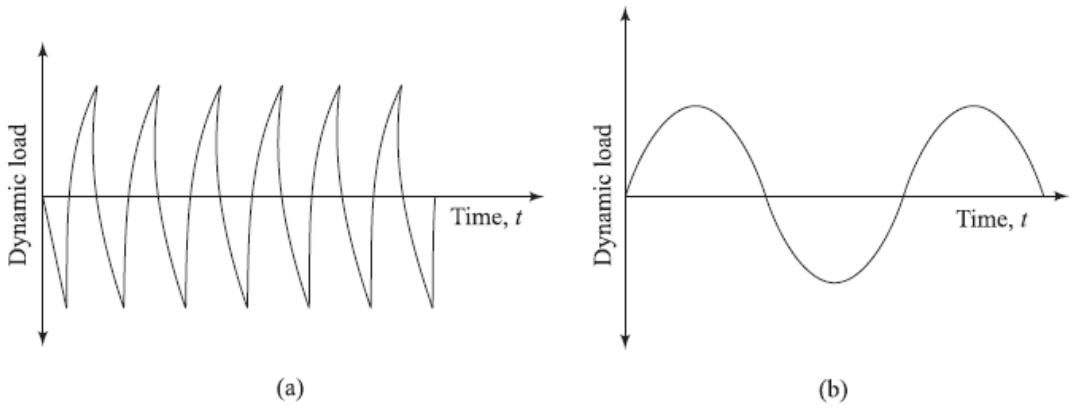

Figure 2.1 : (a) Typical load versus record for a low-speed rotary machine;
(b) Sinusoidal idealization for (a)

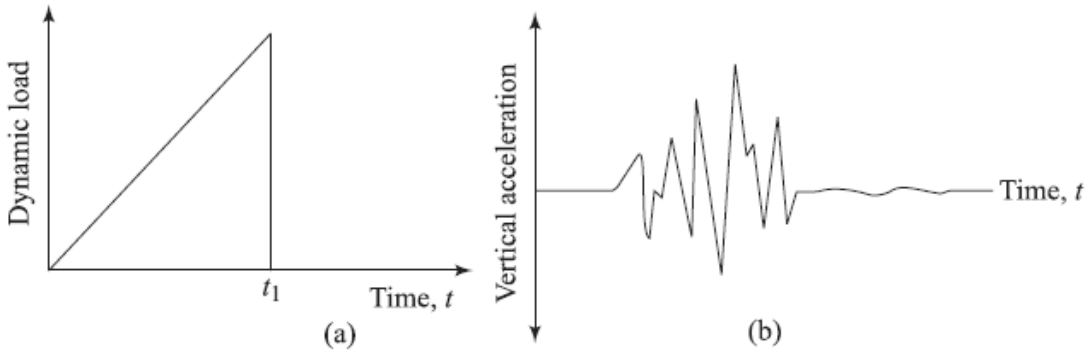

Figure 2.2 : Typical loading diagrams: (a) transient loading due to single impact of a hammer;
(b) Vertical component of ground acceleration due to pile driving

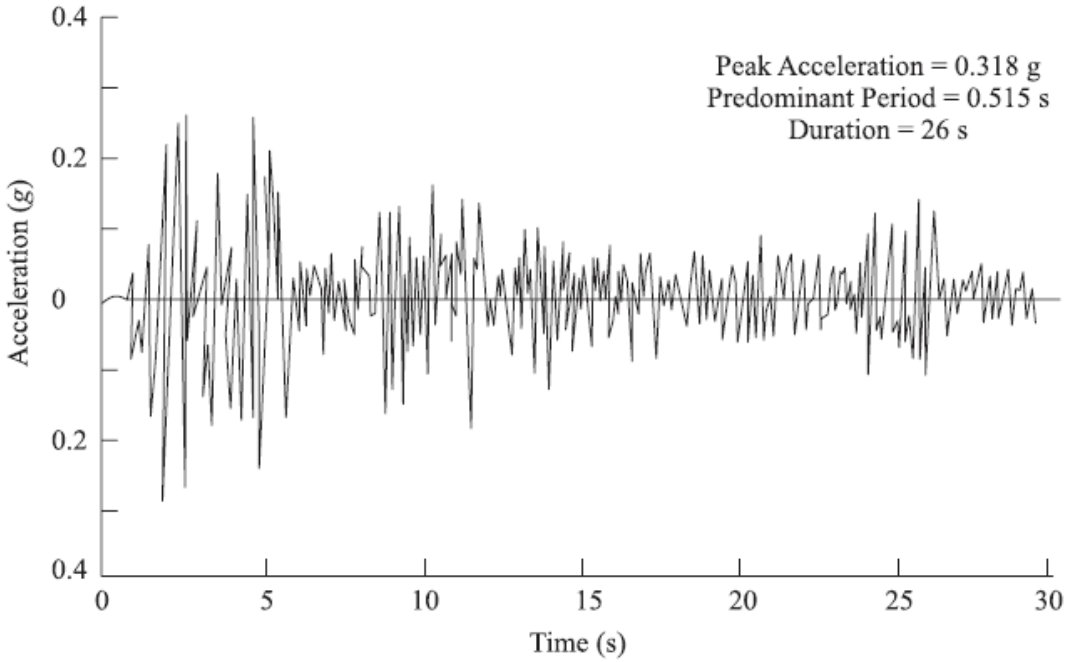

Figure 2.3 : Accelerogram of E1 Centro, California, earthquake of May 18, 1940 (N-S component)

For considerations of land-based structures, earthquakes are the important source of dynamic loading on soils. This is due to the damage-causing potential of strong motion earthquakes and the fact that they represent an unpredictable and uncontrolled phenomenon in nature. The ground motion due to an earthquake may lead to permanent settlement and tilting of footings and, thus, the structures supported by them. Soils may liquify, leading to buildings sinking and lighter structures such as septic tanks floating up (Prakash, 1981).

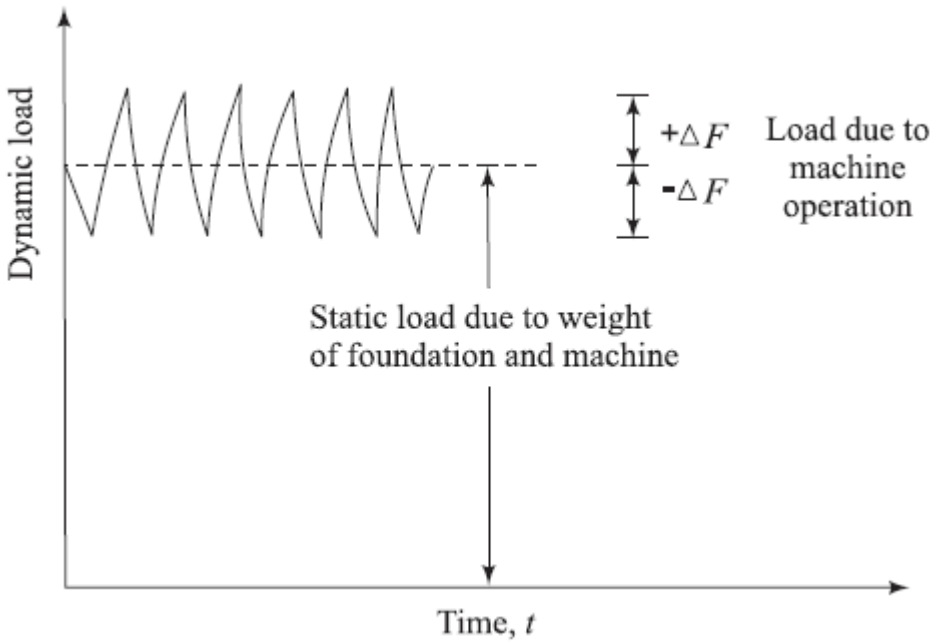

Figure 2.4 : Schematic diagram showing loading on the soil below the foundationduring machine operation

For offshore structures, the dynamic load due to storm waves generally represents the significant load. However, in some situations the most severe loading conditions may occur due to the combined action of storm waves and earthquakes loading. In some cases the offshore structure must be analyzed for the waves and earthquake load acting independently of each other (Puri and Das, 1989; Puri, 1990).

The loadings represented in Figures 2.1, 2.2 and 2.3 are rather simplified presentations of the actual loading conditions. For example, it is well known that earthquakes cause random motion in every direction. Also, pure dynamic loads do not occur in nature and are always a combination of static and dynamic loads. For example, in the case of a well-designed foundation supporting a machine, the dynamic load due to machine operation is a small fraction of the static weight of the foundation (Barkan, 1962). The loading conditions may be represented schematically by Figure 1.4. Thus in a real situation the loading conditions are complex. Most experimental studies have been conducted using simplified loading conditions.

2.1.2 Ground vibration

The vibration of the soil layers due to an earthquake is due to the upward propagation of shear waves from the underlying rock or rocklike layer. The response of a horizontal soil layer with linearly elastic properties, developed by Idriss and Seed (1968), is presented in this section.

Homogeneous Soil Layer

Figure 2.5 shows a horizontal soil layer of thickness *H* underlain by a rock or rocklike material. Let the underlying rock layer be subjected to a seismic motion *ug* that is a function of time *t*. Considering a soil column of unit cross sectional area, the equation of motion can be written as

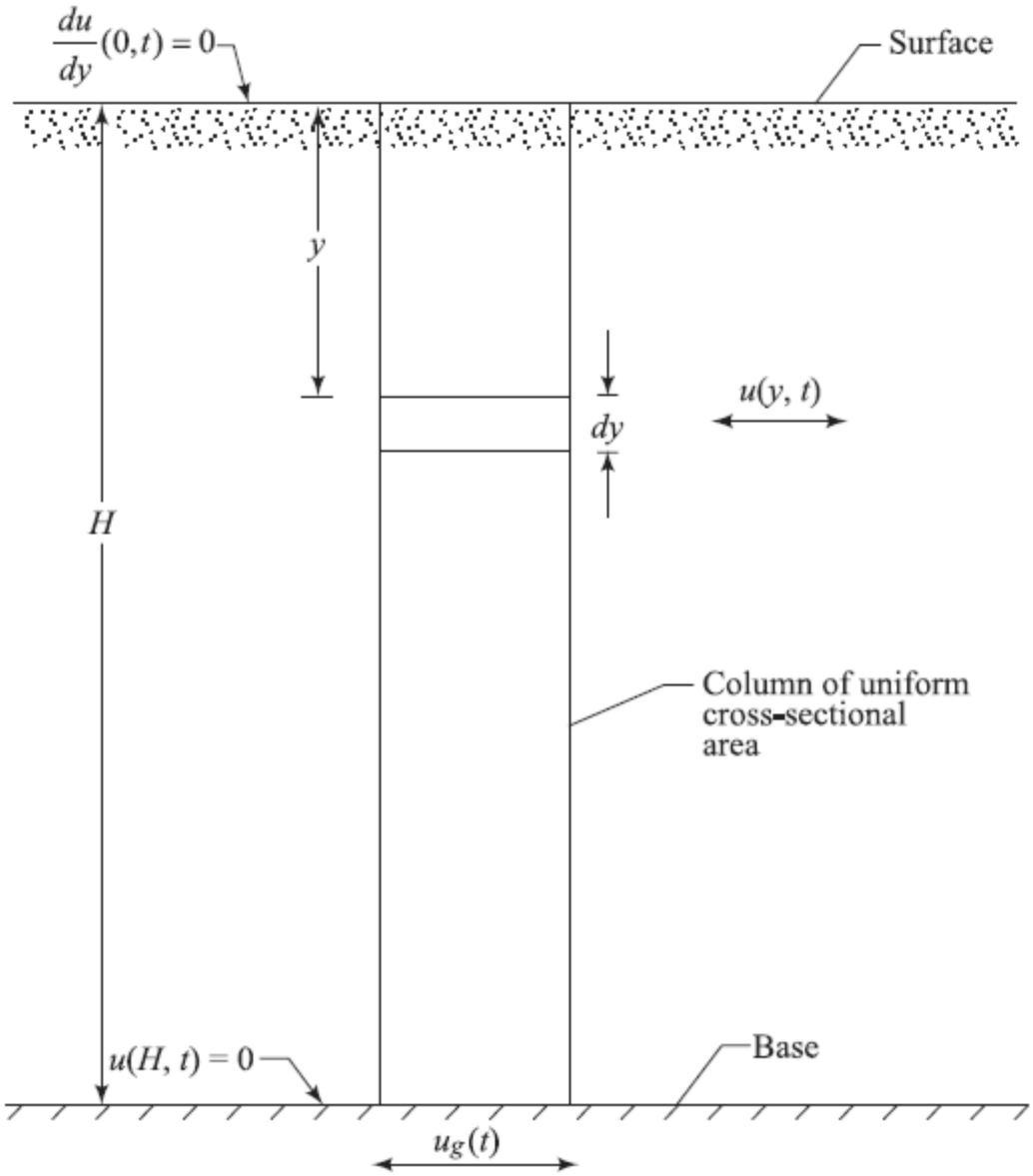

Figure 2.5 : Cross section and boundary conditions of a semi-infinite soil layer subjected to a horizontal seismic motion at its base

$$\rho(y)\frac{\partial^2 u}{\partial t^2}+c(y)\frac{\partial u}{\partial t}-\frac{\partial}{\partial y}\left[G(y)\frac{\partial u}{\partial y}\right]=-\rho(y)\frac{\partial^2 u_g}{\partial t^2} \qquad (2.1)$$

Where u = relative displacement at depth y and time t
$G(y)$ = shear modulus at depth y
$c(y)$ = viscous damping coefficient at depth y
$\rho(y)$ = density of soil at depth y

The shear modulus can be given by the equation

$$G(y) = Ay^B \qquad (2.2)$$

Where A and B are constant depending on the nature of the soil.

Substituting Eq. (2.2) into Eq. (2.1), we obtain

$$\rho\frac{\partial^2 u}{\partial t^2}+c\frac{\partial u}{\partial t}-\frac{\partial}{\partial y}\left[\mathrm{A}y^{\mathrm{B}}\frac{\partial u}{\partial y}\right]=-\rho\frac{\partial^2 u_g}{\partial t^2} \qquad (2.3)$$

For the case of $B \neq 0$ (but < 0.5), using the method of separation of variables, the solution to Eq. (2.3) can be given in the form

$$u(y,t)=\sum_{n=1}^{\infty} y = Y_n(y)X_n(t)$$

(2.4)
Where

$$Y_n(y)=\left(\frac{1}{2}\beta_n\right)^b \Gamma(1-b)\left(\frac{y}{H}\right)^{\frac{b}{\theta}} J_{-b}\left[\beta_n\left(\frac{y}{H}\right)^{\frac{1}{\theta}}\right] \qquad (2.5)$$

and

$$\ddot{X}_n+2D_n\omega_n\dot{X}_n+\omega_n^2X_n=-R_n\ddot{u}_g$$

(2.6)

J_{-b} is the Bessel function of first kind of order – b, βn represents the roots of $J_{-b}(\beta n) = 0$, n = 1, 2, 3…, and the circular natural frequency of nth mode of vibration is

$$\omega_n = \beta_n \frac{\sqrt{\mathrm{A}/\rho}}{\theta H^{1/\theta}} \tag{2.7}$$

The damping ratio in the *n*th mode is

$$D_n = \frac{\frac{1}{2}c}{\rho\omega_n} \tag{2.8}$$

and Γ is the gamma function,

$$R_n = \left[\left(\frac{1}{2}\beta_n\right)^{1+b} \Gamma(1-b) J_{1-b}(\beta_n)\right]^{-1} \tag{2.9}$$

The terms *b* and θ are related as follows:

$$B\theta - \theta + 2b = 0 \tag{2.10}$$

and

$$B\theta - 2\theta + 2 = 0 \tag{2.11}$$

For detailed derivations, see Idriss and Seed (1967).

Special Cases

Cohesionless Soils: In the case of cohesionless soils, the shear modulus [Eq. (2.2)] can be approximated as

$$G(y) = Ay_{1/2} \text{ or } G(y) = Ay_{1/3}$$

Assuming the latter to be representative (i.e., $B = 1\ 3$), Eqs. (2.10) and (2.11) can be solved, yielding

$b = 0.4$ and $\theta = 1.2$

Hence, Eqs. (2.5)–(2.7) take the following form:

$$Y_n(y) = \left(\tfrac{1}{2}\beta_n\right)^{0.4} \Gamma(0.6)\left(\frac{y}{H}\right)^{1/3} J_{-0.4}\left[\beta_n\left(\frac{y}{H}\right)^{5/6}\right] \tag{2.12}$$

$$\ddot{X}_n + 2D_n\omega_n\dot{X}_n + \omega_n^2 X_n = -\ddot{u}_g\left[\left(\frac{\beta_n}{2}\right)^{1.4}\Gamma(0.6)J_{0.6}(\beta_n)\right]^{-1} \tag{2.13}$$

and

$$\omega_n = \frac{\beta_n\sqrt{A/\rho}}{1.2H^{5/6}} \tag{2.14}$$

(*Note:* $\beta_1 = 1.7510$, $\beta_2 = 4.8785$, $\beta_3 = 8.0166$, $\beta_4 = 11.1570$….)

Cohesive Soils: In cohesive soils, the shear modulus may be considered to be approximately constant with depth; so, in Eq. (2.2), $B = 0$ and

$$G(y) = A \tag{2.15}$$

With this assumption, Eqs. (2.5)–(2.7) are simplified as

$$Y_n(y) = \cos\left[\frac{1}{2}(2n-1)\left(\frac{y}{H}\right)\right] \tag{2.16}$$

$$\ddot{X}_n + 2D_n\omega_n\dot{X}_n + \omega_n^2 X_n = (-1)^n\left[\frac{4}{(2n-1)\pi}\right]\ddot{u}_g \tag{2.17}$$

and

$$\omega_n = \left[\frac{(2n-1)\pi}{2H}\right]\sqrt{\frac{G}{\rho}} \tag{2.18}$$

2.1.3 Response Spectrum Analysis

The response spectrum method (RSM) was introduced in 1932 in the doctoral dissertation of Maurice Anthony Biot at Caltech. It is an approach to finding earthquake response of structures using waves or vibrational mode shapes. The mathematical principles of oscillations in *n*-degree-of-freedom systems were taken largely from the theories of acoustics developed by Rayleigh. Biot stated "…[a] building…has a certain number of so called *normal modes* of vibration, and to each of them corresponds a certain frequency. Biot utilized the Fourier amplitude spectrum to find the maximum amplitude of motion of a system: the sum of amplitudes for each separate mode of oscillation
(Trifunac and Todorovska, 2008).

The concept of the "response spectrum" was applied in design requirements in the mid 20th Century, for example in building codes in the state of California (Hudson, 1956; Trifunac and Todorovska, 2008). Itcame into widespread use as the primary theoretical tool in earthquake engineering in the 1970s whenstrong-motion accelerograph data became widely available (Trifunac and Todorovska, 2008).

Using a mathematical model of a building, for example with given masses, stiffness values, and dimensions for each storey, earthquake acceleration records can be applied to evaluate how the given structure behaves (Clough, 1962). System response is represented as the linear superposition of singledegree-of-freedom systems for various mode shapes and corresponding natural frequencies (Trifunac andTodorovska, 2008).

The system used for analysis consists of a mass, *m*, spring with constant *k*, and dashpot with viscous damping constant, *c* (with units of force x time per length) (Figure 2.6).

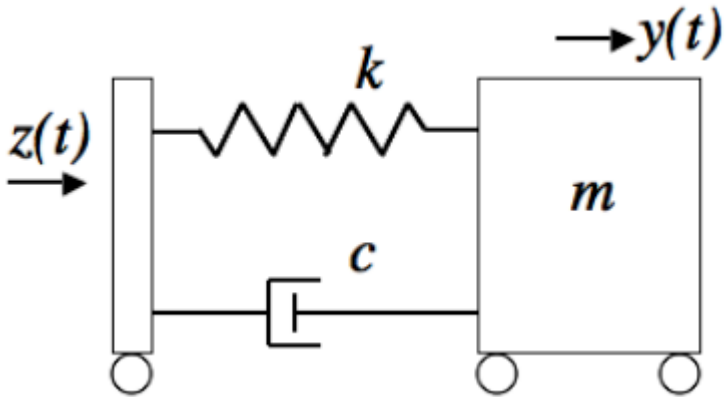

Figure 2.6 : Simple damped mass -spring system with forcing function *z(t)*

The system responds to a ground displacement $z(t)$ with absolute displacement $y(t)$. Given the ground motion, or input, the response of the system can be determined using Newton's second law (de Silva,2005) :

$$m(\ddot{y} + \ddot{z}) = -ky - cy \tag{2.19}$$

or using natural, undamped, radial frequency, ω , and damping ratio, $\xi = \frac{c}{2\sqrt{km}}$:

$$\ddot{y} + 2\xi\omega\dot{y} + \omega 2y = -\ddot{z} \tag{2.20}$$

If $\ddot{z} = 0$, this is the unforced, homogeneous equation of motion (de Silva, 2005). The free response of a damped simple oscillator is

$$y = Ce^{\lambda t} \tag{2.21}$$

Considering the homogeneous situation and substituting (2.21) into (2.20) provides

$$(\lambda 2 + 2\xi\omega\lambda + \omega 2)Ce^{\lambda t} = 0 \tag{2.22}$$

which depends only on the characteristics of the mass-spring system, not the excitation. The roots, λ_1 and λ_2 are the eigenvalues, or poles, of the system and define the frequencies of vibration. Modal shapes are defined by the eigenvectors (Trifunac and Todorovska, 2008; Clough, 1962). A system's linear response (i.e. without brittle deformation) to excitation is a linear combination of modal vibrations and failure is more likely if resonance occurs. Modal vibrations are due to naturally preferred configurations (and associated frequencies). Nontrivial solutions for the *n*-dimensional form of (4) exist when the determinant is equal to zero (Trifunac and Todorovska, 2008). For the underdamped system ($\xi < 1$) the eigenvalues in (2.22) are

$$\lambda = -\xi\omega \pm j\sqrt{1-\xi\omega} \tag{2.23}$$

Substituting $\omega_d = \sqrt{1-\xi^2}\omega$, known as the damped natural frequency, and taking the general form of (2.21) gives a response

$$y = e^{-\xi\omega t}\left[C_1 e^{j\omega_d t} + C_2 e^{-j\omega_d t}\right] \tag{2.24}$$

Knowing that complex exponentials can be expressed in terms of sines and cosines and assigning constants $A_1 = C_1 + C_2$ and $A_2 = j\,(C_1 - C_2)$ (de Silva 2005), (2.24) can be rewritten as

$$y = e^{-\xi\omega t}\left[\mathrm{A}_1 \cos\omega_d t + \mathrm{A}_2 \sin\omega_d t\right] \tag{2.25}$$

In terms of initial position and velocity, x_0 and v_0 ,

$$A_1 = x_0 \text{ and } A_2 = \frac{v_0 + \xi\omega x_0}{\omega_d} \tag{2.26}$$

For $A = \sqrt{\mathrm{A}_1^2 + \mathrm{A}_2^2}$, (2.25) can be written in the form

$$y = Ae^{-\xi\omega t}\sin(\omega_d t + \phi) \tag{2.27}$$

with $\sin\varphi = \frac{A_1}{\sqrt{A_1^2 + A_2^2}}$. When there is forcing input, as with an earthquake, the equation becomes non homogeneous and the solution is a sum of the homogeneous solution and the particular integral for the equation of motion in (2.20). The behavior can be studied in either the time domain or the frequency domain (de Silva 2005). For a physical system with an input $z(t)$ at time $t = \tau$,

$$y(t-\tau) = z(t-\tau) = 0 \text{ for } t < \tau \tag{2.28}$$

where y is the total response of the system. $h(t-\tau)$ will be taken as the delayed response. An arbitrary input z can be divided into a series of pulses with magnitude $z(\tau)\Delta\tau$ and width $\Delta\tau$. In a linear system with constant parameters, the total response is

$$y = \sum_{\tau=0}^{t} h(t-\tau)z(\tau)\Delta\tau \tag{2.29}$$

and taking the limit as $\Delta\tau \to 0$ gives the convolution integral,

$$y(t) = \int_0^t h(t-\tau)z(\tau)d\tau \tag{2.30}$$

This is the final solution for (2). Substituting (9) for h and making the appropriate substitutions for terms of ω and ξ , the absolute acceleration of the system takes the form of the Duhamel integral equation (Clough, 1962):

$$\ddot{y} = \omega \int_0^t \ddot{z}(t) e^{-\omega\xi(t-\tau)} \sin\omega(t-\tau) d\tau \tag{2.31}$$

This is using the assumption of small damping, ξ < 0.2 so that $\sqrt{1-\xi^2} \approx 1$ (Hudson, 1956). It is straightforward to find comparable expressions for velocity and displacement.

Of interest in response spectrum analysis is the maximum displacement, velocity, or acceleration and a plot of any of those maximum values versus natural, undamped frequency is considered the *response spectrum* (de Silva, 2005; Hudson, 1956) (**Figure 2.7 (a)**). The maximum value of the integral in (2.31) will be denoted S_v , which is termed the spectral velocity (Clough, 1962). The maximum values for relative displacement, relative velocity, and absolute acceleration of the system are thus, respectively,

$$\begin{aligned} (y - z)_{\max} &= \frac{1}{\omega} S_v \\ (\dot{y} - \dot{z})_{\max} &= S_v \\ \ddot{y}_{max} &= \omega S_v \end{aligned} \tag{2.32}$$

The importance of S_v is apparent, as it is proportional to the maximum energy per unit mass,

$$\frac{E}{m} = \frac{1}{2} S_v^2 \tag{2.33}$$

and because relative displacement, given in (2.32), is proportional to the strains within a system. The easiest measurement to make in a moving structure is its absolute acceleration so the calculated maximum acceleration of the system, also given in (2.32), can be compared with empirical results (Hudson, 1956). For design purposes, an envelope of spectra for varying earthquakes is determined (de Silva, 2005).

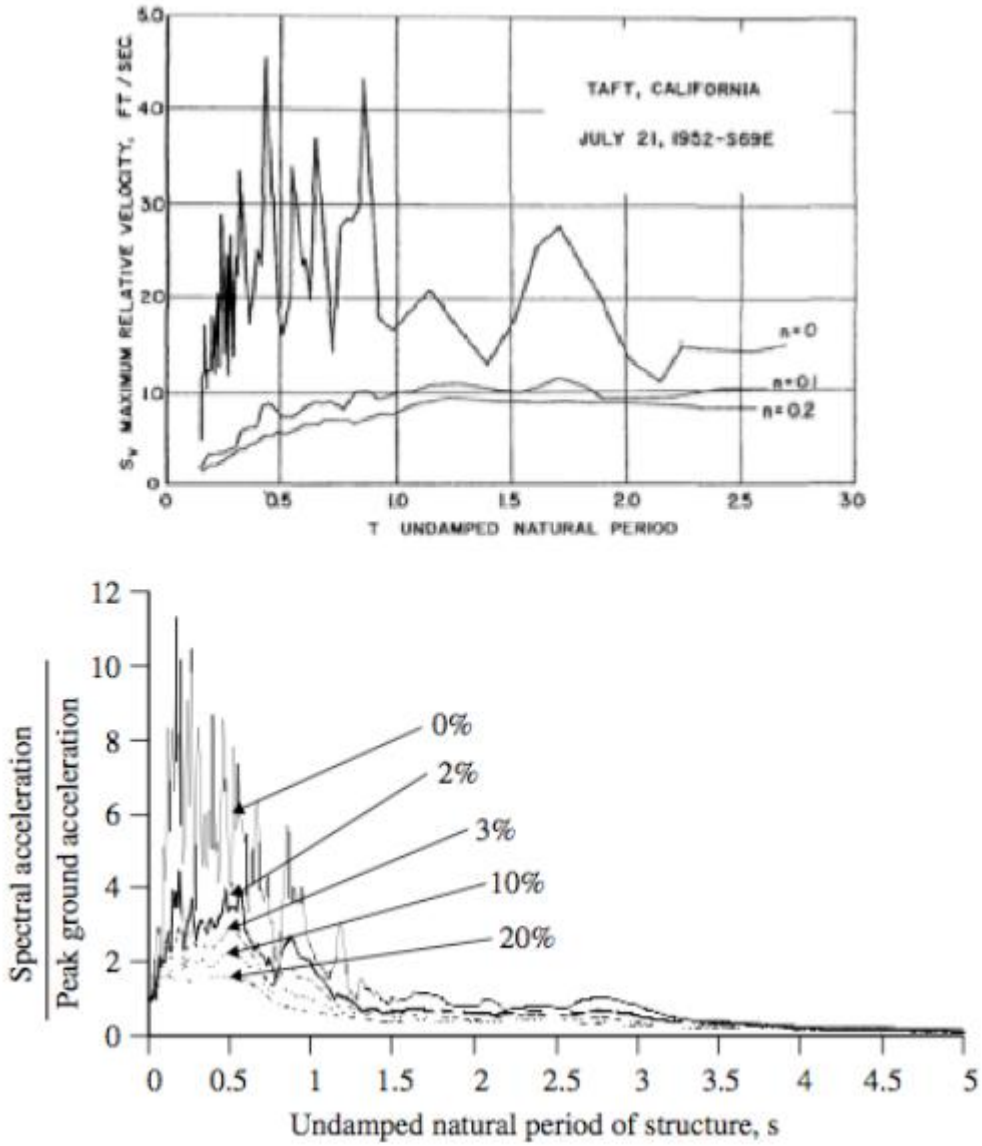

Figure 2.7 : (a) example of a relative velocity response spectrum for various damping ratios (*from Hudson, 1956),* (b) Acceleration response spectrum for El Centro 1940 earthquake and a range of damping ratios between 0-20% (*Modified from de Silva, 2005**)***

Given a ground acceleration or ground motion record, the integral in (2.31) must be evaluated for various values of ω and ξ (Hudson, 1956). However, for design purposes, calculation of the Duhmel integral is not always necessary. Often, the spectral response for a range of periods is available for a local historical earthquake (Clough 1962) or, based on the seismic history of an area, an acceleration spectrum envelope is developed for use in structural design. *Figure 2.7(b***)** shows the acceleration response spectra calculated for the El Centro 1940 earthquake for various damping values.

2.2 Liquefaction

2.2.1 Introduction

During earthquakes, major destruction of various types of structures occurs due to the creation of fissures, abnormal and/or unequal movement, and loss of strength or stiffness of the ground. The loss of strength or stiffness of the ground results in the settlement of buildings, failure of earth dams, landslides and other hazards. The process by which loss of strength occurs in soil is called *soil liquefaction*. The phenomenon of soil liquefaction is primarily associated with medium – to fine-grained *saturated cohesionless soils*. Examples of soil liquefaction-related damage are the June 16, 1964, earthquake at Niigata, Japan, the 1964 Alaskan earthquake, and also the 2001 *Republic Day* earthquake at Bhuj, India. Most of the destruction at port and harbor facilities during earthquakes is attributable to liquefaction. Classical examples are Kobe Port, Japan (1995 earthquake) and at Kandla Port, India (2001 earthquake).

One of the first attempts to explain the liquefaction phenomenon in sandy soils was made by Casagrande (1936) and is based on the concept of *critical void ratio*. Dense sand, when subjected to shear, tends to dilate; loose sand, under similar conditions, tends to decrease in volume. The void ratio at which sand does not change in volume when subjected to shear is referred to as the *critical void ratio*. Casagrande explained that deposits of sand that have a void ratio larger than the critical void ratio tend to decrease in volume when subjected to vibration by a *seismic effect*. If drainage is unable to occur, the pore water pressure increases. Based on the effective stress principles, at any depth of a soil deposit

$$\sigma' = \sigma - u \tag{2.34}$$

where σ' = effective stress
σ = total stress
u = pore water pressure

If the magnitude of s remains practically constant, and the pore water pressure gradually increases, a time may come when σ will be equal to u. At that time, σ' will be equal to zero. Under this condition, the sand does not possess any shear strength, and it transforms into a liquefied state. However, one must keep in mind the following facts, which show that the critical void ratio concept may not be sufficient for a quantitative evaluation of soil liquefaction potential of sand deposits:

1. Critical void ratio is not a constant value, but changes with confining pressure.
2. Volume changes due to dynamic loading conditions are different than the one directional static load conditions realized in the laboratory by direct shear and triaxial shear tests.

2.2.2 Fundamental Concept of Liquefaction

Figure 2.8 shows the gradual densification of sand by repeated back-and-forth straining in a simple shear test. For this case drainage from the soil occurs freely. Each cycle of straining reduces the void ratio of the soil by a certain amount, although at a decreasing rate. It is important to note that there exists a threshold shear strain, below which no soil densification can take place, irrespective of the number of cycles. Decrease in volume of the sand, as shown in Figure 2.8, can take place only if drainage occurs freely. However, under earthquake conditions, due to rapid cyclic straining this will not be the condition. Thus, during straining gravity loadings is transferred from soil solids to the pore water. The result will be an increase of pore water pressure with a reduction in the capacity of the soil to resist loading.

This is schematically shown in Figure 2.9. In this figure, let A be the point on the compression curve that represents the void ratio (e_0) and effective state of stress (σ') at a certain depth in a saturated sand deposit. Due to a certain number of earthquake related cyclic straining, let $AB = \Delta e$ be the equivalent change of void ratio of the soil at that depth if full drainage is allowed. However, if drainage is prevented, the void ratio will remain as e_0 and the effective stress will be reduced to the level of σ'_C , with an increase of pore water pressure of magnitude Δu. So the state of the soil can be represented by point C. If the number of cyclic straining is large enough, the magnitude of Δu may become equal to σ'_A , and the soil will liquefy.

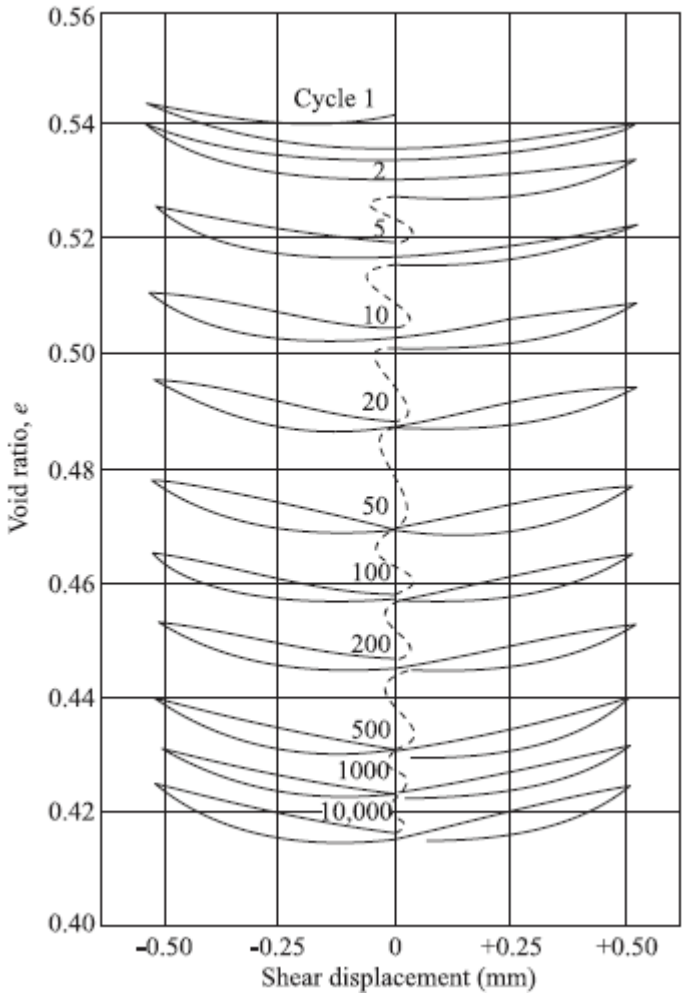

Figure 2.8 : Void ratio versus cyclic shear displacement for densification of a sand with successive cycles of shear (after Youd, 1972)

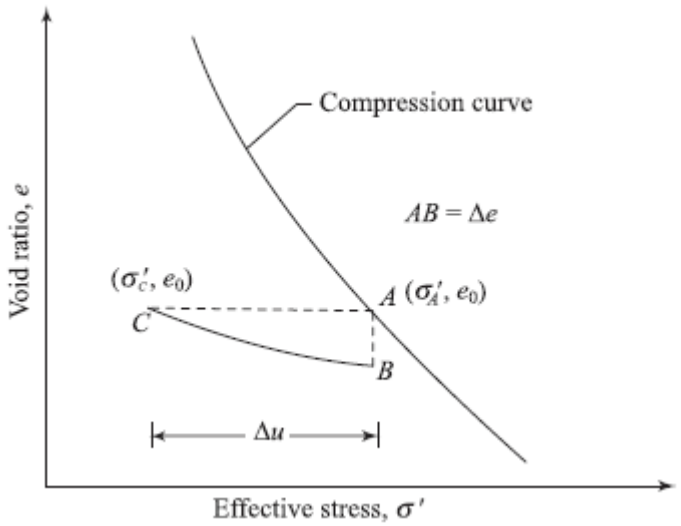

Figure 2.9 : Mechanism of pore water pressure generation due to cyclic loading in undrained conditions

2.2.3 Laboratory Studies to Simulate Field Conditions for Soil Liquefaction

If one considers a soil element in the field, as shown in Figure 2.10a, when earthquake effects are not present, the vertical effective stress on the element is equal to σ' , which is equal to σ_v , and the horizontal effective stress on the element equals $K_0\,\sigma_v$, where K_0 is the at-rest earth pressure coefficient. Due to ground-shaking during an earthquake, a cyclic shear stress t_h will be imposed on the soil element. This is shown in Figure 2.10b. Hence, any laboratory test to study the liquefaction problem must be designed in a manner so as to simulate the condition of a constant normal stress and a cyclic shear stress on a plane of the soil specimen. Various types of laboratory test procedure have been adopted in the past, such as the dynamic triaxial test (Seed and Lee, 1966; Lee and Seed, 1967), cyclic simple shear test (Peacock and Seed, 1968; Finn, Bransby, and Pickering, 1970; Seed and Peacock, 1971), cyclic torsional shear test (Yoshimi and Oh-oka, 1973; Ishibashi and Sherif, 1974), and shaking table test (Prakash and Mathur, 1965). However, the most commonly used laboratory test procedures are the dynamic triaxial tests and the simple shear tests.

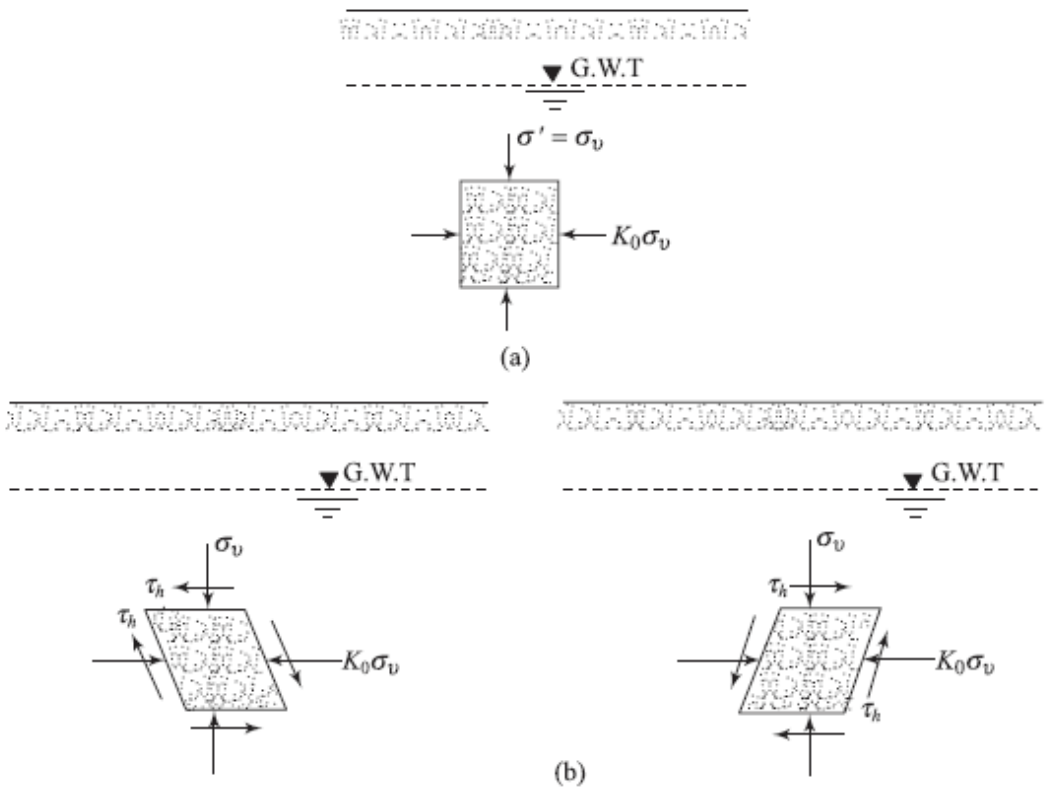

Figure 2.10: Application of cyclic shear stress on a soil element due to an earthquake

2.2.4 Cyclic Simple Shear Test

General Concepts

Cycle simple shear tests can be used to study liquefaction of saturated sands by using the simple shear apparatus. In this type of test, the soil specimen is consolidated by a vertical stress σ_v . At this time, lateral stress is equal to $K_0\ \sigma_v$ (K_0 = coefficient of earth pressure at rest). The initial stress conditions of a specimen in a simple shear device are shown in Figure 2.11a; the corresponding Mohr's circle is shown in Figure 2.11b. After that, a cyclic horizontal shear stress of peak magnitude τ_h is applied (undrained condition) to the specimen as shown in Figure 2.11c. The pore water pressure and the strain are observed with the number of cycles of horizontal shear stress application.

Using the stress conditions on the soil specimen at a certain time during the cyclic shear test, a Mohr's circle is plotted in Figure 2.11d. Note that the maximum shear stress on the specimen in simple shear is not τ_h, but

$$\tau_{max} = \sqrt{\tau_h^2 + \left[\frac{1}{2}\sigma_v\left(1 - K_0\right)\right]^2} \tag{2.35}$$

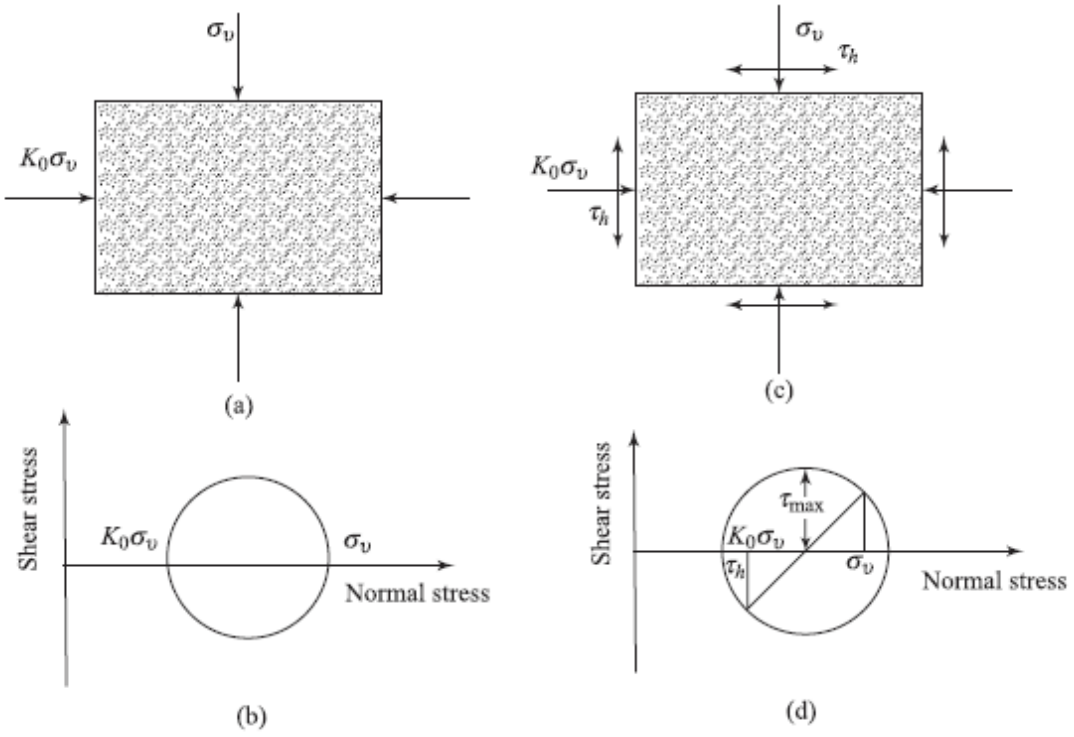

Figure 2.11: Maximum shear stress for cyclic simple shear test

Typical Test Results

Typical results of some soil liquefaction tests on Monterey sand using simple shear apparatus are shown in Figure 2.12. Note that these are for the initial liquefaction condition. From the figure the following facts may be observed:

1. For a given value of u s and relative density R_D, a decrease of τ_h requires an increase of the number of cycles to cause liquefaction.
2. For a given value of R_D and number of cycles of stress application, a decrease of u s requires a decrease of the peak value of τ_h for causing liquefaction.
3. For a given value of σ_v and number of cycles of stress application, τ_h for causing liquefaction increases with the increase of the relative density.

Another important factor – the variation of the peak value of τ_h for causing initial liquefaction with the initial relative density of compaction (for a given value of σ_v and number of stress cycle application) – is shown in Figure 2.13.
For a relative density up to about 80%, the peak value of τ_h for initial liquefaction increases linearly with R_D. At higher relative densities (which may not be practical to achieve in the field, particularly if fines are present), the relationship is nonlinear.

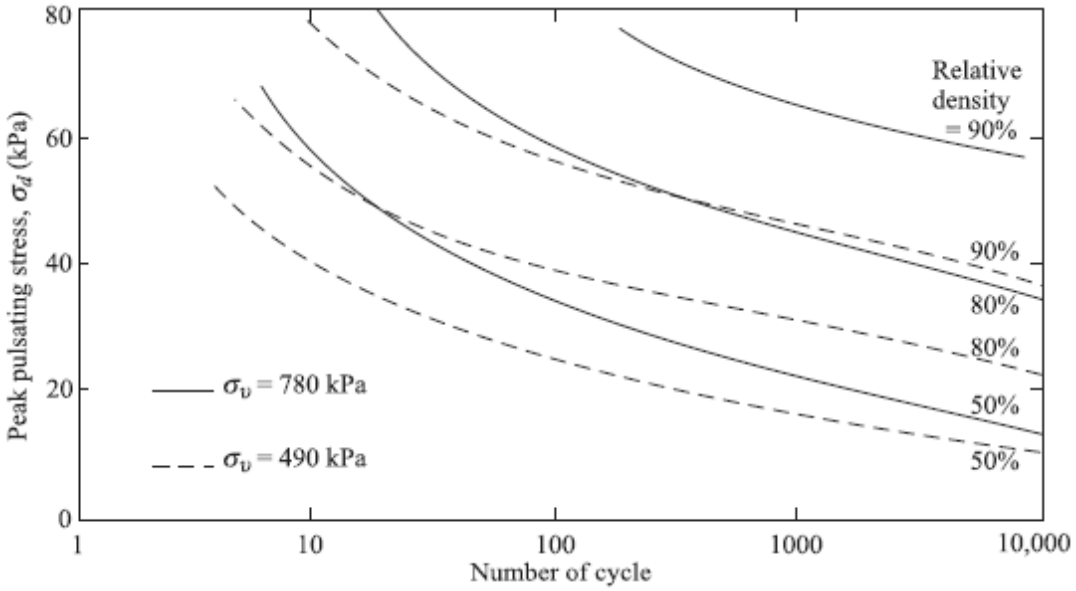

Figure 2.12: Initial liquefaction in cyclic simple shear test on Monterey sand (redrawn after Peacock and Seed, 1968

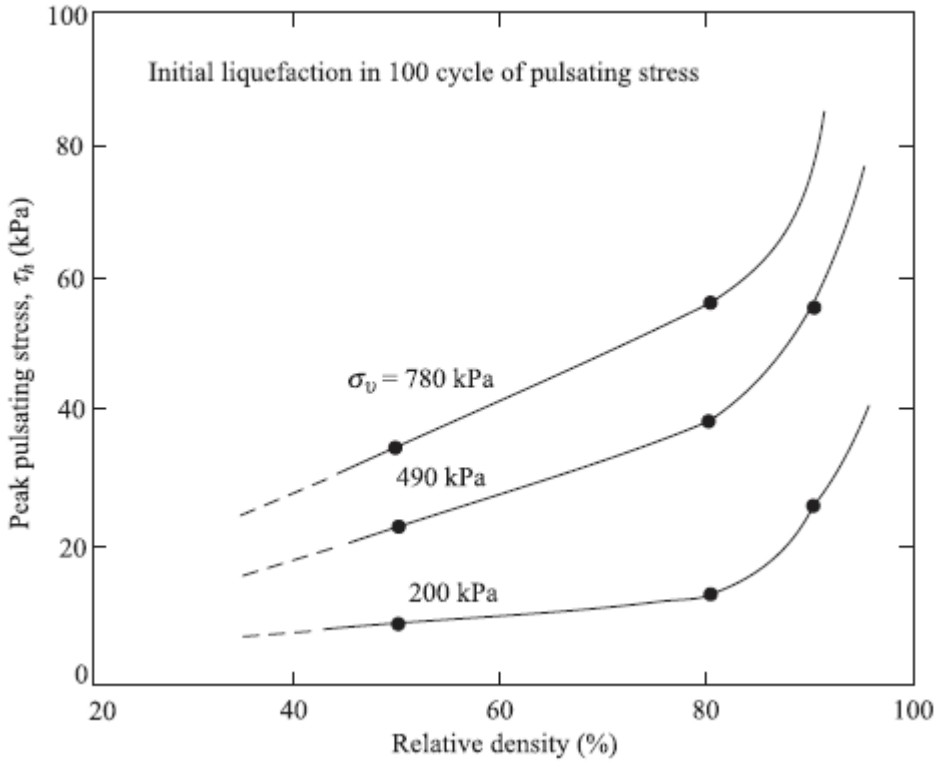

Figure 2.13: Effect of relative density on cyclic shear stress causing initial liquefaction of Monterey sand (redrawn after Peacock and Seed, 1968)

Influence of Test Condition

In simple shear test equipment, there is always some nonuniformity of stress conditions. This causes specimens to develop liquefaction under lower applied horizontal cyclic stresses as compared to that in the field. This happens even though care is taken to improve the preparation of the specimens and rough platens are used at the top and bottom of the specimens to be tested. For that reason, for a given value of σ_v, R_D, and number of cyclic shear stress application, the peak value of τ_h in the field is about 15% - 50% higher than that obtained from the cyclic simple shear test. This fact has been demonstrated by Seed and Peacock (1971) for a uniform medium sand ($R_D \approx 50\%$) in which the field values are about 20% higher than the laboratory values.

Influence of Overconsolidation Ratio on the Peak Value of τ_h Causing Liquefaction

For the cyclic simple shear test, the value of τ_h is highly dependent on the value of the initial lateral earth pressure coefficient at rest (K_0). The value of K_0, is in turn, dependent on the over consolidation ratio (OCR). The variation of τ_h / σ_v

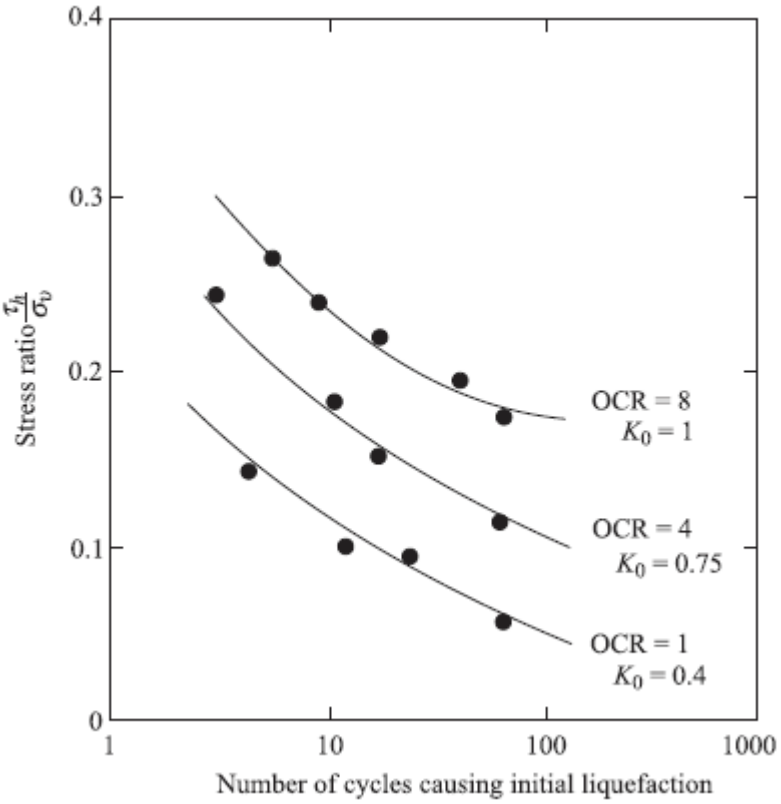

Figure 2.14: Influence of overconsolidation ratio on stresses causing liquefaction in simple shear tests (redrawn after Seed and Peacock, 1971)

for initial liquefaction with the overconsolidation ratio as determined by the cyclic simple shear test is shown in Figure 2.14. For a given relative density and number of cycles causing initial liquefaction, the value of τ_h / σ_v decreases with the decrease of K_0. It needs to be mentioned at this point that all the cyclic triaxial studies for liquefaction are conducted for the initial value of K_0 = 1.

Rate of Excess Pore Water Pressure Increase

Seed and Booker (1977) and DeAlba, Chan, and Seed (1975) measured the rate of excess pore water pressure increase in saturated sands during liquefaction using cyclic simple shear tests. The range of the variation of pore water pressure generation u_g during cyclic loading is shown in Figure 2.15. The average value of the variation of *ug* can be expressed in a nondimensional form as (Seed, Martin, and Lysmer, 1975)

$$\frac{u_g}{\sigma_v} = \left(\frac{2}{\pi}\right) \arcsin\left(\frac{N}{N_i}\right)^{1/2\alpha} \tag{2.36}$$

where u_g = excess pore water pressure generated

σ_v = initial consolidation pressure

N = number of cycles of shear stress application

Ni = number of cycles of shear stress needed for initial *liquefaction*

α = constant (≈ 0.7)

Hence, the rate of change of u_g with N can be given as

$$\frac{\partial u_g}{\partial N} = \left(\frac{2\sigma_v}{\alpha \pi N_i}\right)\left[\frac{1}{\sin^{2\alpha-1}\left(\frac{\pi}{2}r_u\right)\cos\left(\frac{\pi}{2}r_u\right)}\right] \tag{2.37}$$

where

$$r_u = \frac{u_g}{\sigma_v} \tag{2.38}$$

The preceding relationship is very useful in the study of the stabilization of potentially liquefiable sand deposits.

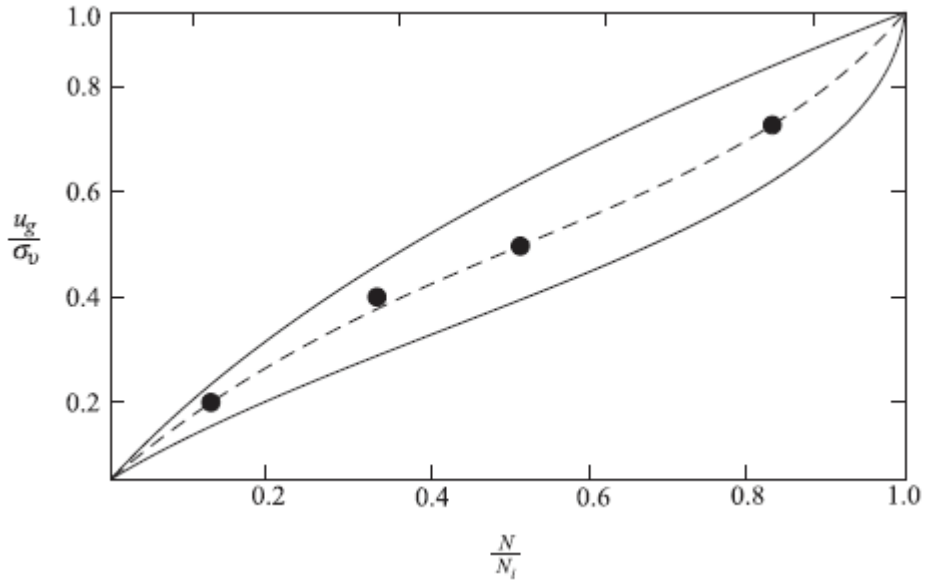

Figure 2.15: Rate of pore water pressure build up cyclic simple shear test [after Seed and Booker,1977]

2.2.5 Zone of Initial Liquefaction in the Field

There are five general steps for determining the zone in the field where soil liquefaction due to an earthquake can be initiated:

1. Establish a design earthquake.
2. Determine the time history of shear stresses induced by the earthquake at various depths of sand layer.
3. Convert the shear stress–time histories into N number of equivalent stress cycles. These can be plotted against depth, as shown in Figure 2.16.
4. Using the laboratory test results, determine the magnitude of the cyclic stresses required to cause initial liquefaction in the field in N cycles (determined from Step 3) at various depths. Note that the cyclic shear stress levels change with depth due to change of σ_v. These can be plotted with depth as shown in Figure 2.16.
5. The zone in which the cyclic shear stress levels required to cause initial liquefaction (Step 4) are equal to or less than the equivalent cyclic shear stresses induced by an earthquake is the zone of possible liquefaction. This is shown in Figure 2.16.

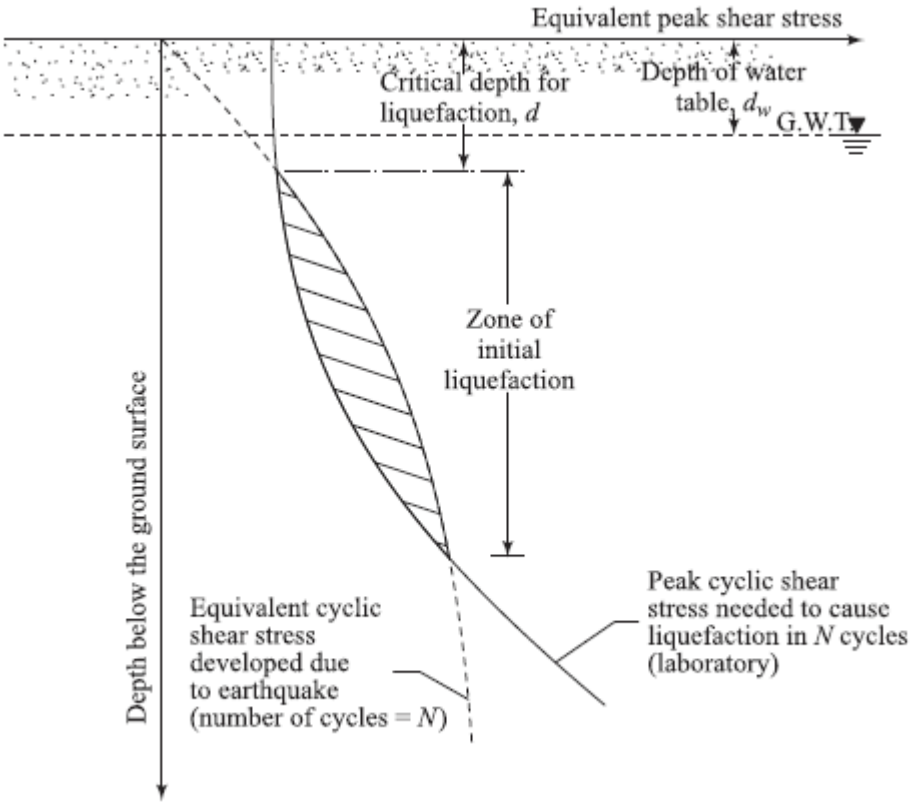

Figure 2.16: Zone of initial liquefaction in the field

2.2.6 Liquefaction Analysis from Standard Penetration Resistance

Another way of evaluating the soil liquefaction potential is to prepare correlation charts with the standard penetration resistance. After the occurrence of the Niigata earthquake of 1964, Kishida (1966), Kuizumi (1966), and Ohasaki (1966) studied the area in Niigata where liquefaction had and had not occurred. They developed criteria, based primarily on standard penetration resistance of sand deposits, to differentiate between liquefiable and nonliquefiable conditions. Subsequently, a more detailed collection of field data for liquefaction potential was made by Seed and Peacock (1971). These results and some others were presented by Seed, Mori, and Chan (1971) in a graphical form, which is a plot of τ_h / σ_v versus N'. This is shown in Figure 2.17. In this figure note that N' is the corrected standard penetration resistance for an effective overburden pressure of 100 kPa. Figure 2.18 shows the lower bounds of the correlation curve causing liquefaction in the field. However, correlation charts such as this cannot be used with confidence in the field, primarily because they do not take into consideration the magnitude of the earthquake and the duration of shaking.

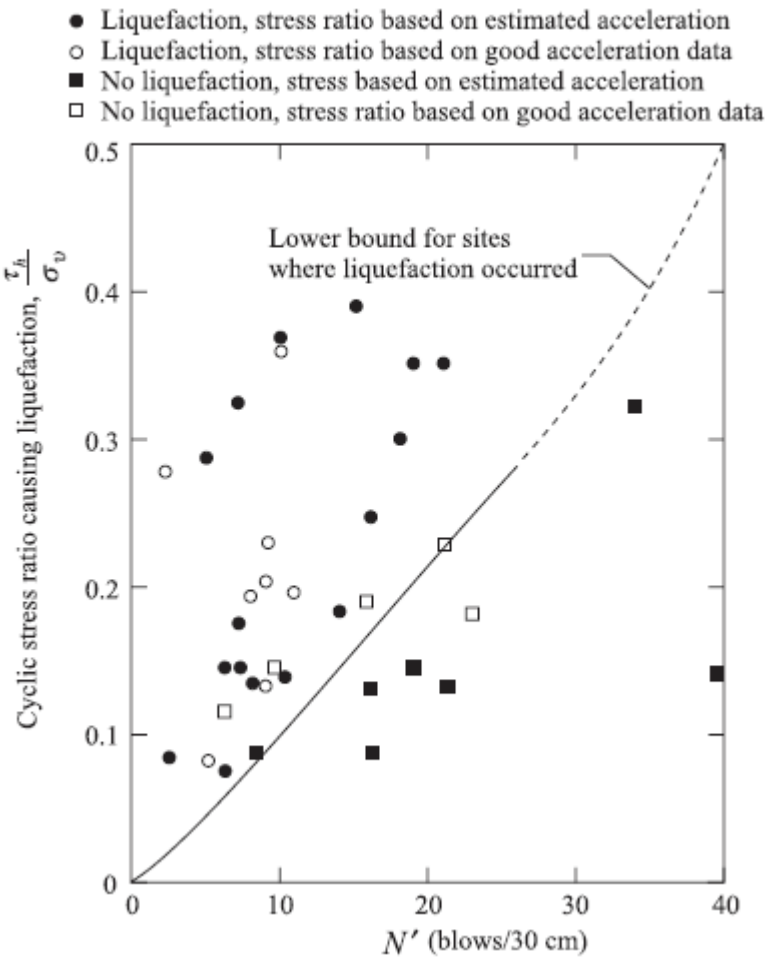

Figure 2.17: Correlation between τ_h / σ_v and N' (after Seed, 1979)

In order to develop a better correlation chart, Seed (1979) considered the results of the large-scale simple shear test conducted by DeAlba, Chan, and Seed (1976). These results were corrected to take into account the significant factors that affect the field condition, and they are shown in Table 2.1. It is important to realize that the $(\tau_h / \sigma_v)_{\text{test}}$ values listed in Table 2.1 are those required for a peak cyclic pore pressure ratio of 100% and cyclic shear strain of ±5%. Also, the correlation between R_D and N' shown in columns 1 and 2 are via the relationship established by Bieganousky and Marcuson (1977).

Excellent agreement is observed when the values of N' and the corresponding $(\tau_h / \sigma_v)_{\text{field}}$ values (columns 2 and 6) shown in Table 2.1 are superimposed on the lower-bound correlation curve shown in Figure 2.17. Hence the lower bound curve of Figure 2.17 is for an earthquake magnitude M = 7.5. Proceeding in a similar manner and utilizing the results shown in Table 2.1, lower-bound curves for M = 6, 7.5, and 8.25 can be obtained as shown in Figure 2.18.

Also shown in this figure is the variation of the limited strain potential in percent (for effective overburden pressure of 100 kPa). Figure 2.18 can be used for determination of the liquefaction potential in the field. In doing so, it is important to remember that

$$N' = C_N N_F \tag{2.39}$$

Table 2.1 : Data from Large-scale Simple Shear Tests on Freshly Deposited Sanda

		$M = 5-6$ 5 cycles		$M = 7-7.5$ 15 cycles		$M = 8-8.25$ 25 cycles	
Relative density, R_D	N' (blows/30 cm)	$\left(\frac{\tau_h}{\sigma_v}\right)_{test}$	$\left(\frac{\tau_h}{\sigma_v}\right)_{field}$	$\left(\frac{\tau_h}{\sigma_v}\right)_{test}$	$\left(\frac{\tau_h}{\sigma_v}\right)_{field}$	$\left(\frac{\tau_h}{\sigma_v}\right)_{test}$	$\left(\frac{\tau_h}{\sigma_v}\right)_{field}$
(1)	(2)	(3)	(4)	(5)	(6)	(7)	(8)
54	13.5	0.22	0.25	0.17	0.19	0.155	0.175
68	23	0.30	0.34	0.24	0.27	0.210	0.235
82	33	0.44	0.49	0.32	0.37	0.280	0.315
90	39	0.59	0.66	0.41	0.46	0.360	0.405

Note: N' = standard penetration resistance corrected to an effective overburden pressure of 100 kPa; M = magnitude of earthquake.

[a] After Seed (1979).

where

N_F = field standard penetration test values

C_N = correction factor to convert to an effective overburden pressure (σ'_v) of 100 kPa

The correction factor can be expressed as (Liao and Whitman, 1986)

$$C_N = 9.78\sqrt{\frac{1}{\sigma'_v}} \tag{2.40}$$

where σ'_v is in kPa.

A slight variation of Figure 2.18 is given by Seed, Idriss, and Arango (1983) and Seed and Idriss (1982). It can be seen from this figure that, if N' is more than 30, liquefaction is unlikely to occur, in general.

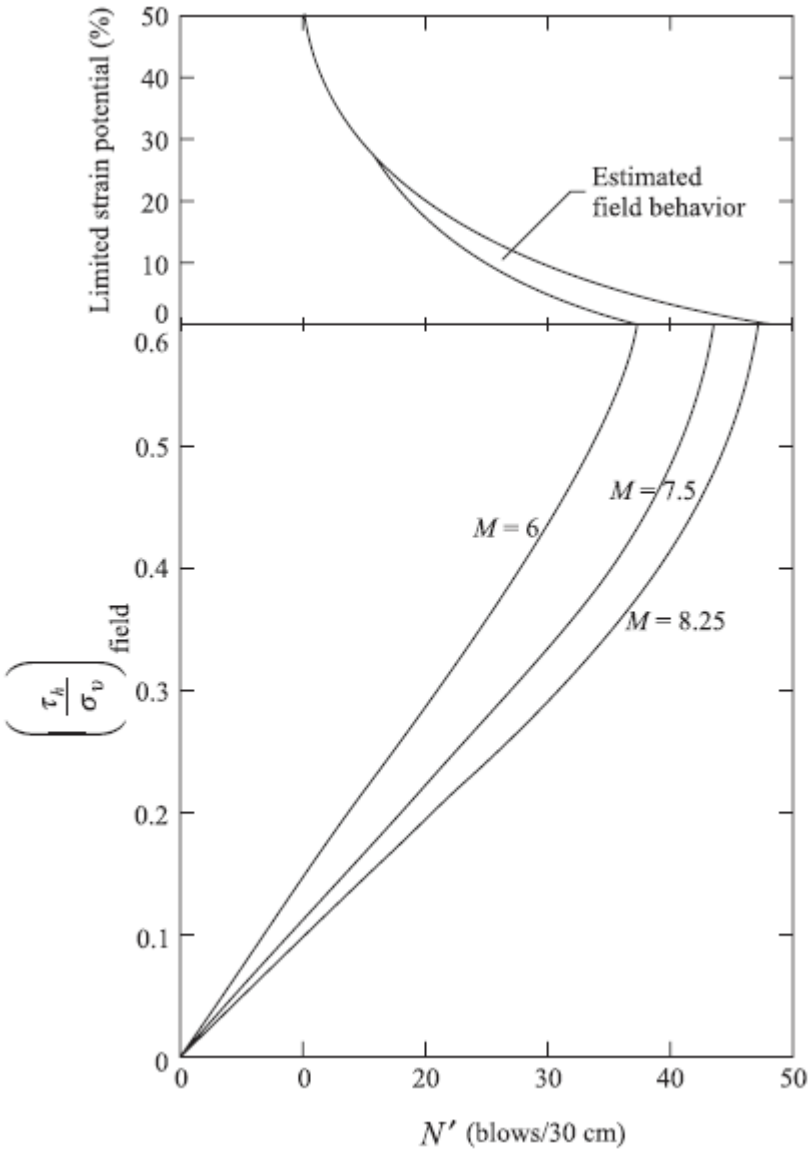

Figure 2.18: Variation of $(\tau_h / \sigma_v)_{field}$ with N' and M (after Seed, 1979)

Discussion regarding soil liquefaction has so far been limited to the case of clean sands; however liquefaction can, and has been observed in silty sands, mine tailings and silts. It is generally reported that mine tailings behave similar to clean sands under seismic loading. Information regarding the liquefaction of silty sand is somewhat limited and there is no consensus among the researchers as of date. In general, it is observed that liquefaction resistance of silty sands, up to certain silt content, is more than that of clean sands. It may be due to the fact that, voids in clean sands are occupied by silt particles and thus these may inhibit a quick volume change behavior. Seed et al. (1984) presented limited correlations between $(\tau_h / \sigma_v)_{field}$, N' and percent fines (F) for an earthquake magnitude M = 7.5, which can be summarized as follows:

Percent of fines, F	N'	Lower bound of $(\tau_h/\sigma_v)_{\text{field}}$ for which liquefaction is likely ($M = 7.5$)
≤5	5	0.055
	10	0.115
	15	0.170
	20	0.220
	25	0.295
	30	0.500
10	5	0.098
	10	0.160
	15	0.225
	20	0.295
	25	0.500
35	5	0.130
	10	0.185
	15	0.260
	20	0.400

2.3 Interaction of Soil and caisson quay wall

2.3.1 Mononobe-Okabe Active Earth Pressure Theory

In 1776, Coulomb derived an equation for active earth pressure on a retaining wall due to a dry cohesionless backfill, which is of the form

$$P_A = \frac{1}{2}\gamma H^2 K_A \tag{2.41}$$

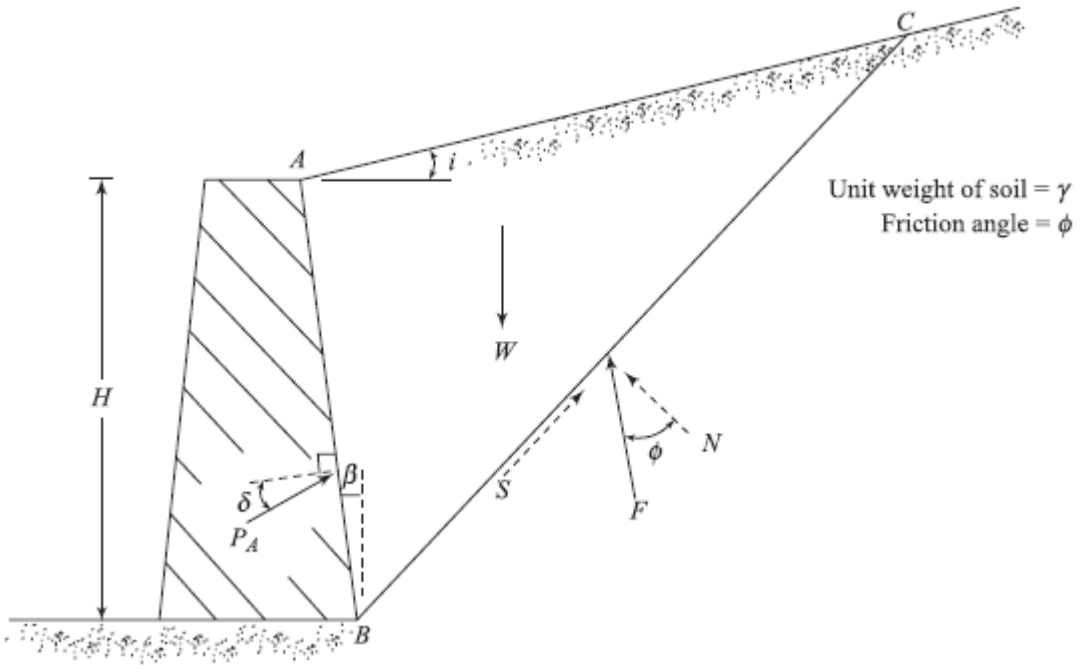

Figure 2.19: Coulomb's active earth pressure (*Note: BC* is the failure plane; *W* = weight of the wedge *ABC*; *S* and *N* = shear and normal forces on the plane *BC*; *F* = resultant of *S* and *N*)

where *PA* = active force per unit length of the wall
γ = unit weight of soil
H = height of the retaining wall
KA = active earth pressure coefficient

$$= \frac{\cos^2(\phi-\beta)}{\cos^2\beta\cos(\delta+\beta)\left[1+\left\{\frac{\sin(\delta+\phi)\sin(\phi-i)}{\cos(\delta+\beta)\cos(\beta-i)}\right\}^{1/2}\right]^2} \tag{2.42}$$

where φ = soil friction angle
δ = angle of friction between the wall and the
β = slope of the back of the wall with respect to the vertical
i = slope of the backfill with respect to the horizontal

Coulombs' active earth pressure equation can be modified to take into account the vertical and horizontal coefficients of acceleration induced by an earthquake. This is generally referred to as the *Mononobe-Okabe analysis* (Mononobe, 1929; Okabe, 1926). The Mononobe-Okabe solution is based on the following assumptions:

1. The failure in soil takes place along a plane such as *BC* shown in Figure 2.20
2. The movement of the wall is sufficient to produce minimum active pressure.
3. The shear strength of the dry cohesionless soil can be given by the equation

$$s = \sigma' \tan\phi \tag{2.43}$$

where σ' is the effective stress and s is shear strength.
4. At failure, full shear strength along the failure plane (plane *BC*, Figure 2.20) is mobilized.
5. The soil behind the retaining wall behaves as a rigid body.

Figure 2.20 shows the forces considered in the Mononobe-Okabe solution. Line *AB* is the back face of the retaining wall and *ABC* is the soil wedge which will fail. The forces on the failure wedge per unit length of the wall are

a. weight of wedge *W*,
b. active force P_{AE},
c. resultant of shear and normal forces along the failure plane *F*, and
d. $k_h W$ and $k_v W$, the inertia forces in the horizontal and vertical directions, respectively, where,

$$k_h = \frac{\text{horiz. component of earthquake accel.}}{g}$$

$$k_v = \frac{\text{vert. component of earthquake accel.}}{g}$$

and g is acceleration due to gravity.

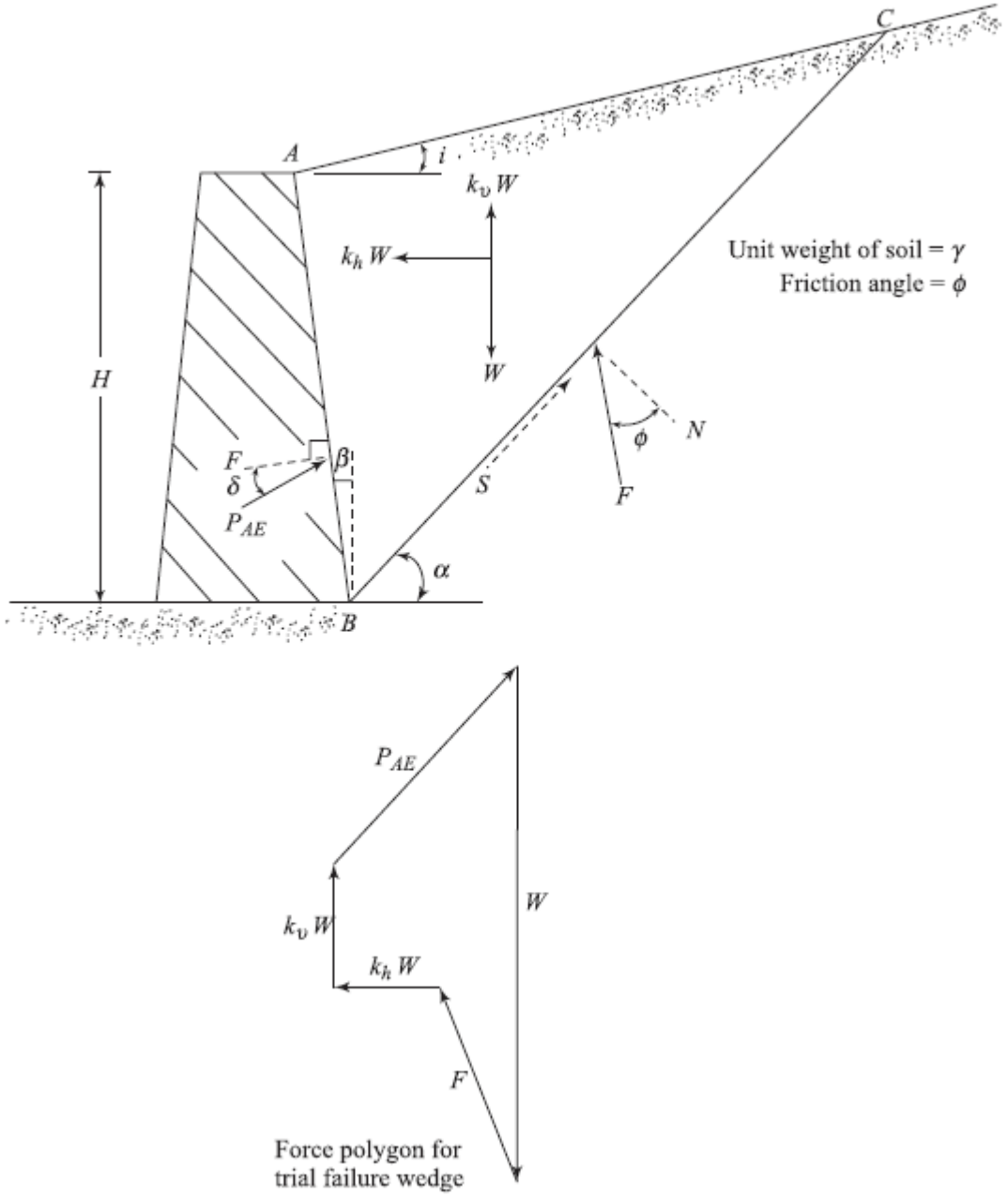

Figure 2.20: Derivation of Mononobe–Okabe equation

The active force determined by the wedge analysis described here may be expressed as

$$P_{AE} = \frac{1}{2}\gamma H^2 (1 - k_v) K_{AE} \tag{2.44}$$

where K_{AE} is the active earth pressure coefficient with earthquake effect:

$$K_{AE} = \frac{\cos^2(\phi - \theta - \beta)}{\cos\theta\cos^2\beta\cos(\delta + \beta + \theta)\left[1 + \sqrt{\frac{\sin(\phi + \delta)\sin(\phi - \theta - i)}{\cos(\delta + \beta + \theta)\cos(i - \beta)}}\right]^2} \tag{2.45}$$

$$\theta = \tan^{-1}\left(\frac{k_h}{1 - k_v}\right) \tag{2.46}$$

Equation (2.44) is generally referred to as the *Mononobe-Okabe active earth pressure equation*

The design seismic coefficient is not necessarily equal to the design level PGA/g due to the transient nature of the earthquake motions. The ratio of equivalent seismic coefficient k_e to PGA/g has been studied in the Port and Harbour Research Institute based on case histories (e.g., Noda *et al*., 1975; Nozu *et al.,* 1997). In these studies, the threshold seismic coefficients obtained by back analyses of a damaged and non-damaged structure at sites of non-liquefiable soils provide a lower and upper bound estimate for an equivalent seismic coefficient. The roots of the arrows in the figure, rather than the points, show the exact values. The arrows pointing up indicate lower bound estimates; those pointing down indicate upper bound estimates. The equation for an upper bound envelope was given by Noda *et al.* (1975) as

$$\begin{aligned} k_e &= \frac{a_{\max}}{g} && a_{\max} < 0.2g \\ k_e &= \frac{1}{3}\left(\frac{a_{\max}}{g}\right)^{\frac{1}{3}} && a_{\max} \geq 0.2g \end{aligned} \tag{2.47}$$

Below the water level, apparent seismic coefficient k_h', could be substituted in the above formulae to calculate θ. It is allowed to calculate the earth pressure acting below the residual water level during an earthquake according to the procedure stated before by using the apparent seismic coefficient that is determined by (PIANC,2001):

$$k' = \frac{2\left(\Sigma\gamma_t H_i + \Sigma\gamma_{sat} H_j + q_{sur}\right) + \gamma_{sat} . H_{sat}}{2\left[\Sigma\gamma_t H_i + \Sigma\gamma` H_j + q_{sur}\right] + \gamma` H_{sat}} k_h \qquad (2.47)$$

where: H_j Thickness of soil layer below the residual water level

H_i Thickness of the i-th soil layer above the residual water level

H_{sat} Thickness of soil layer to calculate earth pressure below the residual water level

γ_t Unit weight of backfill above the residual water level

γ_{sat} Unit weight of saturated soil layer below the residual water level

γ' Buoyant unit weight of backfill below the residual water level

q_{sur} Uniform surcharge on the backfill

k_h Horizontal seismic coefficient

Finally, the horizontal earth pressure acting on back-face of vertical wall during earthquake could be calculated by the following equation:

$$p_{ae} = k_{ae}\left[\Sigma\gamma H + q_{sur}\right] \qquad (2.48)$$

2.3.2 Effective Stress Numerical Analysis

Kobe Case History

The 1995 Hyogo-ken Nanbu (Kobe) Earthquake brought great damage to structures in the Port of Kobe, which is one of the primary ports in Japan (Figure2.21).
Most quay walls in Kobe were of the caisson type. They had been designed pseudo-statically, with seismic coefficients ranging from 0.10 to 0.25, depending on site conditions, year of construction, and the importance of the facility. They had been placed on top of gravelly fill consisting of decomposed granite (called locally 'Masado'), which had completely replaced the soft clay layer beneath the caisson for improving the bearing capacity and reducing settlements. The most severe damage occurred in those caisson walls of Port and Rokko Islands that: (a) were nearly parallel to the coastline (and thus parallel to the causative fault), and thereby experienced the stronger fault-normal accelerations (Somerville, 1998); and/or (b) had been designed with a small seismic coefficient, of 0.10 to 0.15. By contrast, the caisson wall of the main wharf at Maya Futo, designed conservatively with a large seismic coefficient of 0.25 and running almost perpendicular to the fault (and thereby having been subjected to some less severe accelerations parallel to the fault), did not experience any visible damage or substantial deformation, remaining operational after the earthquake. It is worth mentioning that, despite the large deformations, the caissons did not overturn. Their overall performance can be judged as better than that of the alternative quay wall system, the anchored sheet-pile wall, which in earlier earthquakes that were much less devastating than the Kobe 1995 earthquakes were frequently experiencing collapsing failures.

After the 1995 Hyogo-ken Nanbu (Kobe) Earthquake, it has been recognized that, although the pseudo-static analysis for caisson quay walls is effective for the serviceability-level design ground motion, it is not applicable for the level II design ground motion, which is a safety-level design ground motion, because of its intensity. Thus a need was recognized for a more sophisticated analysis, in which seismic performance of a quay wall beyond the limit of force-balance can be assessed. For this reason, the effective-stress analysis for quay walls was incorporated in the latest version of the technical standards for port and harbour facilities in Japan (Ministry of Transport, Japan, 1999). Effective-stress analysis, generally using a finite element technique, involves coupled soil-structure interaction wherein the response of the foundation and backfill soils is incorporated in the computation of the structural response.

While the stress-strain behavior of the soil is idealized with an effective-stress constitutive model (e.g., Iai *et al*., 1992), modeling of a caisson itself is generally accomplished using a linear model. Fairly comprehensive results can be obtained from the effective-stress analysis, including failure modes of the soil-structure systems and extent of residual deformation of the system.

Figure 2.21: Damage to a quay wall at the Port of Kobe during the 1995 Hyogo-ken Nanbu Earthquake

The case history corresponds to the typical quay wall section of Rokko Island, in which both the foundation and backfill soils are liquefiable. A cross-section of the quay wall with its deformation recorded after the earthquake is reproduced from Iai et al. (1998) in Fig. 2.22. The finite-difference discretisation and the material zones used in our analyses are shown in Fig. 2.23. During the earthquake the wall top displaced approximately 4 m seaward (exceeding 5 m in a few locations). It settled about 1–2 m and tilted about 4o outwards. Despite these significant movements, the site investigation showed no collapse of the wall along its entire length. Also, no evidence was observed of liquefaction either within a zone extending about 30 m behind the wall or near the toe of the wall in the sea. However, evidence of liquefaction was abundant farther away in the free field. Investigation by divers cited by Inagaki et al. (1996) revealed substantial heaving of the foundation rubble at a distance of 2–5 m in front of the toe of the caisson—indicative of 'squeezing out' of the soil underneath the edge (toe) of the tilting caisson. [Dakoulas, P. & Gazetas, G. (2008)]

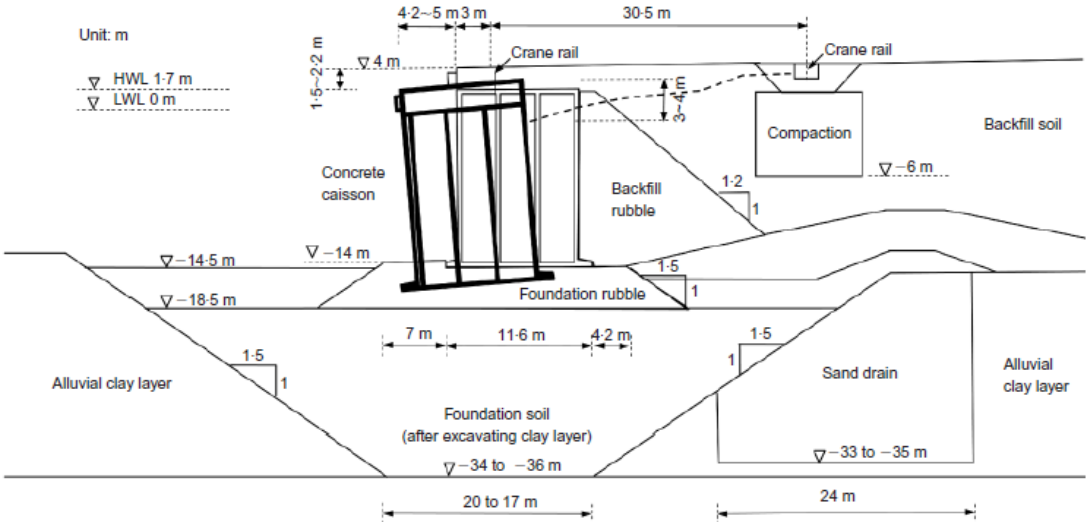

Figure 2.22: Cross-section of caisson quay wall RC-5 in Rokko Island and its residual deformation observed after Kobe 1995 earthquake(from Iai et al., 1998)
[Dakoulas, P. & Gazetas,G. (2008)]

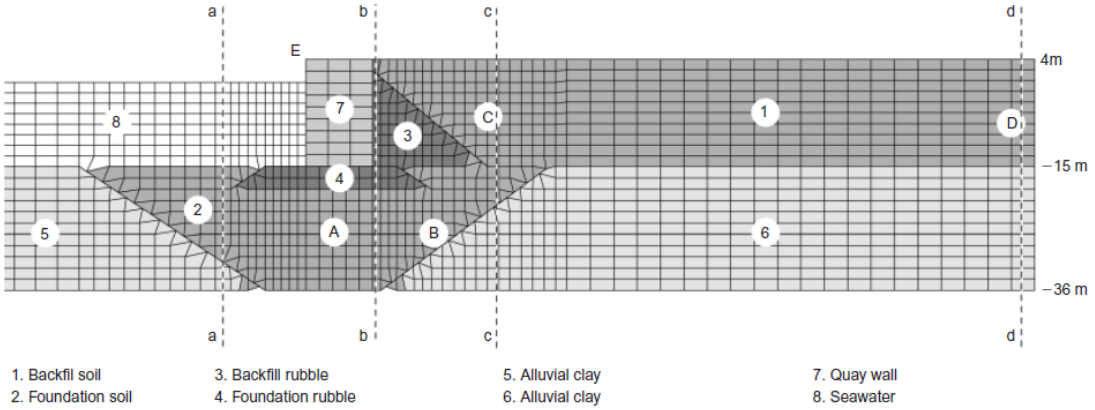

Figure 2.23: Geometry (in natural scale), finite difference discretisation, and material zones of Rokko Island quay wall system. Points A, B,C and D and lines aa, bb, cc and dd are for showing details of pore water pressures and displacements [Dakoulas, P. & Gazetas, G. (2008)]

Interaction between caisson quay wall, seismic earth and water pressures

Comprehensive theoretical and experimental research has shed light on the complicated behavior of the quay wall–soil system. Among the most significant findings of the research so far are the following.

- The displacement of the wall could be attributed to two factors:
  - the significant lateral pressures from the backfill and the large inertia of the wall itself, as the driving forces
  - the strongly inelastic deformation of the foundation soil, allowing the caisson to move and tilt, as the supporting soil beneath the caisson was 'pushed out' (Iai et al., 1998).

- Liquefaction occurred only in the free field away from the wall, not in the backfill next to the wall. In the foundation soil, on the other hand, very substantial excess pore water pressures developed, undermining its stiffness and strength. This facilitated the lateral translation and rotation of the wall, even though 'complete' liquefaction did not develop.

- Of the two driving forces, the wall inertia played the most detrimental role, whereas the earth and water pressures from the backfill were of lesser importance

- The outward movement of the caisson stopped at the end of shaking—an analytical and experimental finding consistent with the previous conclusions. This provides further evidence that the whole phenomenon is driven mainly by wall inertia and not by liquefaction flow. In fact, use of the term 'lateral spreading' for the deformations observed behind the quay walls may not be suitable for describing the whole phenomenon.

For the quay walls that are of interest here, in particular, the situation becomes far more complicated because of the following four phenomena that occur simultaneously:

- The development of oscillatory wall inertia loading, which tends to produce outward displacement and rotation of the wall due to the compliance of the supporting soil.

- The simple-shear deformation of the backfill from the (incident and reflected) vertically propagating shear waves, which tends to generate positive excess pore water pressures $+\Delta u$ in the (usually loose)

underwater placed soils. In the free field, the accumulated build-up of such pressures may lead to liquefaction.

- Extensional normal deformation of the backfill soil adjacent to the wall, as the wall moves outwards. This tends to generate negative excess pore water pressures -Δu, which may or may not overshadow the positive seismic pore water pressures, depending on the amount and speed of the wall movement, as well as on the density of soil. (Dense dilatant soil in extension may develop exceedingly large negative water pressures.)

- The tendency to continuous dissipation and redistribution of pore water pressures (flow in two dimensions), eventually resulting in a detrimental 'contamination' of the regions of negative excess pore water pressure (which therefore become neutralized or even change their sign to positive) towards the end of shaking.

Evidently, the whole problem is very complex, and with the present state of knowledge there is no clear understanding of how sensitive each of the above simultaneous phenomena is to variations in soil characteristics (imperfectly known in reality) such as the relative density and the coefficient of permeability of the various constituent soils.

[Dakoulas, P. & Gazetas, G. (2008)]

2.4 Fragility Curves

2.4.1 Fragility definition

Evaluation of the seismic risk at a port requires a thorough assessment of the vulnerability of a wharf, which can be most effectively done through the use of fragility curves. Using the information on the demand and capacity of the systems, fragility curves provide the probability that the structure under consideration will fail to satisfy a performance limit or a set of limits at a given intensity measure of earthquake disturbance. In this study, analytical fragility curves for typical pile supported wharves on the west coast of the United States are developed using nonlinear time-history analysis on detailed foundation-wharf models for various seismic hazard scenarios.

In general, fragility functions are probability distributions that indicate the probability that a structural system or component will be damaged to a predefined damage state as a function of an engineering demand parameter (EDP). Herein, fragility functions take the form of lognormal cumulative distribution functions, having a median value α and logarithmic standard deviation, β. The mathematical form for a fragility function, which associates the probability that the structural component may be damaged to damage state "i" with the maximum ground acceleration, is:

$$F(PGA)=\Phi\left[\frac{1}{\beta_c}\cdot\ln\left(\frac{PGA}{Ai}\right)\right] \qquad (2.48)$$

Where

$\Phi(_)$: is the standard normal cumulative distribution function.

PGA : is the maximum ground acceleration whose value gives a corresponding probability of failure referring to particular damage states

A_i : is the median value of the probability distribution.

β_c : is the logarithmic standard deviation.

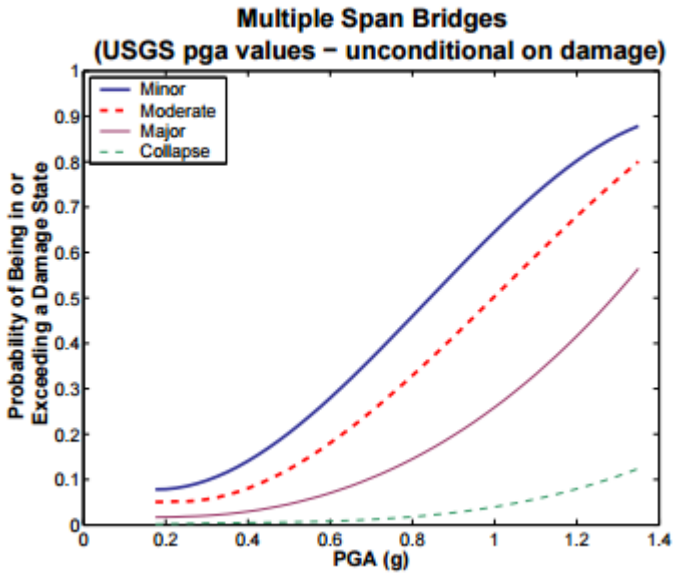

Figure 2.23: Fragility Curve Example for Multi-Span Bridges (Basoz and Kiremidjian, 1997)

2.4.2 Fragility criteria for Quay Walls

PIANC, the World Association for Waterborne Transport Infrastructure, distinguishes four degrees of damage criteria for gravity quay walls:

- Degree I: "Serviceable", where the residual horizontal displacement should be less than 1,5% of the height of the quay wall and the residual tilt should be less than 3º
- Degree II: "Repairable", where the residual horizontal displacement should be 1,5%-5% of the height of the quay wall and the residual tilt should be 3º-5º
- Degree III: "Near collapse", where the residual horizontal displacement should be 5%-10% of the height of the quay wall and the residual tilt should be 5º-8º
- Degree IV: "Collapse", where the residual horizontal displacement should be larger than 10 % of the height of the quay wall and the residual tilt should be larger than 8º

Chapter 3
Numerical Modeling

2.1 Finite Element Program

PLAXIS 2D is a special purpose two-dimensional finite element program used to perform deformation and stability analysis for various types of geotechnical applications. Real situations may be modeled either by a plane strain or an axisymmetric model. The program uses a convenient graphical user interface that enables the user to quickly generate a geometry model and finite element mesh based on a representative vertical cross section of the situation at hand.

The user interface consists of two sub-programs (Input and Output)

The Input program is a pre-processor, which is used to define the problem geometry, to create the finite element mesh and to define calculation phases.

The Output program is a post-processor, which is used to inspect the results of calculations in a two dimensional view or in cross sections, and to plot graphs (curves) of output quantities of selected geometry points.

A general overview for starting the input program, i.e. general model properties and the layout of the input program is perfectly composed in the PLAXIS2D Reference Manual.

General overview of Input program

The soil stratigraphy is defined in the soil mode using the Borehole feature of the program (Figure 3.1). When a new project is created, the soil contour defined in the Project properties window is displayed in the draw area. Otherwise, the soil stratigraphy can be defined in the Structures mode by selecting *Create soil polygon* option, which creates a general polygon by specifying the points that define the polygon (Figure 3.2).

In order to define distributed prescribed displacements, the *Create line displacement* option should be selected from the menu appearing as the *Create prescribed displacement* button is selected. The options for the components of line prescribed displacement are *Free, Fixed* and *Prescribed.* These options can be selected in the *Model explorer* (Figure 3.2).

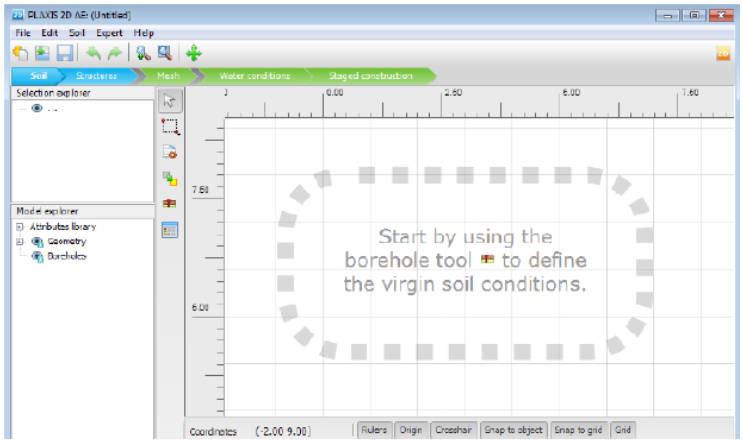

Figure 3.1: View of a new project in the Soil mode

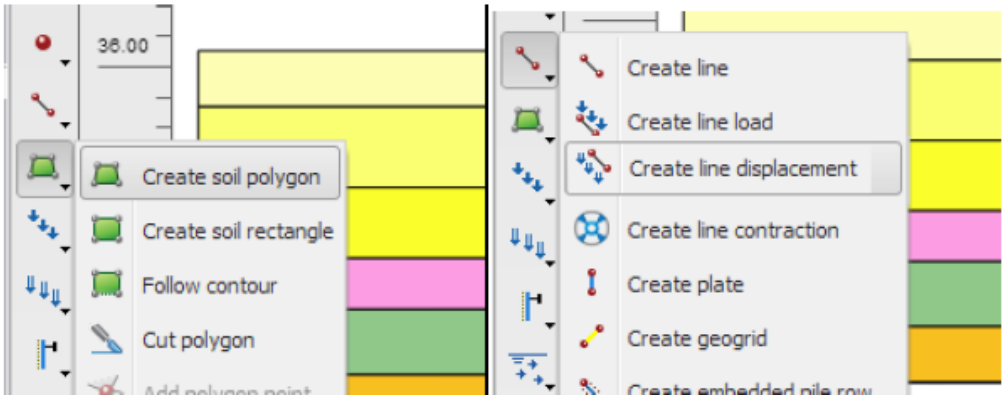

Figure 3.2: View of the Structures mode (ground modeling and load modeling)

Soil properties and material properties of structures are stored in material data sets. There are four different types of material sets grouped as data sets for soil and interfaces, plates, geogrids, embedded pile rows and anchors (Figure 2.3). The material properties and model parameters for soil clusters are entered in material data sets. The properties in the data sets are divided into five tabsheets: *General, Parameters, Flow parameters, Interfaces* and *Initial* (Figure 2.4).

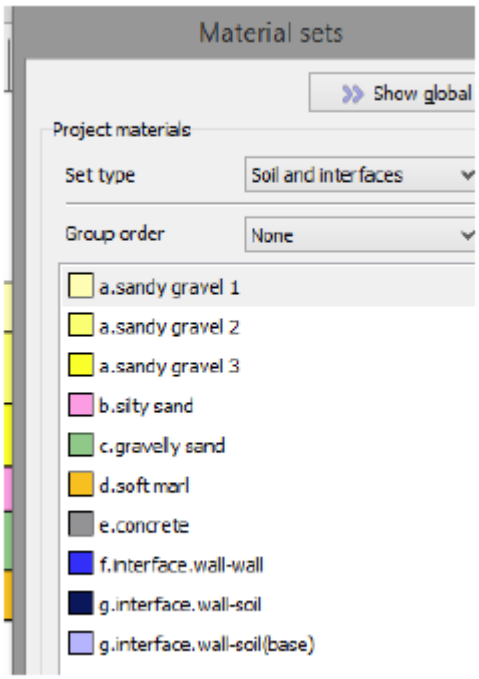

Figure 3.3: Material sets window

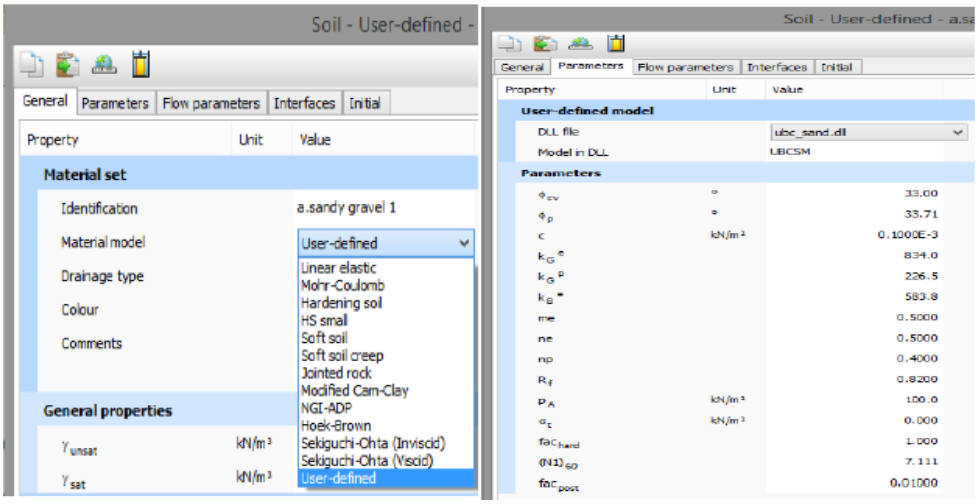

Figure 3.4: *General* and *Parameters* tabsheet from Soil Window

When the geometry model is fully defined, the geometry has to be divided into finite elements in order to perform finite element calculations. A composition of finite elements is called a mesh. The mesh is created in the *Mesh* mode (Figure 2.5). The mesh should be sufficiently fine to obtain accurate numerical results. On the other, very fine meshes should be avoided since this will lead to excessive calculation times. The generation of the mesh is based on a robust triangulation procedure. The mesh generation process takes into account the soil stratigraphy as well as all structural objects, loads and boundary conditions.

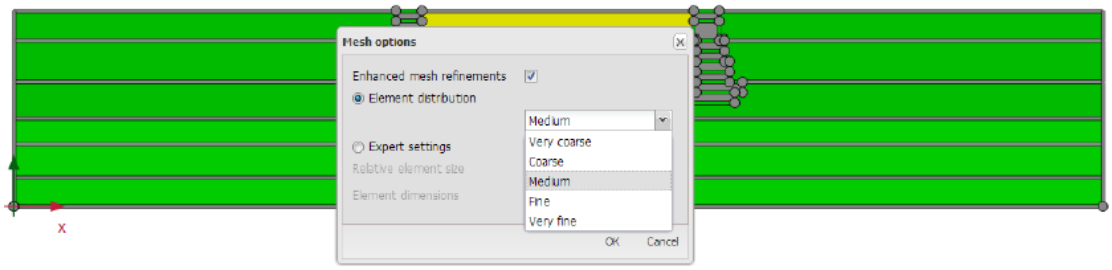

Figure 3.5: *Mesh options* window

The *Global water level* can be used to generate a simple hydrostatic pore pressure distribution (Phreatic calculation type) for the full geometry (Figure 2.6). The global water level is by default assigned to all clusters in the geometry.

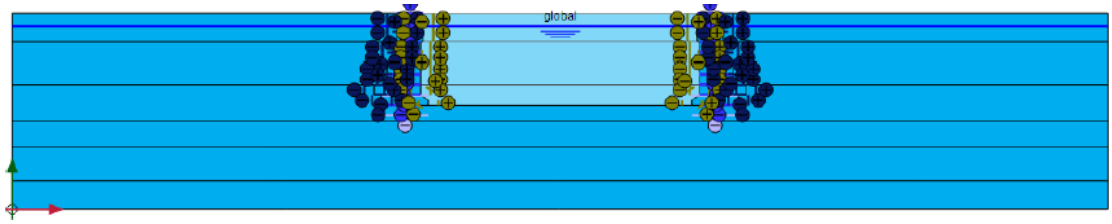

Figure 3.6: *Global water level*

Finite element calculations can be divided into several sequential calculation phases. Each calculation phase corresponds to a particular loading or construction stage. The construction stages can be defined in the *Staged construction* mode and the calculation phases are listed in the *Phases explorer*.

In the *Initial phase* (Figure 3.7), all the soil clusters are activated and all the interfaces are deactivated. It is crucial to mention that in this phase there are soil clusters activated even in front of the quay walls. In this phase the *K0 procedure* is used to define the initial stresses for the model, taking into account the loading history of the soil. The parameters required in the initial stresses development procedures are defined in the *Initial* tabsheet of material data sets for soil and interfaces (Figure 3.8).

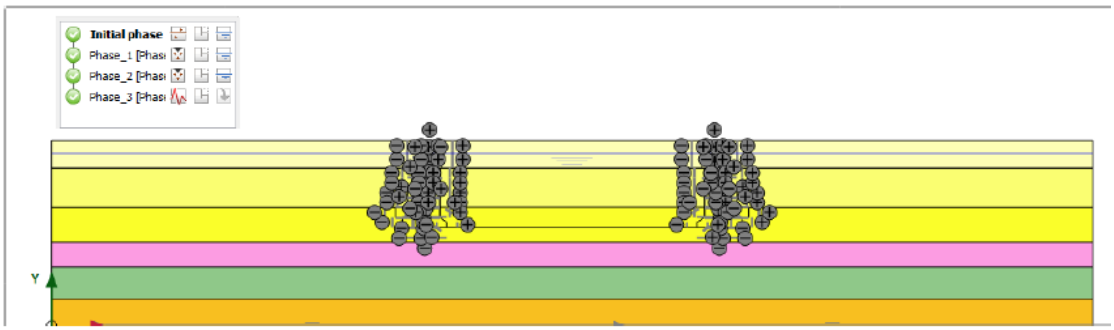

Figure 3.7: *Initial phase*

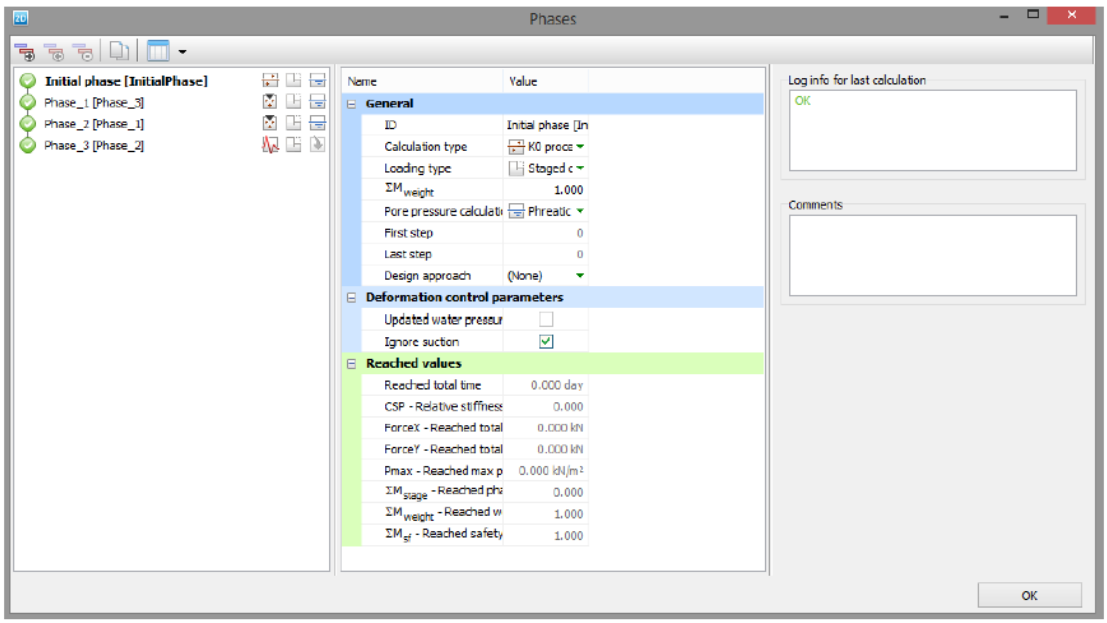

Figure 3.8: Parameters for the *Initial phase*

In the first phase (*Phase 1*) the soil clusters in front of the quay walls are deactivated in order the water to replace them (Figure 2.9) and all the interfaces remain deactivated. The *Plastic calculation* is used to carry out an elastic-plastic deformation analysis in which it is not necessary to take the change of pore pressure with time into account. An elastic-plastic deformation analysis where undrained behavior (*Undrained (A)* or *Undrained (B)*) is temporarily ignored, can be defined be selecting the *Ignore undrained behavior (A, B)* parameter. In this case the stiffness of water is not taken into account.

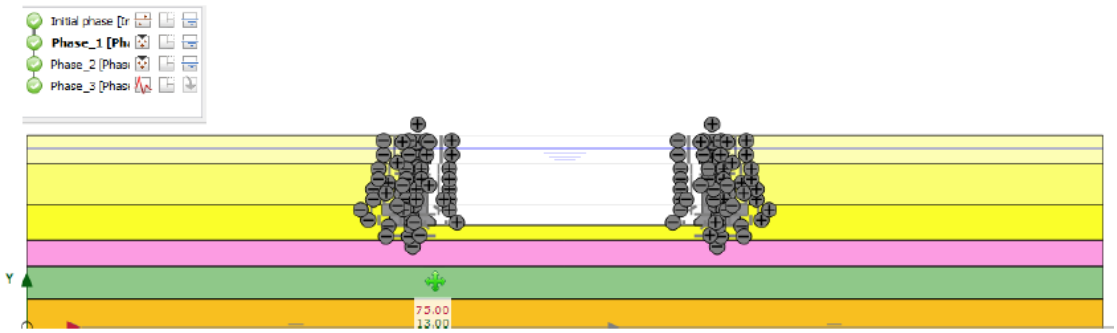

Figure 3.9: Fist phase (*Phase 1*)

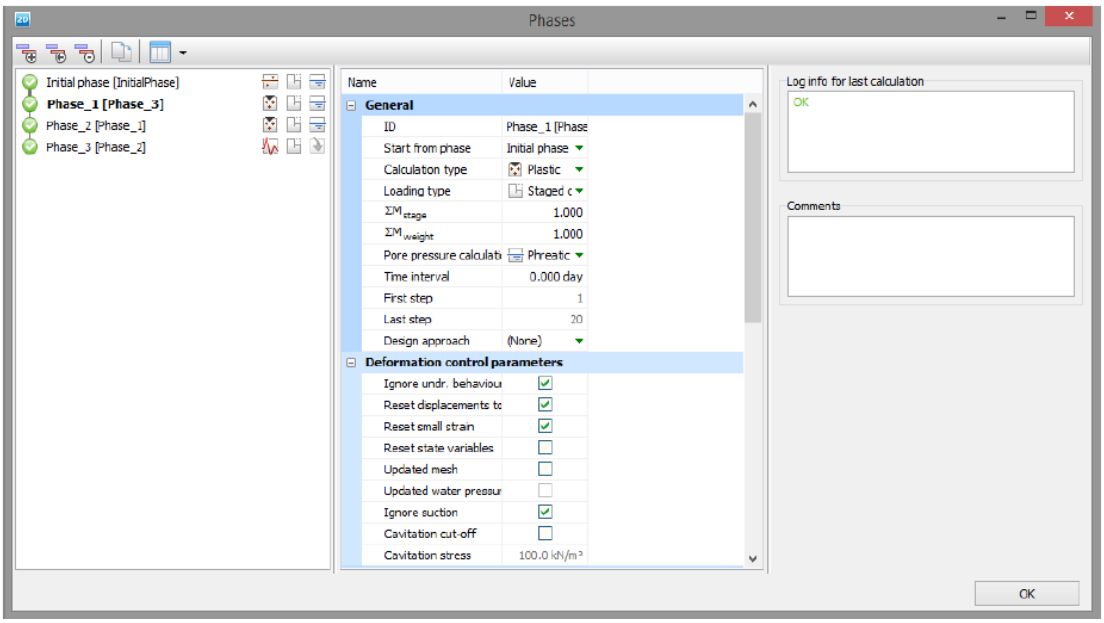

Figure 3.10: Parameters for the First phase *(Phase 1)*

In the third phase (*Phase 3*) the soil clusters in front of the quay wall remain deactivated and the interfaces in the back and the base of the quay wall remain activated. In this last phase the prescribed line displacement is activated (Figure 3.13). In this phase the *Dynamic calculation* is selected in order to consider stress waves and vibrations in the soil. As far as the ignorance of the undrained behavior is concerned, the *Ignore undrained behavior (A, B)* option has to be deselected (Figure 3.14). As for the time step used in a *Dynamic* calculation, it is constant and equal to $\delta t = \Delta t / (m*n)$, where Δt is the duration of the dynamic loading (*Dynamic time interval*), *m* is the value of *Max steps* and *n* is the value of the *Number of sub steps* parameter. The *Max steps* parameter specifies the number of the steps that are stored which can be used in plots in the Output program. A higher value of the *Max steps* parameter provides more detailed plots and animations, however the processing time required by the Output program is increased as well (Figure 3.15).

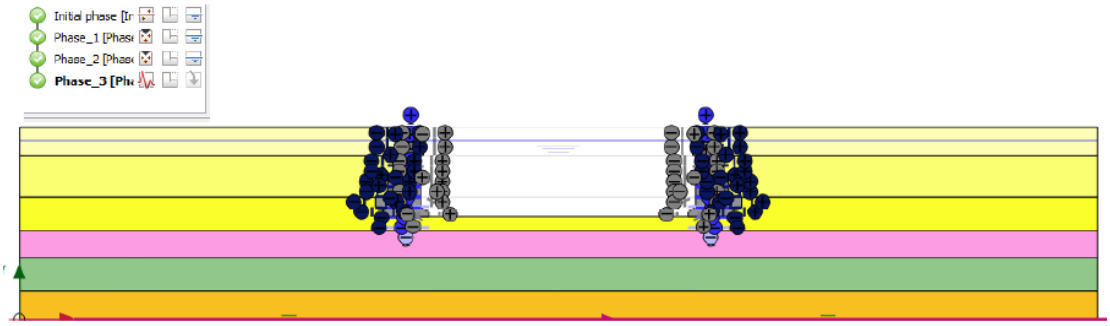

Figure 3.13: Third phase (*Phase 3*)

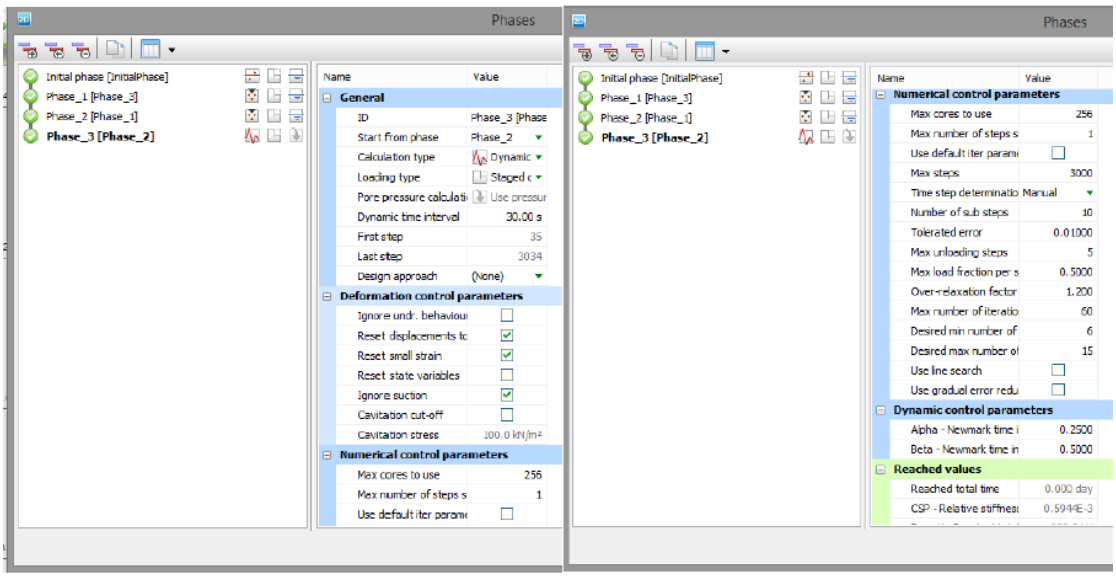

Figure 3.14: Parameters for the Third phase (*Phase 3)*

The *Model explorer* displays information related to the physical entities composing the model.

In the Dynamics option, the model conditions for a dynamic analysis can be defined at the extreme boundaries of the model. The options available for the X-axis boundaries are *None*, *Viscous*, *Free-field* and *Tied degrees of freedom*. The options available for the Y-axis boundaries are *None, Viscous* and *Compliant base*. (Figure 3.15)

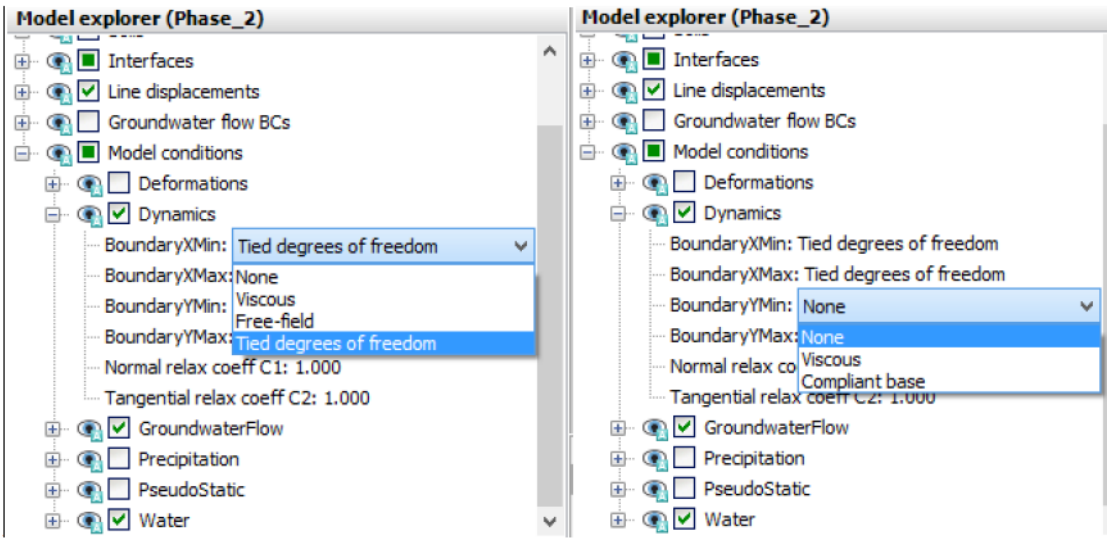

Figure 3.15: *Model explorer*

The *Selection explorer* displays information about the selection made in the draw area.

Although the input values of prescribed displacements are specified in the *Structures* mode, the activation, deactivation or change of values may be considered in the framework of *Staged construction* in the *Selection explorer.* For a dynamic prescribed displacement representing an excitation, $Displacement_x$ should be *Prescribed* and $Displacement_y$ should be *Fixed* (Figure 3.16).

Dynamic multipliers can be assigned to a prescribed displacement. The dynamic multipliers to be applied in the model can be defined in the *DynLineMultiplier* subtree under the Line *displacement* in the *Selection explorer (*Figure 3.16). The definition of the multipliers is made in the *Multipliers* window. Besides the harmonic signal, there is also the possibility to define a signal by specifying the values in the table that appears when the corresponding option is selected in the *Signal* drop-down menu. Besides defining the signal in the table, there is also the

possibility to read data from a file with a digitized load signal using the *Open* button in the toolbar (Figure 3.17).

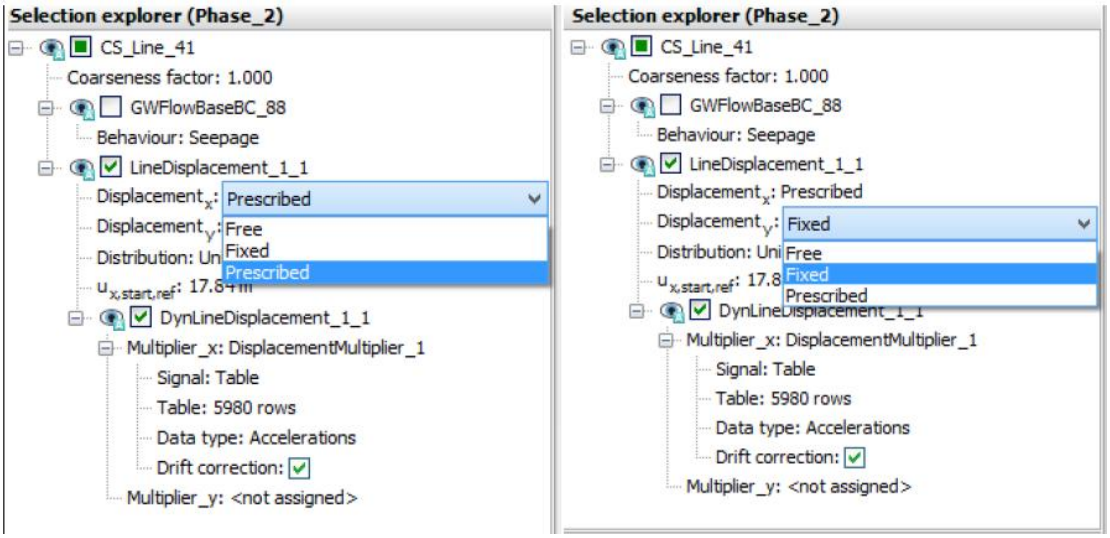

Figure 3.16: *Selection explorer*

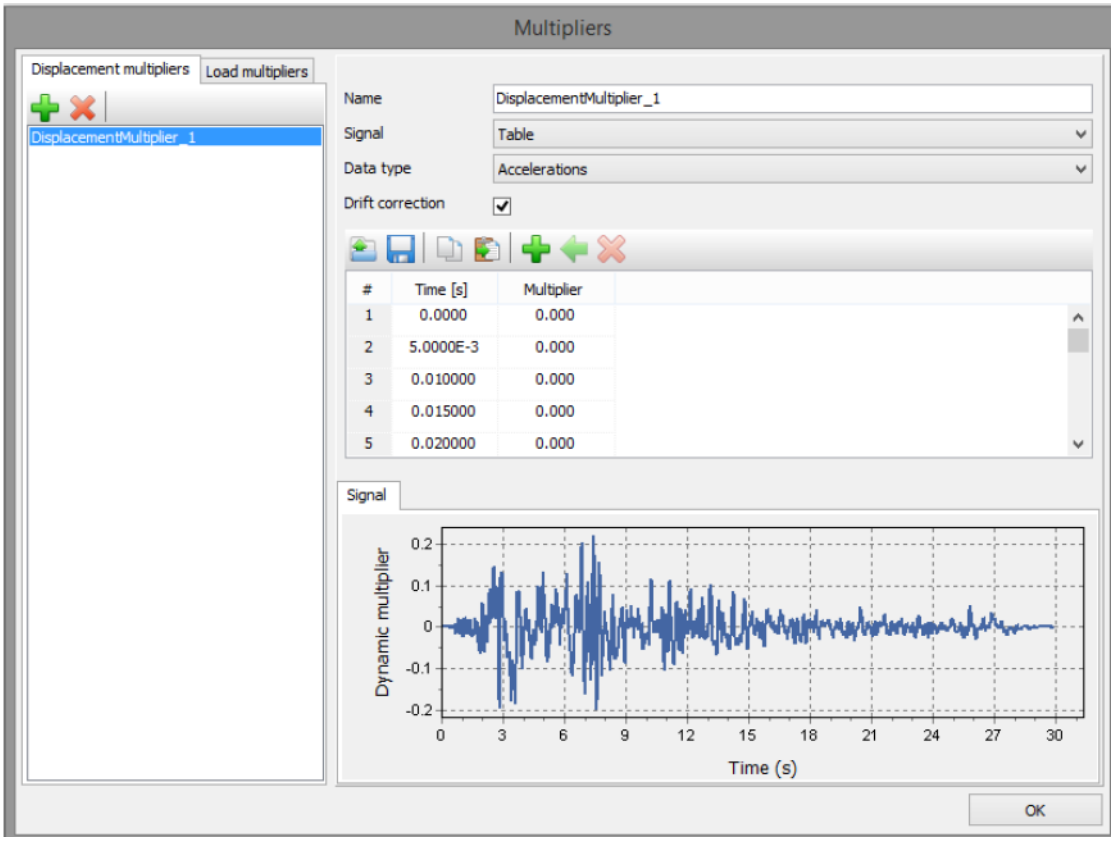

Figure 3.17: *Dynamic multipliers* window

After the calculation phases have been defined and before the calculation process is started, some points may be selected by the user for the generation of load-displacement curves or stress paths by clicking the *Select points for curves* button (Figure 3.18).

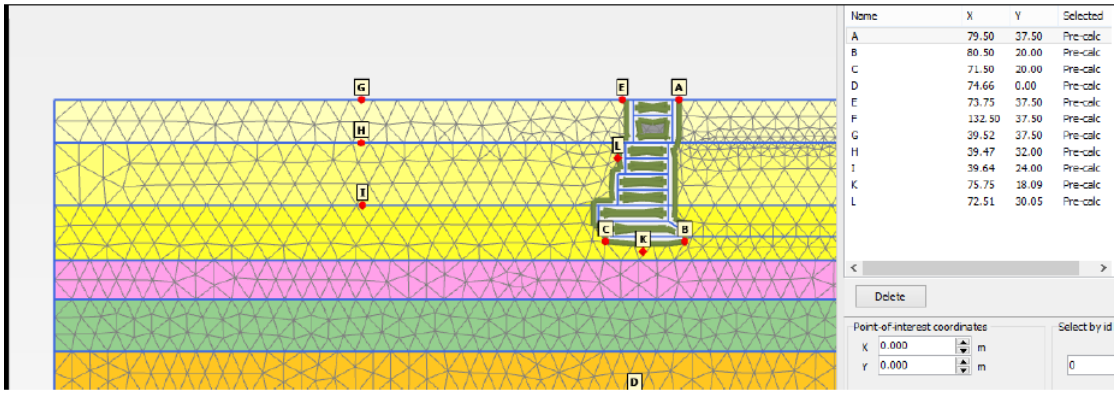

Figure 3.18: Example of points selected for pre-calculation

Finally, the calculation process can be started by clicking the *Calculation* button in the tool bar. As a result the program first performs a check on the ordering and consistency of the calculation phases. When a calculation phase is selected that has been executed, the tool bar will show the *View results* button. Clicking this button will directly display the results of the selected phase in the Output program (Figure 3.19).

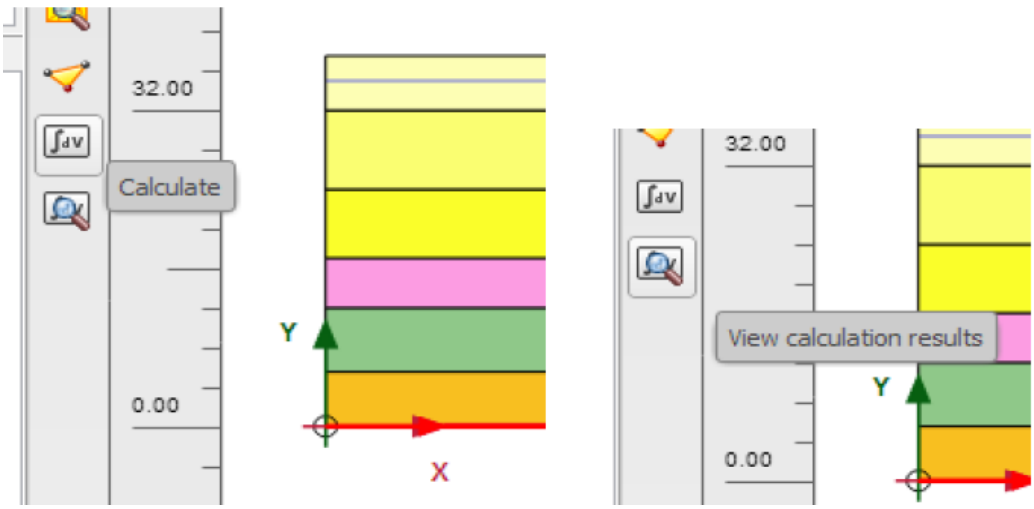

Figure 2.19: *Calculation* and *View results* buttons

3.2 Boundaries

With the ultimate purpose to define the boundary conditions that would be selected for the thesis model, a dynamic calculation has been processed by PLAXIS2D on a soil column (Figure 3.20), in which two *Material models* have been used, the linear elastic and the Hardening Soil small (HSsmall) (non-linear). This layer is based either on a *Rigid base* or on a *Compliant base*. As far as the X-axis is concerned, *Free field* and *Tied degrees of freedom* options have been tested.

The dimensions of the soil column are 2m * 20m, the damping that has been used is ξ = 5% and the parameters of the soil is presented in Figures 3.21 and 3.22. Regarding the linear elastic model, the main parameters that are inserted in the *Parameters* tabsheet, according to which the others are defined is the velocity V_S=140m/s and the Poisson ratio ν=0,3. As for the HSsmall model, the main parameters are E_{50}^{ref} , E_{OED}^{ref} and E_{ur}^{ref} , as well as $\gamma_{0.7}$.

The fundamental frequency of both models is given by f_1 = Vs / (4*H) and the next frequencies are given by f_i = i * f1, i.e. f_2 = 2 * Vs / (4*H) etc. The *Mode shapes* of the first four frequencies are given in Figures 3.23 and 3.24 for the linear elastic and the Hssmall model, respectively. This is the first evidence that the dynamic response of the soil column is in the right direction.

When using the *Free field* boundary condition we need to create so called node pairs along the boundary of the model (for this we manually need to create an interface along the boundary). Between the two nodes of a node pair a viscous damper is created which allows for transfer of the input and/or free field motion but also allows for absorbing the incoming waves. Currently however we can by default only see one side of this node pair in the Output program: this is the side of the viscous damper that also moves due to absorption of incoming waves. So in general the motion of this node is not equal to the input motion. To be able to see and to explicitly check our input motion we should make the other node of the node pair visible in Output. To do so we can make use of a trick with a "dummy plate". This is why between the X-axis boundaries *Free field* and *Tied degrees of freedom*, the later is selected in this thesis as the simpler one.

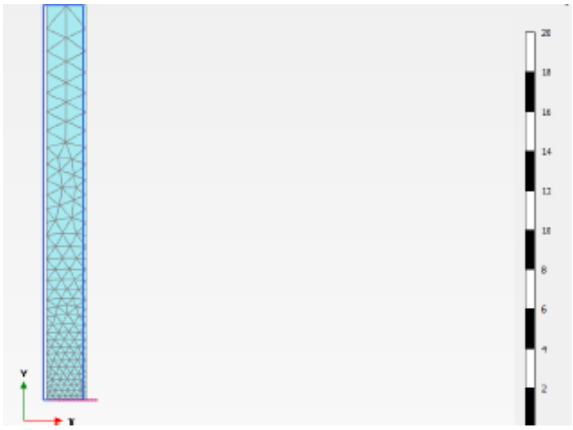

Figure 3.20: Soil column

General | Parameters | Flow parameters | Interfaces | Initial

Property	Unit	Value
Material set		
Identification number		1
Identification		soil
Material model		Linear elastic
Drainage type		Drained
Colour		RGB 161, 226, 232
Stiffness		
E	kN/m²	103.9E3
ν (nu)		0.3000
Alternatives		
G	kN/m²	39.96E3
E_{oed}	kN/m²	139.9E3
Velocities		
V_s	m/s	140.0
V_p	m/s	261.9

Figure 3.21: Soil parameters for the Linear elastic model

Material set		
Identification number		1
Identification		soil
Material model		HS small
Drainage type		Drained
Colour		RGB 161, 226, 232
Stiffness		
E_{50}^{ref}	kN/m²	500.0
E_{oed}^{ref}	kN/m²	500.0
E_{ur}^{ref}	kN/m²	1000
power (m)		0.5000
Alternatives		
Use alternatives		☐
C_c		0.6900
C_s		0.3105
e_{init}		0.5000
Strength		
c_{ref}	kN/m²	5.000
φ (phi)	°	32.00
ψ (psi)	°	0.000

Small strain		
$\gamma_{0.7}$		5.000E-3
G_0^{ref}	kN/m²	39.00E3
Advanced		
Set to default values		☐
Stiffness		
ν_{ur}		0.2000
P_{ref}	kN/m²	100.0
K_0^{nc}		0.5000
Strength		
c_{inc}	kN/m²/m	0.000
y_{ref}	m	0.000
R_f		0.9000
Tension cut-off		☑
Tensile strength	kN/m²	0.000
Failure criterion		
Failure criterion		Mohr-Coulomb

Display units | Next

Figure 3.22: Soil parameters for the Hssmall model

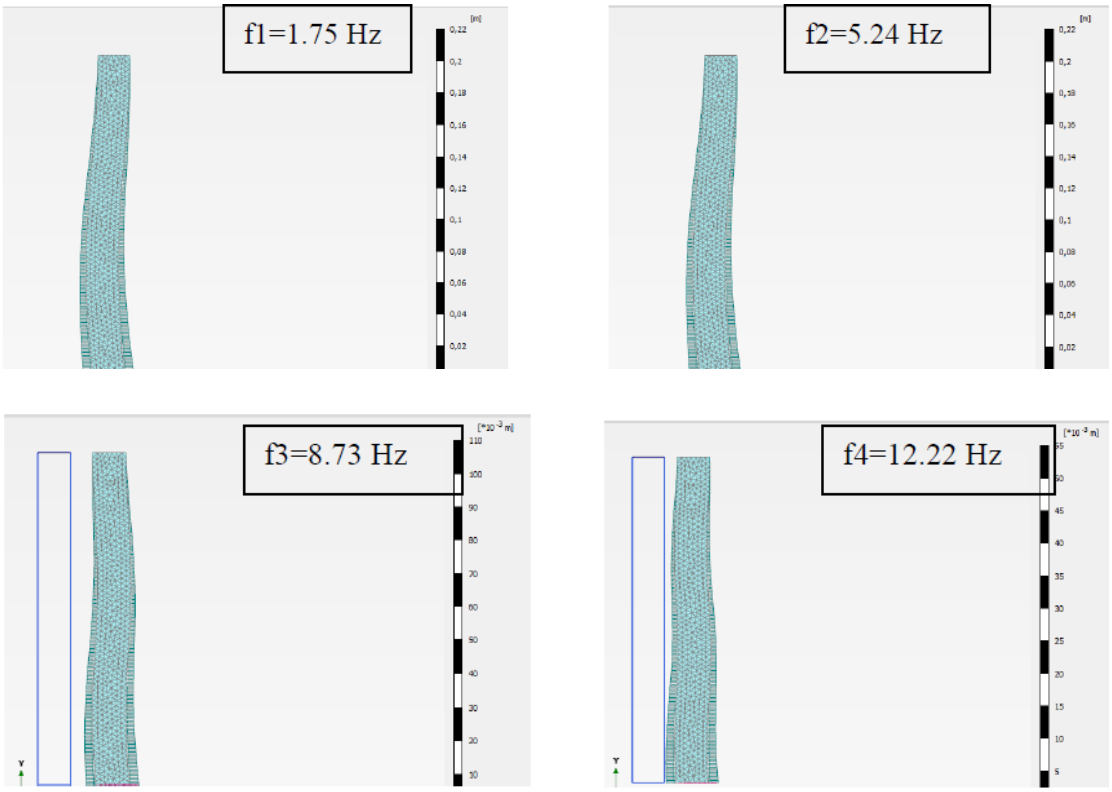

Figure 3.23: Mode shapes for the linear elastic model

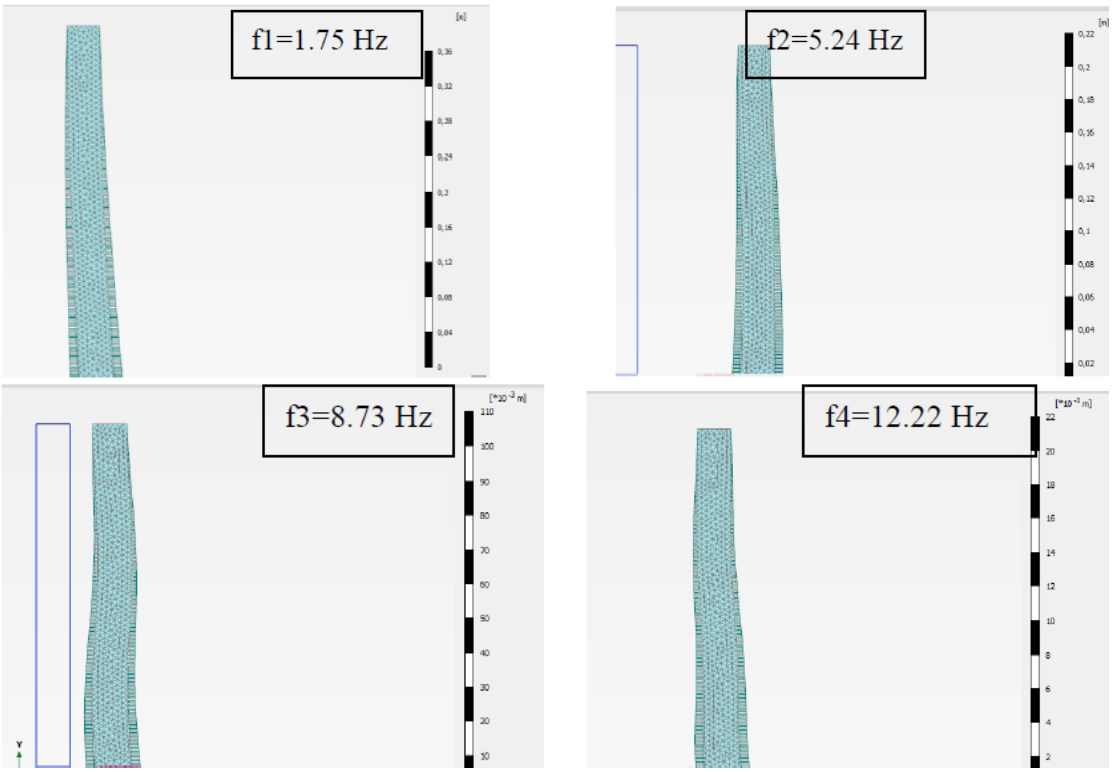

Figure 2.24: Mode shapes for the HSsmall model

The calculation of the *Transfer functions* follows in order to prove that the boundaries conditions used in this thesis are adequately functional. In Figure 3.25 and 3.26 the amplification functions of the linear elastic and the HSsmall models, respectively, are presented. In both soil columns *Tied degrees of freedom* boundary condition is selected for the X-axis and the Y-axis boundaries are either *Rigid base* or *Compliant base.*

In the case where the *Free field* boundary condition is selected, the soil column has exactly the same dynamic response

It can be observed that when compliant base boundary is selected, there is no amplification of the amplitude of the base, due to the fact that the compliant base absorbs the downward travelling stress waves so that they are partially reflected, thus part of their energy will be transmitted through the boundary to continue travelling downward through the base.

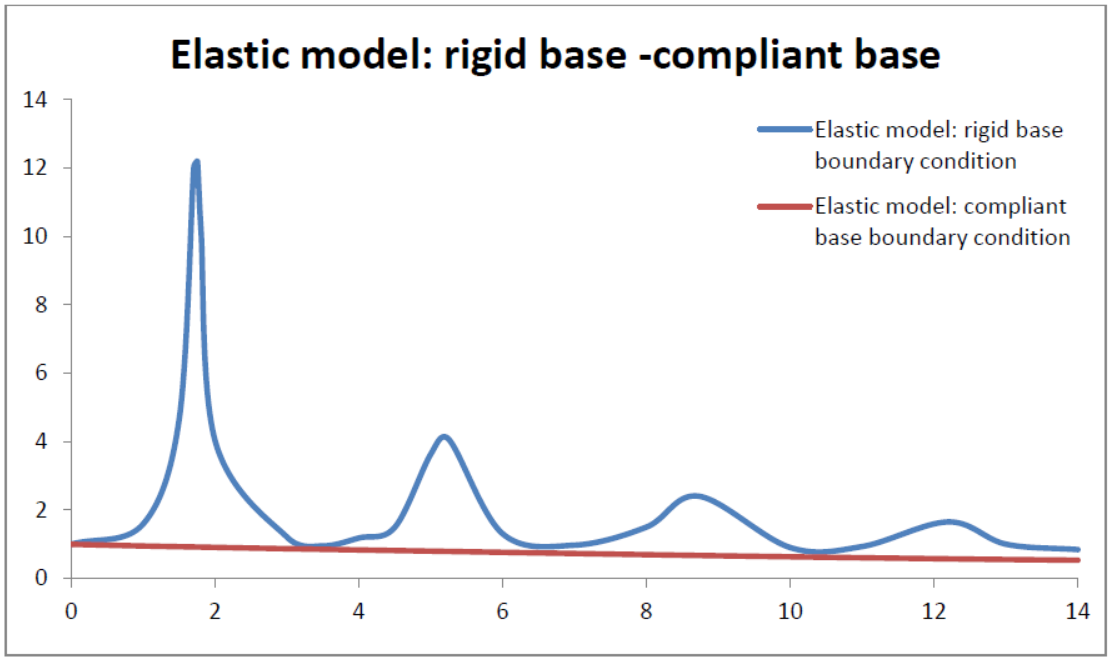

Figure 3.25: *Transfer functions* for linear elastic model (rigid base-compliant base)

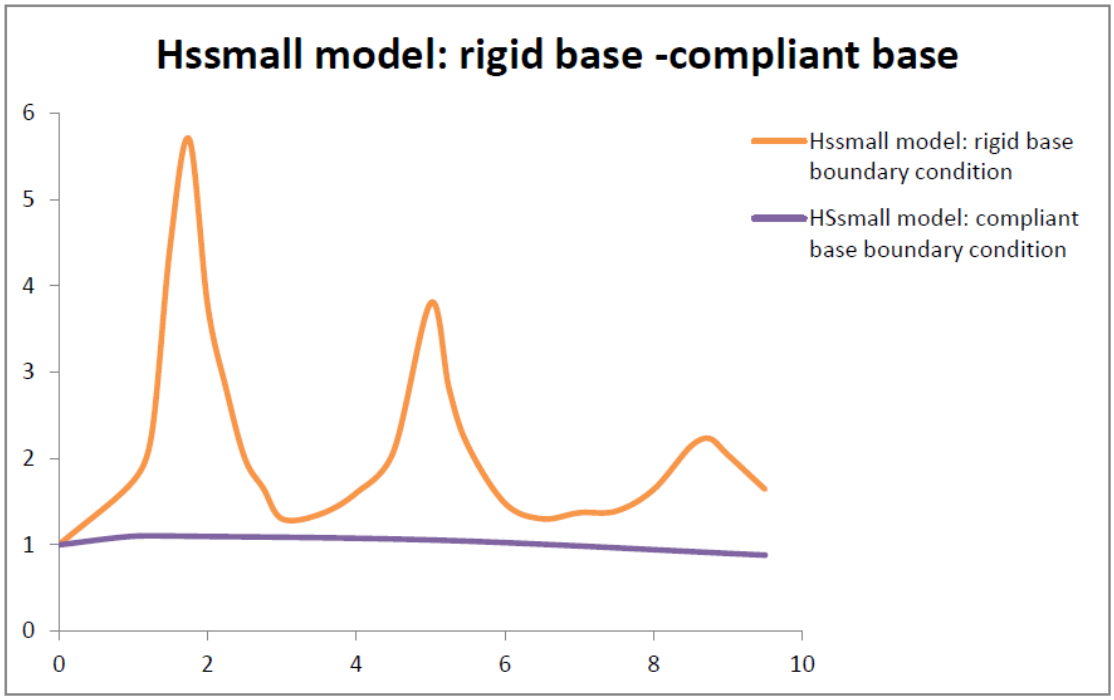

Figure 3.26: *Transfer functions* for HSsmall model (rigid base-compliant base)

In Figure 3.27 *Transfer functions* for rigid base for both linear elastic and HSsmall model are compared to show the lower amplification of the HSsmall model, because it is non-linear and the mitigation of the amplification is obvious especially in the frequencies of resonance.

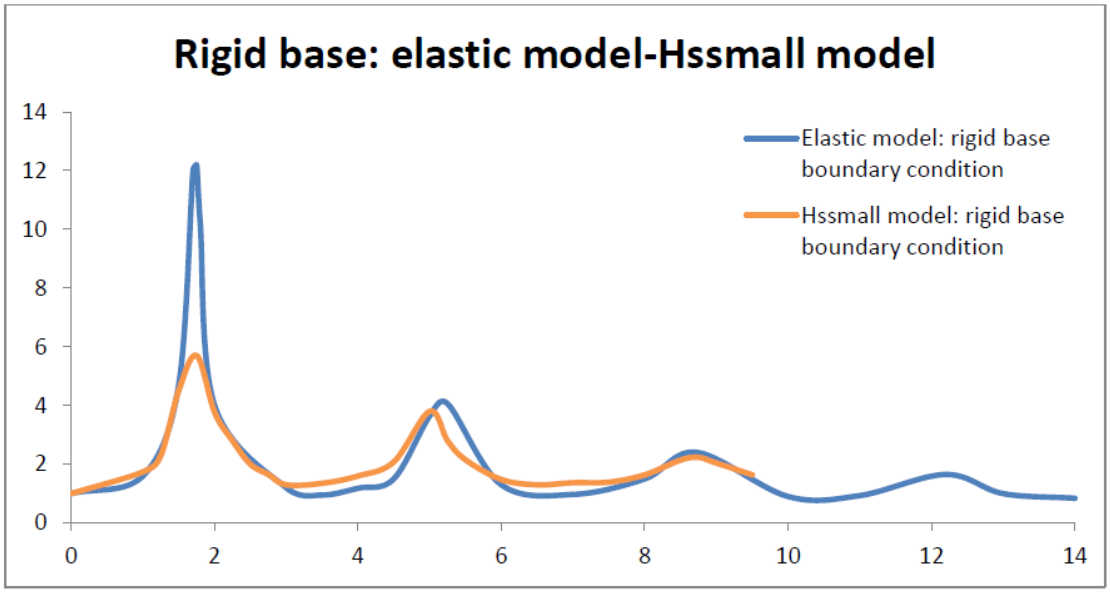

Figure 3.27: *Transfer functions* for rigid base (linear elastic-HSsmall model)

Eventually, in Figure 2.28 there is a comparison between the Amplification functions calculated by PLAXIS2D and Amplification functions calculated based on the equation:

$$\left|F_2(\omega)\right| = \frac{1}{\sqrt{\cos^2 kH + \sinh^2 \xi kH}} \tag{3.1}$$

[Kramer S. L. (1996)]

It is obvious that there is a perfect agreement between the two calculations.

Consequently, the boundary conditions of the finite element program PLAXIS2D, which are constantly improved, are of adequate precision. In this thesis, the X-axis boundary *Tied degrees of freedom* is selected as the simpler one and the Y-axis boundary *Rigid base* is selected because there is a bedrock in the geometry profile of the quay wall at Piraeus Port.

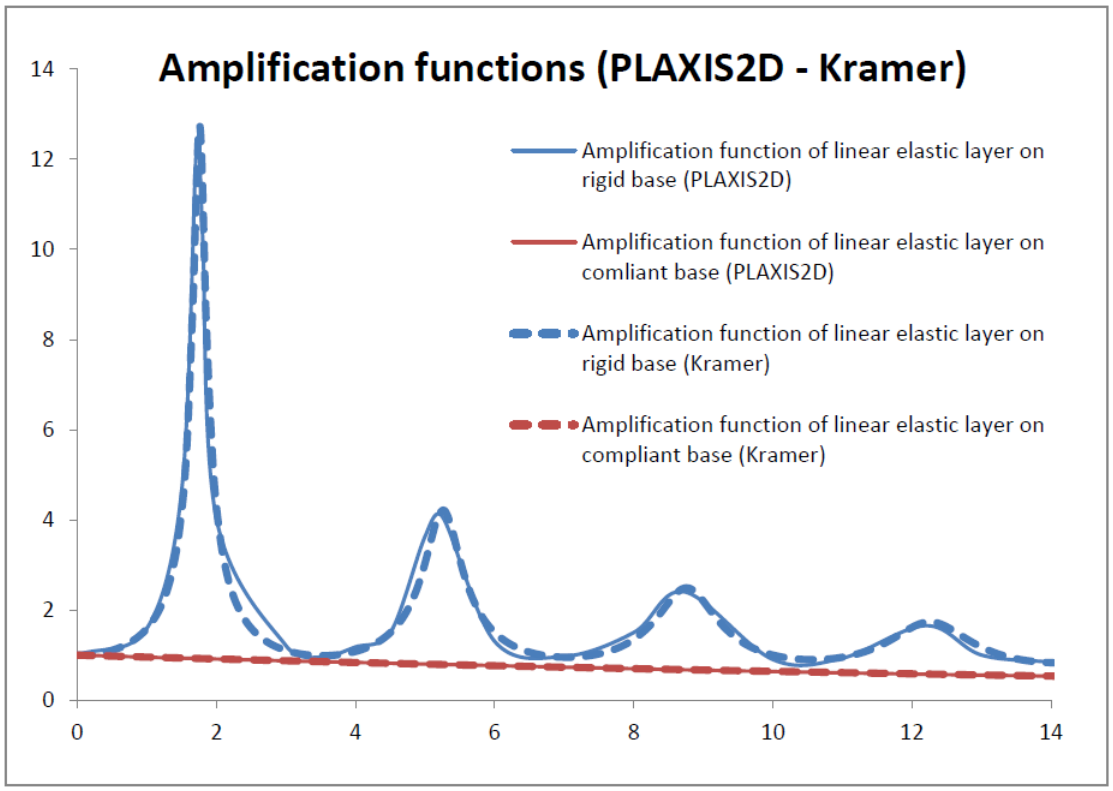

Figure 3.28: *Transfer functions* for linear elastic model (PLAXIS2D-Kramer)

3.3 Constitutive Model

2.3.1 UBCSAND

For the purpose of this thesis, there has been incorporated into PLAXIS2D an elastic plastic formulation for the constitutive model UBCSAND in which the yield loci are radial lines of constant stress ratio and the flow rule is non-associated. This represents a fully coupled effective stress dynamic analysis procedure for modeling seismic liquefaction.

The simplest realistic model for soil is the classic Mohr-Coulomb elastic-plastic model as depicted in Figure 3.29. Soils are modeled as elastic below the strength envelope and plastic on the strength envelope with plastic shear and volumetric strains increments related by the dilation angle, ψ. This model is really too simple for soils since plastic strains also occur for stress states below the strength envelope. The UBCSAND stress-strain model described herein modifies the Mohr-Coulomb model to capture the plastic strains that occur at all stages of loading. Yield loci are assumed to be radial line of constant stress ratio as shown in Figure 3.30. Unloading is assumed to be elastic. Reloading induces plastic response but with a stiffened plastic shear modulus.

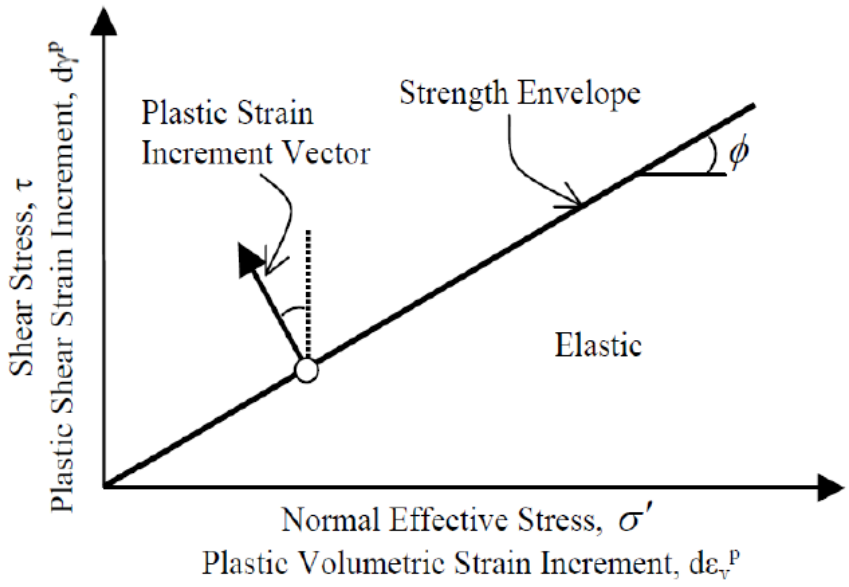

Figure 2.29: Classic Mohr-Coulomb model [P. M. Byrne & S. S. Park, M. Beaty]

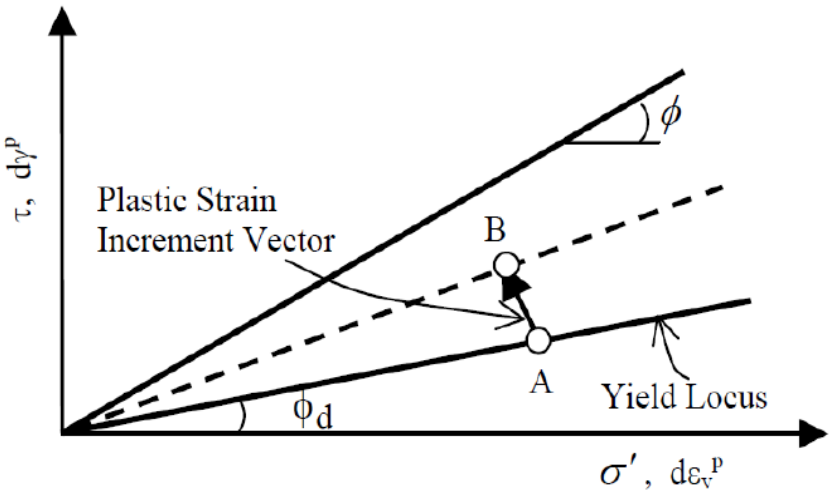

Figure 2.30: UBCSAND model [P. M. Byrne & S. S. Park, M. Beaty]

The plastic shear modulus relates the shear stress and the plastic shear strain and is assumed to be hyperbolic with stress ratio as shown in Figure 3.31. Moving the yield locus from A to B in Figure 3.30 requires a plastic shear strain increment, $\Delta\gamma^p$, as shown in Figure 3.31, and is controlled by the plastic shear modulus, G^P. The associated plastic volumetric strain increment, $d\varepsilon_v{}^P$, is obtained from the dilation angle ψ:

$$\Delta\varepsilon_v^p = \Delta\gamma^p \sin\psi \qquad (3.2)$$

The dilation angle is based on laboratory data and energy considerations and is approximated by:

$$\sin\psi = \sin\varphi_d - \sin\varphi_{cv} \qquad (3.3)$$

where φ_{cv} is the phase transformation or constant volume friction angle and φ_d describes the current yield locus. A negative value of ψ corresponds to contraction. Contraction occurs for stress states below φ_{cv} and dilation above as shown in Figure 3.32.

Elastic and plastic properties for the model are defined as follows.

[P. M. Byrne & S. S. Park, M. Beaty]

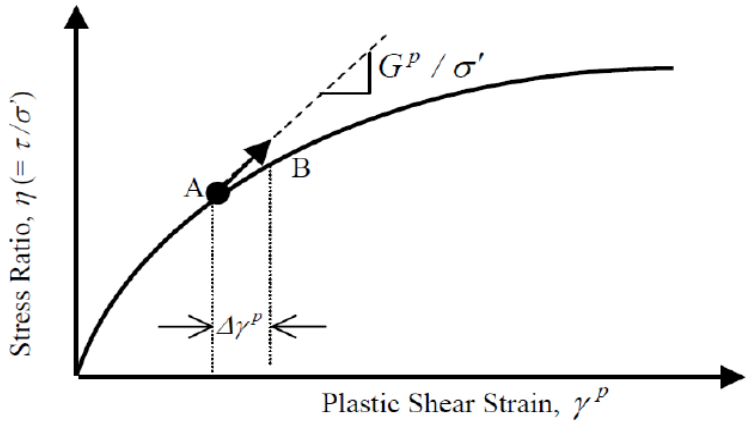

Figure 3.31: Classic Mohr-Coulomb model [P. M. Byrne & S. S. Park, M. Beaty]

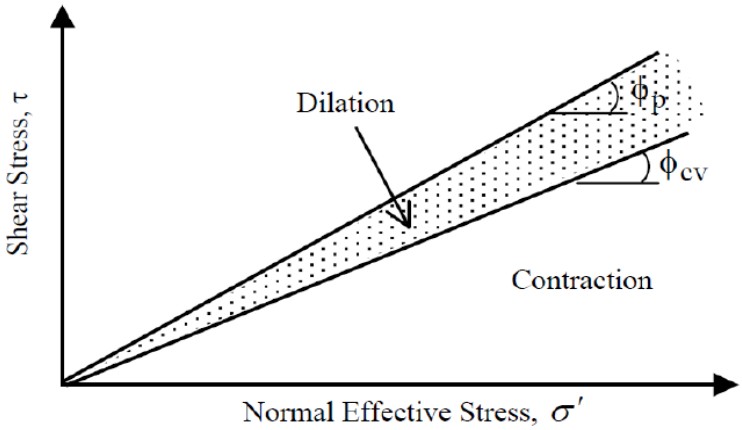

Figure 3.32: Classic Mohr-Coulomb model [P. M. Byrne & S. S. Park, M. Beaty]

Elastic Properties

The elastic bulk modulus, *B*, and shear modulus, *Ge*, are assumed to be isotropic and stress level dependent. They are described by the following relations where *kB* and *kG* are modulus numbers, *PA* is atmospheric pressure, and *σ′m* is the mean effective stress:

$$B = k_B * P_A * \left(\frac{\sigma'_m}{P_A} \right)^{0.5} \tag{3.4}$$

$$G^e = k_G * P_A * \left(\frac{\sigma'_m}{P_A} \right)^{0.5} \tag{3.5}$$

Plastic Properties

The plastic properties used by the model are the peak friction angle φ_p, the constant volume friction angle φ_{cv}, and plastic shear modulus G_P, where

$$G^P = G_i^P * \left(1 - \frac{\tau}{\tau_f} R_f\right)^{0.5} \tag{3.6}$$

$G_i^P = a * G^e$ and α depends on relative density, τ is the current shear stress, τ_f is the projected shear stress at failure, and R_f is the failure ratio used to truncate the hyperbolic relationship.

The position of the yield locus φ_d is known for each element at the start of each time step. If the stress ratio increases and plastic strain is predicted, then the yield locus for that element is pushed up by an amount $\Delta\varphi_d$ as given by Equation (3.7). Unloading of stress ratio is considered to be elastic. Upon reloading, the yield locus is set to the stress ratio corresponding to the stress reversal point.

$$\Delta\varphi_d = \left(\frac{G^P}{\sigma'_m}\right) * \Delta\gamma^P \tag{3.7}$$

The elastic and plastic parameters are highly dependent on relative density, which must be considered in any model calibration. These parameters can be selected by calibration to laboratory test data. The response of the model can also be compared to a considerable database for triggering of liquefaction under earthquake loading in the field. This database exists in terms of penetration resistance, typically from cone penetration (CPT) or standard penetration (SPT) tests. A common relationship between $(N1)_{60}$ values from the SPT and the cyclic stress ratio that triggers liquefaction for a magnitude 7.5 earthquake is given by Youd et al. (2001). Comparing laboratory data based on relative density to field data based on penetration resistance relies upon an approximate conversion, such as that proposed by Skempton (1986):

$$35 < \frac{(N_1)_{60}}{D_r^2} < 60 \tag{3.8}$$

Model parameters based on penetration resistance and field observation may be useful for field conditions where it is very difficult to retrieve and test a representative sample. However, this indirect method is not appropriate for simulation of centrifuge models. Calibrations for this case should be based on direct laboratory testing of samples that are prepared in the same manner as the centrifuge model.

3.3.2 Parameters

The PLAXIS2D liquefaction model differentiates the elastic bulk modulus *B*, and the shear modulus G^e, [PLAXIS Liquefaction Model]

The elastic behavior which occurs within the yield surface is governed by a non-linear rule. Two parameters control this non-linear behavior, the elastic bulk modulus K and the elastic shear modulus G. These two modules are stress-dependent and the relationships are given in the following equations (3.9), (3.10):

$$K = K_B^e * P_A * \left(\frac{P}{P_{ref}} \right)^{me} \tag{3.9}$$

$$G = K_G^e * P_A * \left(\frac{P}{P_{ref}} \right)^{ne} \tag{3.10}$$

where K_B^e and K_G^e are the bulk and the shear modulus respectively, at a reference stress level. The factors n_e and m_e are parameters define the rate of stress dependency of stiffness. In the literature, the reference stress level p_{ref} is commonly taken as the atmospheric pressure P_A=100 kPa.

The hyperbolic hardening rule (Beaty and Byrne, 1998) relates the increment of the sine of the mobilized friction angle to the plastic shear strain increment as follows (Puebla et al., 1997):

$$\delta\gamma^P = \left(\frac{1}{G^*} \right) * \delta * \sin\varphi_{nod} \tag{3.11}$$

$$G^* = K_G^p * \left(\frac{P'}{P_A} \right)^{np} * \left\{ 1 - \frac{\sin\varphi_{mob}}{\sin\varphi_{peak}} * R_f \right\}^2 \tag{3.12}$$

where K_G^p is the plastic shear modulus number, n_p is the plastic shear modulus exponent, φ_{mob} is the mobilized friction angle, which is defined by the stress ratio, φpeak is the peak friction angle and R_f is the failure ratio n_f/n_{ult}, ranging from 0.5 to 1.0, where n_f is the stress ratio at failure and n_{ult} is the asymptotic stress ratio from the best fit hyperbola.

The input parameters of the UBCSAND are summarized below:

- φ_{cv} is the constant volume friction angle
- φ_p is the peak friction angle
- c is the cohesion of the soil
- K_B^e is the elastic bulk modulus of the soil in a reference level of 100 kPa. It can be derived from a drained triaxial test with a confining pressure of 100 kPa.
- K_G^e is the elastic shear modulus of the soil in a reference level of 100 kPa. It can be related with the K_B^e using the Poison ratio as shown in Equation:

$$\frac{K_B^e}{K_G^p} = \frac{2(1+\nu')}{3(1-2\nu')} \qquad (3.13)$$

- K_G^p is the plastic shear modulus and has to be extracted after curve fit
- m_e is the elastic bulk modulus index and has a default value of 0.5
- n_e is the elastic shear modulus index and has a default value of 0.5
- n_p is the plastic shear modulus index and has a default value of 0.5
- R_f is the failure ratio n_f/n_{ult}
- P_A is the atmospheric pressure
- fac_{hard} is the densification factor. It is a multiplier that controls the scaling of the plastic shear modulus during secondary loading. Above 1 the K_G^p becomes higher and the behavior stiffer and bellow 1 the K_G^p becomes lower and the behavior softer
- $N1_{60}$ is the corrected SPT value of the soil.
- fac_{post} is a fitting parameter to adjust post liquefaction behavior

3.3.3 Undrained behavior

The undrained behavior of the soil is treated implicitly by the UBCSAND constitutive model. Therefore, the increment of the pore water pressure is computed at each step of the analysis. Considering a saturated soil specimen, the increments in total stress during loading is given by the following equation:

$$dp = K_u * d\varepsilon_v \tag{3.14}$$

where K_u is the bulk modulus of the undrained soil and $d\varepsilon_v$ the volumetric strain of the soil as a whole

The effective stress increment can be computed as follows:

$$dp' = K' * d\varepsilon_v \tag{3.15}$$

where K' is the bulk modulus of the soil skeleton and $d\varepsilon_v$ its volumetric strain.

The increments of the pore water pressure are computed with the following equation:

$$dp_w = \frac{K_w}{n} * d\varepsilon_v \tag{3.16}$$

where K_w is the bulk modulus of the water, n is the soil porosity and $d\varepsilon_v$ is the volumetric strain of the fluid.

The relationship between the total stresses, the effective stresses and the pore pressure is assumed according to Terzaghi's theory (Equation 3.17). Moreover, the volumetric compatibility under undrained conditions requires that the equivalent fluid volumetric strain must be equal to the volumetric strain of the soil skeleton. Equation 16 is finally derived.

$$dp = dp' + dp_w \tag{3.17}$$

$$\frac{K_w}{n} = (K_u - K') \tag{3.18}$$

Once K_w is determined, then the excess pore pressures can be computed in each increment using Equation 3.16. The Poisson's ratio for undrained condition is set

as ν = 0.495 implicitly by the model. This value is close to the upper limit (of 0.5) as water is almost incompressible. Using a value of 0.5 is to be avoided as this is known to cause numerical instabilities. Based on this Poisson's ratio the bulk modulus of the undrained soil is computed as follows:

$$K_u = \frac{2G^e(1+\nu_u)}{3(1-2\nu_u)} \tag{3.19}$$

where G^e is the elastic shear modulus.

The drained bulk modulus of the soil skeleton K' is computed in the same way using the drained Poisson's ratio which is based on the stress dependent stress module (Equation 3.20).

$$K_u = \frac{3K^e - 2G^e}{6K^e + 2G^e} \tag{3.20}$$

3.3.4 Rayleigh

Material damping in dynamic calculations is caused by the viscous properties of soil, friction and the development of irreversible strains. All plasticity models in PLAXIS2D can generate irreversible (plastic) strains, and may thus cause material damping. However, the damping is generally not enough to model the damping characteristics of real soils, especially in cases of low deformations. For example, most soil models show pure elastic behavior upon unloading and reloading which does not lead to damping at all. When using these models, the amount of damping that is obtained depends on the amplitude of the strain cycles and so, these models do not show material damping. Hence, additional damping is needed to model realistic damping characteristics of soils in dynamic calculations. This can be done by means of Rayleigh damping.

The use of additional damping, i.e. Rayleigh α and β, can also lead to numerical convergence. Rayleigh damping is a numerical feature in which a damping matrix C is composed by adding a portion of the mass matrix M and a portion of the stiffness matrix K:

$$C = \alpha M + \beta K$$

The parameters α and β are the Rayleigh coefficients and can be specified in the corresponding cells in the *Parameters* tabsheet of the *Soil* window (Figure 3.33).

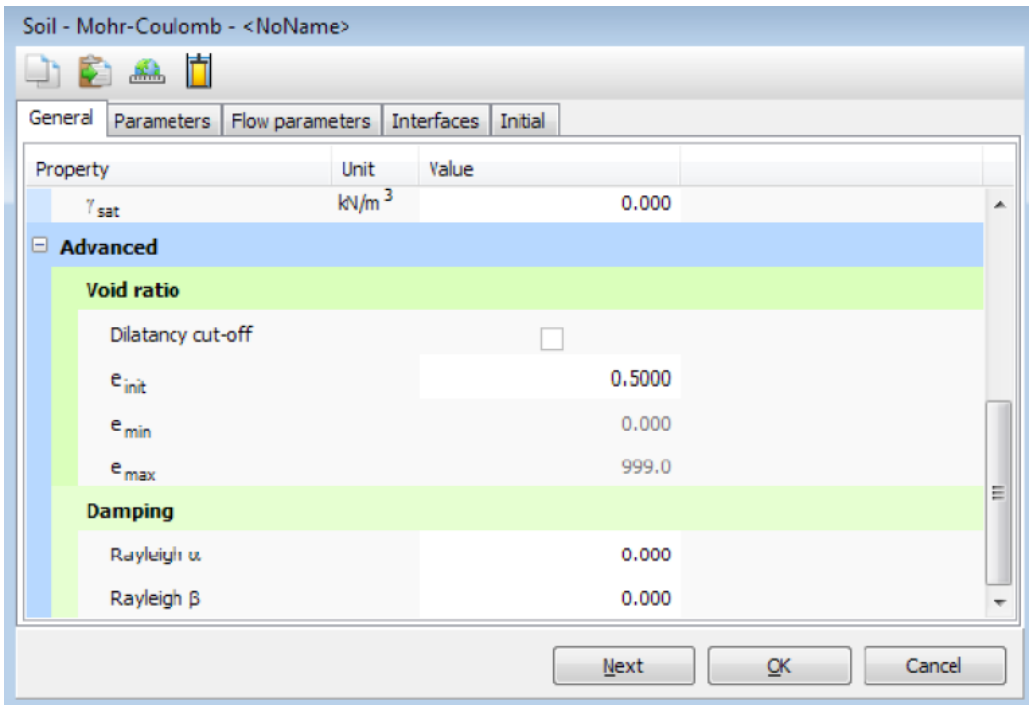

Figure 3.33: Damping parameters in the *General* tabsheet

2.4 Interfaces

Interfaces are joint elements to be added to plates or geogrids to allow for a proper modeling of soil-structure interaction. Interfaces may be used to simulate, for example, the thin zone of intensely shearing material at the contact between a plate and the surrounding soil. Interfaces can be created next to plate or geogrid elements or between two soil volumes.

2.4.1 Interfaces between the blocks of the quay wall

The parameters selected for the interface between the blocks of the multi-block quay wall are shown in the Figure 3.34.

Analyses that have been done within this thesis by PLAXIS2D indicate that the Effective Young's modulus should be larger than 100 *10^3 kN/m2.

Figure 3.34: Interfaces between the blocks of the quay wall

2.4.2 Interfaces at the back and the base of the quay wall

The parameters selected for the interface at the back and the base of the quay wall are shown in the Figure 3.35 and 3.36.

Analyses that have been done within this thesis by PLAXIS2D indicate that the Effective Young's modulus should be larger than 50 *10^3 kN/m2.

Material set		
Identification number		7
Identification		g.interface.wall-soil
Material model		Mohr-Coulomb
Drainage type		Drained
Colour		RGB 11, 23, 91
Stiffness		
E	kN/m²	80.00E3
ν (nu)		0.2500
Alternatives		
G	kN/m²	32.00E3
E_{oed}	kN/m²	96.00E3
Strength		
c_{ref}	kN/m²	1.000
φ (phi)	°	15.00
ψ (psi)	°	0.000
Velocities		
V_s	m/s	112.1
V_p	m/s	194.1

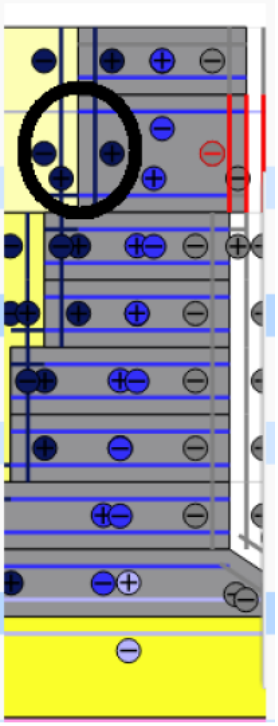

Figure 2.35: Interfaces at the back of the quay wall

Material set		
Identification number		10
Identification		g.interface.wall-soil(base)
Material model		Mohr-Coulomb
Drainage type		Drained
Colour		RGB 183, 180, 254
Stiffness		
E	kN/m²	80.00E3
ν (nu)		0.2500
Alternatives		
G	kN/m²	32.00E3
E_{oed}	kN/m²	96.00E3
Strength		
c_{ref}	kN/m²	1.000
φ (phi)	°	30.00
ψ (psi)	°	0.000
Velocities		
V_s	m/s	112.1
V_p	m/s	194.1

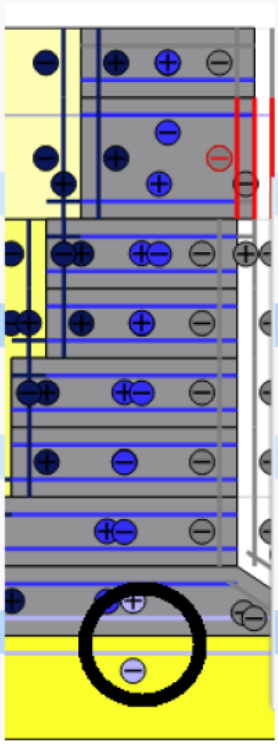

Figure 2.36: Interfaces at the base of the quay wall

2.4.3 Interfaces on the frontage of the quay wall

In the thesis model in the first sight, it is obvious that there is not any adjacent soil in the frontage of the quay wall, thus there is no need for an interface. However, after analyses that were proceeded within this thesis by PLAXIS2D, it was observed that the lack of interface in the frontage of the quay wall did not let the blocks to move the one along the other and the quay wall to move along the base soil. This becomes clear by observing the relative displacement of the blocks in the case without interface (Figures 3.38, 3.39) and the case with interface on the frontage (Figures 3.41, 3.42).

In Figures 3.40 and 3.43 it is also observed that the *Relative shear stress τrel* in the frontage is eliminated in the case without interface, while in the case with interface the *Relative shear stress τrel* in the frontage is finite. This leads to the fact that interface should be used in the frontage of the quay wall.

Nevertheless, since there is not any adjacent soil, the interfaces can be deactivated when modeling soil-structure interaction is not desired (Figure 3.37). Nodes generated for interfaces in mesh generation process are still there. They have stiff elastic behavior and they are fully permeable.

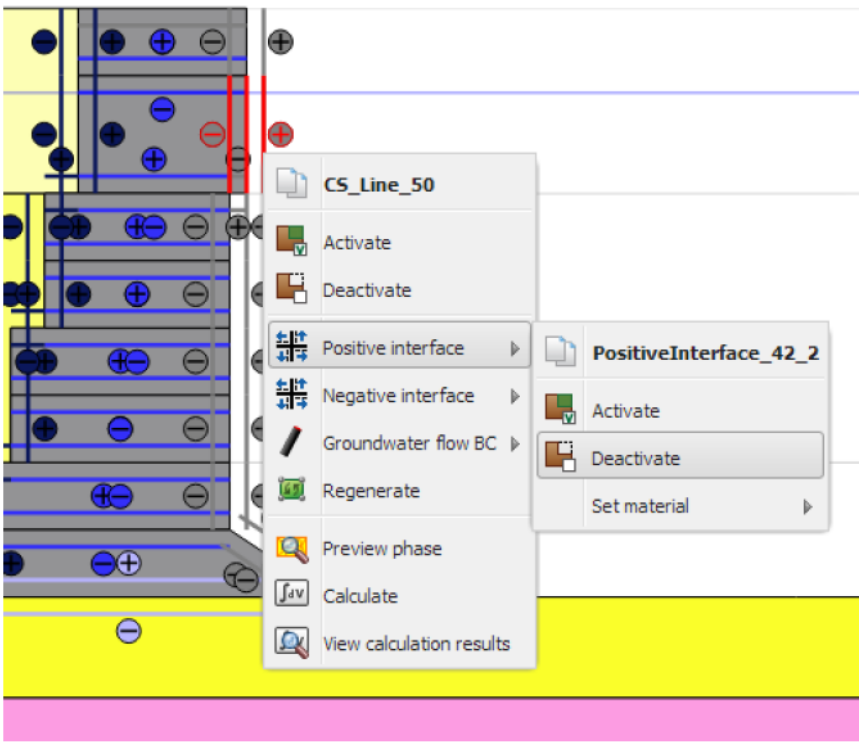

Figure 3.37: Interface in the frontage of the quay wall

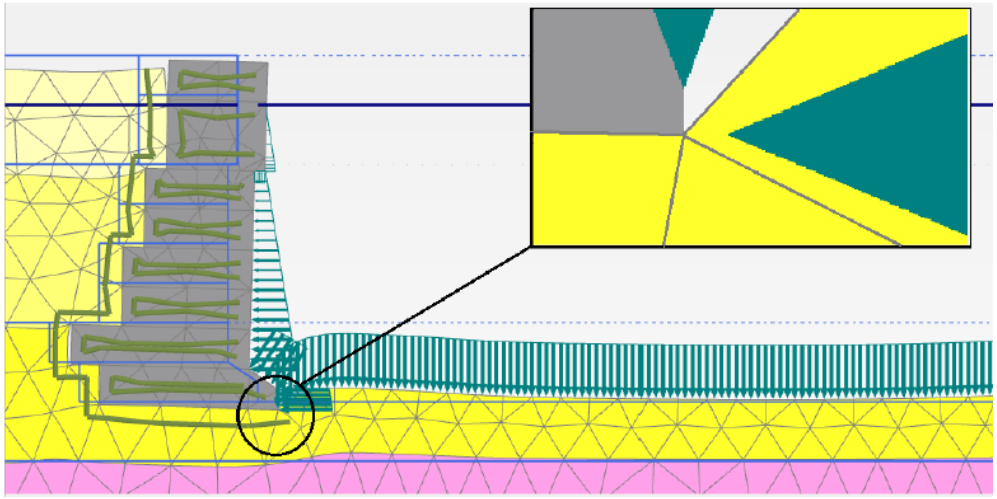

Figure 3.38: Relative displacement of quay wall blocks (without interface)

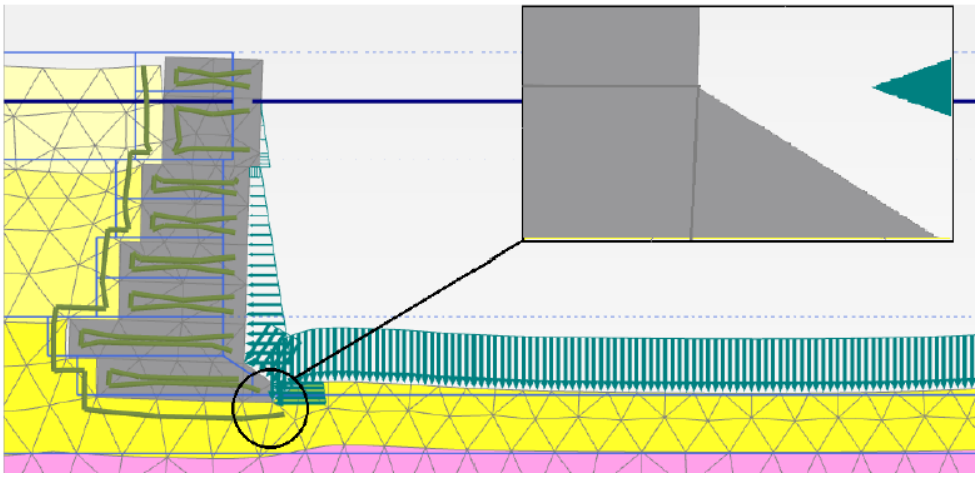

Figure 3.39: Relative displacement of quay wall blocks (without interface)

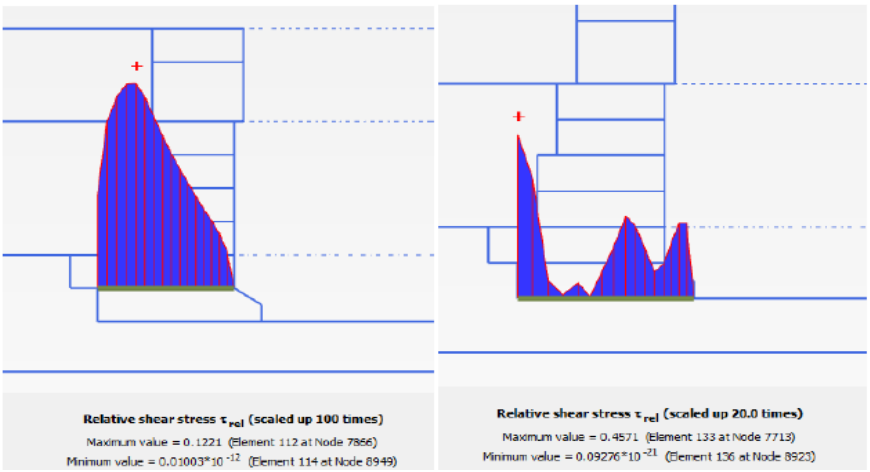

Figure 3.40: *Relative shear stress τrel* in the frontage of the quay wall (without interface)

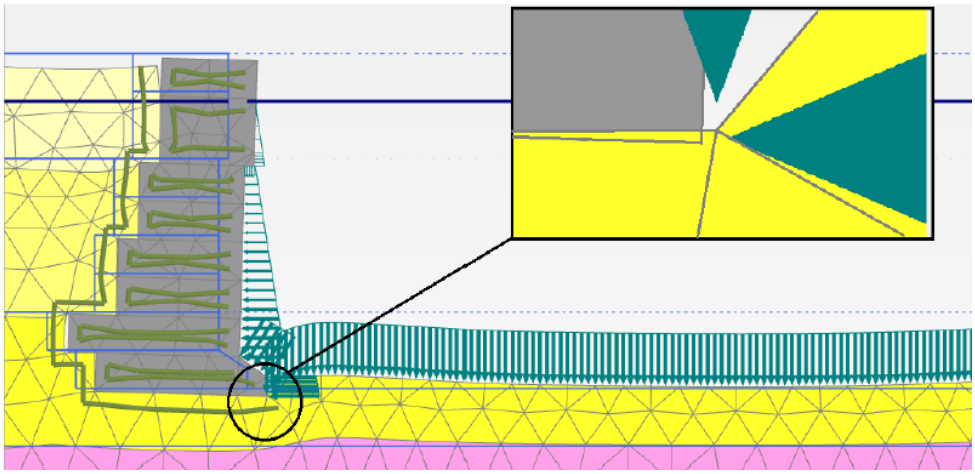

Figure 3.41: Relative displacement of quay wall blocks (with interface)

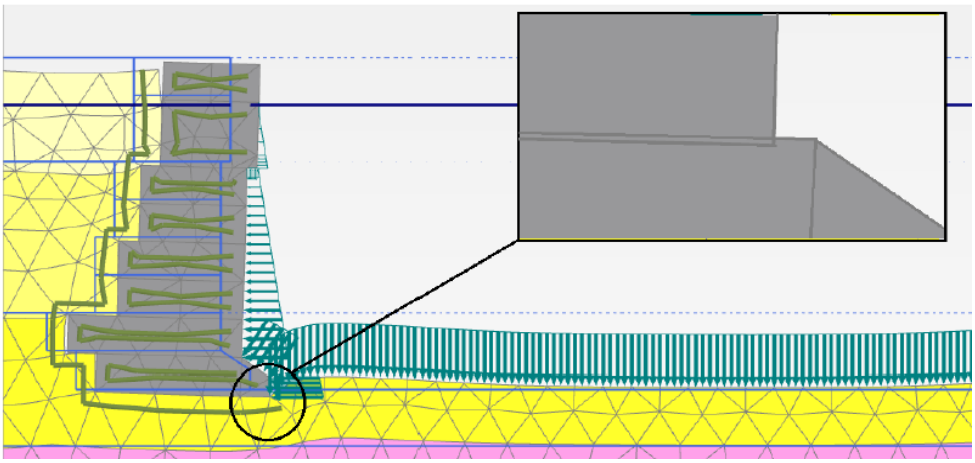

Figure 3.42: Relative displacement of quay wall blocks (with interface)

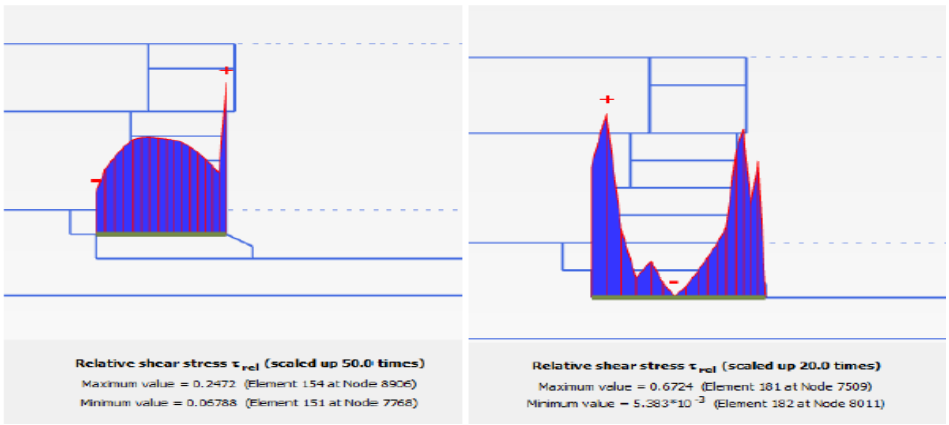

Figure 3.43: *Relative shear stress* τ_{rel} in the frontage of the quay wall (with interface)

Chapter 4

Quay wall at Piraeus Port

4.1 Geometry – Profile

A typical section of pier II comprising the geometry of the block-type gravity quay wall and the idealized soil profile is shown in Figures 4.1, 4.2. The distances of the boundaries from the quay wall are also shown in Figure 4.1.

The layers that constitute the soil profile are the following:

- 0m – 20,5m: sandy gravel, φ=35°, Dr=80%
- 20,5m – 25,5m: silty sand, φ=30°, Dr=60%
- 25,5m – 32m: gravelly sand, φ=35°, Dr=80%
- 32m – 37,5m: soft marl, Su=120 kPa

The examined soil profile does not indicate significant liquefaction potential, apart from the silty sand layer of medium density situated 3m below the base of the quay wall. Consequently, in order to examine the interaction of the quay wall – soil system and the potential liquefaction of the soil included, three types of models were dynamically analyzed, changing only the backfill soil (0m – 20,5m) in each type:

- Model 1: with a significant liquefaction potential, backfill soil with Dr=40%
- Model 2: with a mediocre liquefaction potential, backfill soil with Dr=65%
- Model 3: with a minor liquefaction potential, backfill soil with Dr=80%

The aforementioned Model 1, Model 2 and Model 3 are shown in the Figures 4.3, 4.4 and 4.5, respectively.

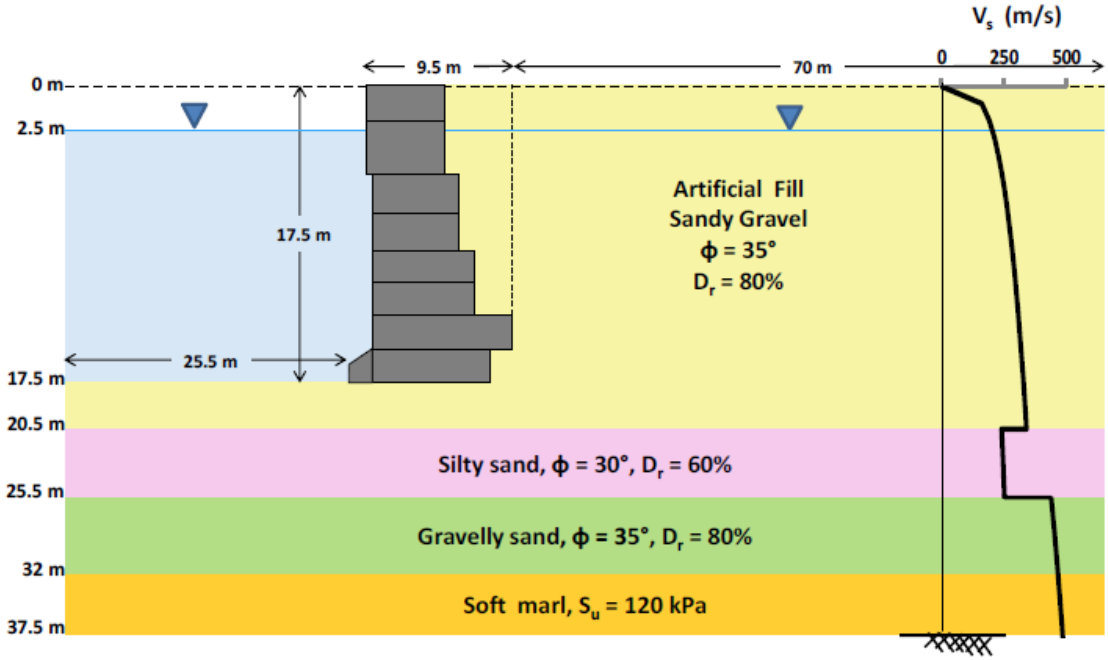

Figure 4.1: Idealized soil profile of pier II of Piraeus Port **[**Tasiopoulou P., Gerolymos N., Gazetas]

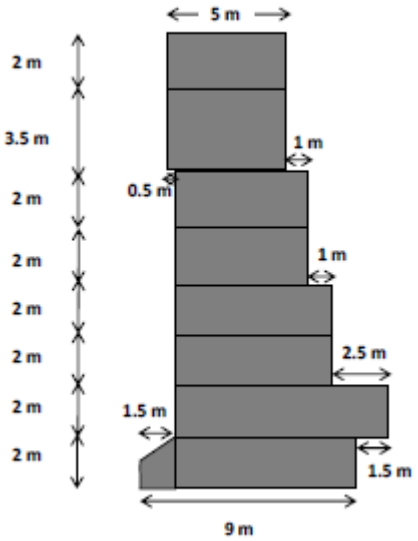

Figure 4.2: Geometry of the block-type gravity quay wall **[**Tasiopoulou P., Gerolymos N., Gazetas]

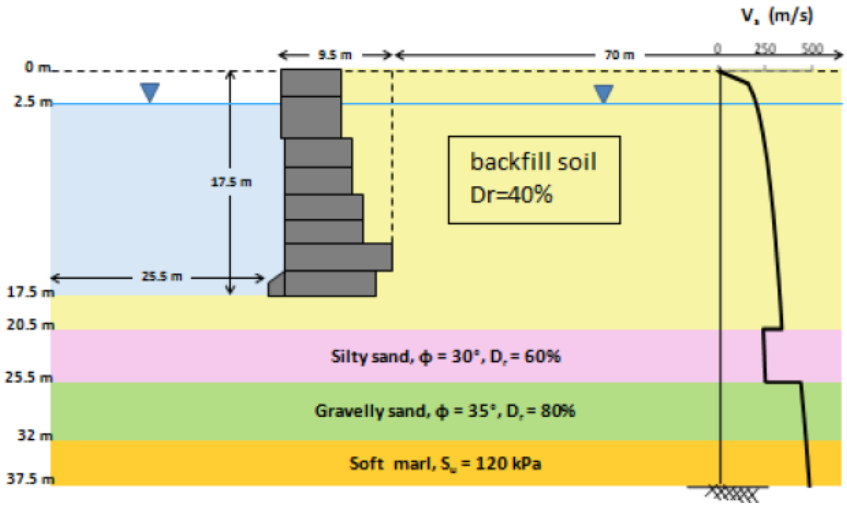

Figure 4.3: Idealized soil profile of pier II of Piraeus Port (Model 1)

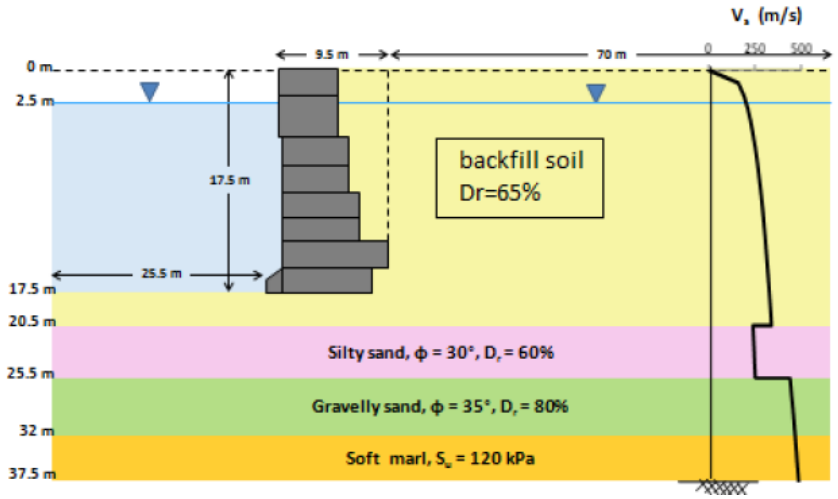

Figure 4.4: Idealized soil profile of pier II of Piraeus Port (Model 2)

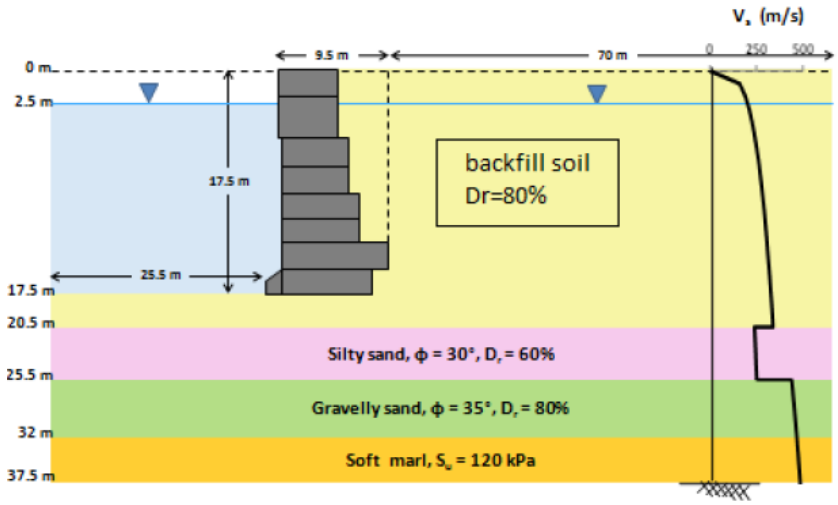

Figure 4.5: Idealized soil profile of pier II of Piraeus Port (Model 3)

4.2 Input values

4.2.1 Material properties

The first layer of the soil profile has been divided into tree sub-layers, in order to have a better discretisation of the features of the first layer, i.e. the backfill soil. Therefore, the ultimate stratigraphy is composed of six layers:

- sandy gravel 1
- sandy gravel 2
- sandy gravel 3
- silty sand
- gravelly sand
- soft marl

The sandy gravel (1,2,3), the silty sand and the gravelly sand *Material model* has been selected to be User defined, i.e. UBCSAND model, and their *Drainage type* has been *Undrained(A).* The soft marl *Material model* is *HSsmall* and *Drainage type Undrained(B*).

The concrete of the blocks of the quay wall has as *Material model* the Linear elastic and as *Drainage type* Non-porous.

The interfaces have as *Material model* the Mohr-Coulomb and as *Drainage type* Drained.

4.2.2 Parameters

The parameters that have been selected for the layers of the soil profile for each backfill soil type, i.e. Dr=40%, Dr=65% and Dr=80%, are arrayed in the Figures 4.6 to 4.18

Only the backfill soil layers, i.e. sandy gravel (1,2,3), should alternate their parameters depending on the backfill soil type, i.e. Dr=40%, Dr=65% and Dr=80%.

Silty sand, gravelly sand and soft marl remain the same at all backfill soil types.

Of course, concrete and interfaces parameters remain as they are.

Dr=40%

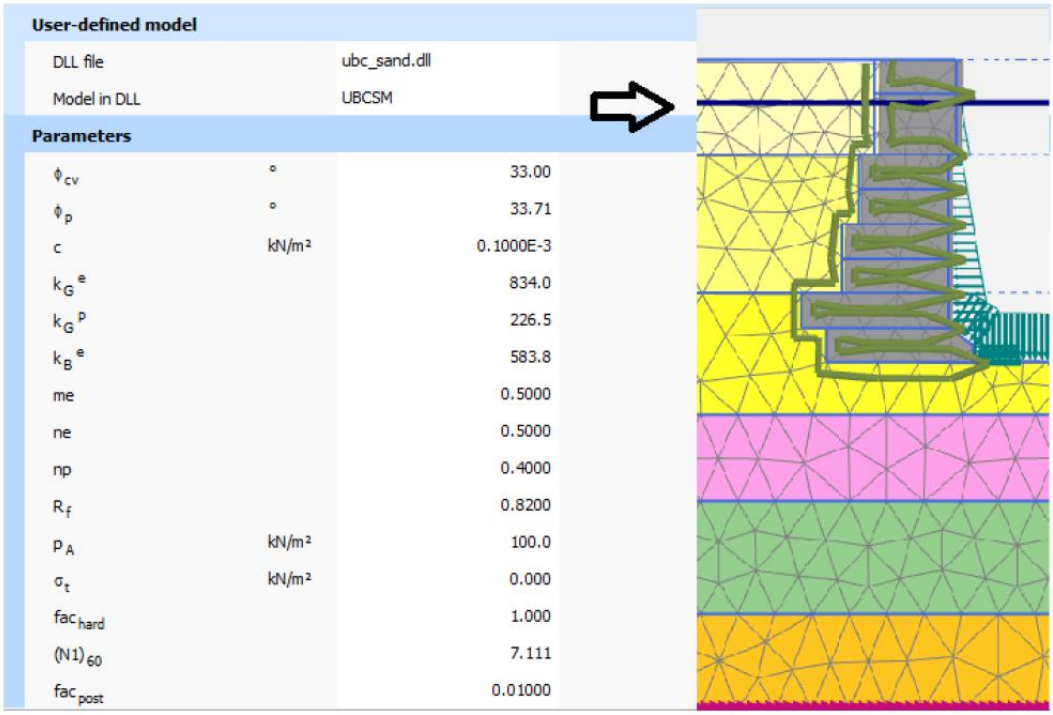

Figure 4.6: Parameters of sandy gravel 1 (Dr=40%)

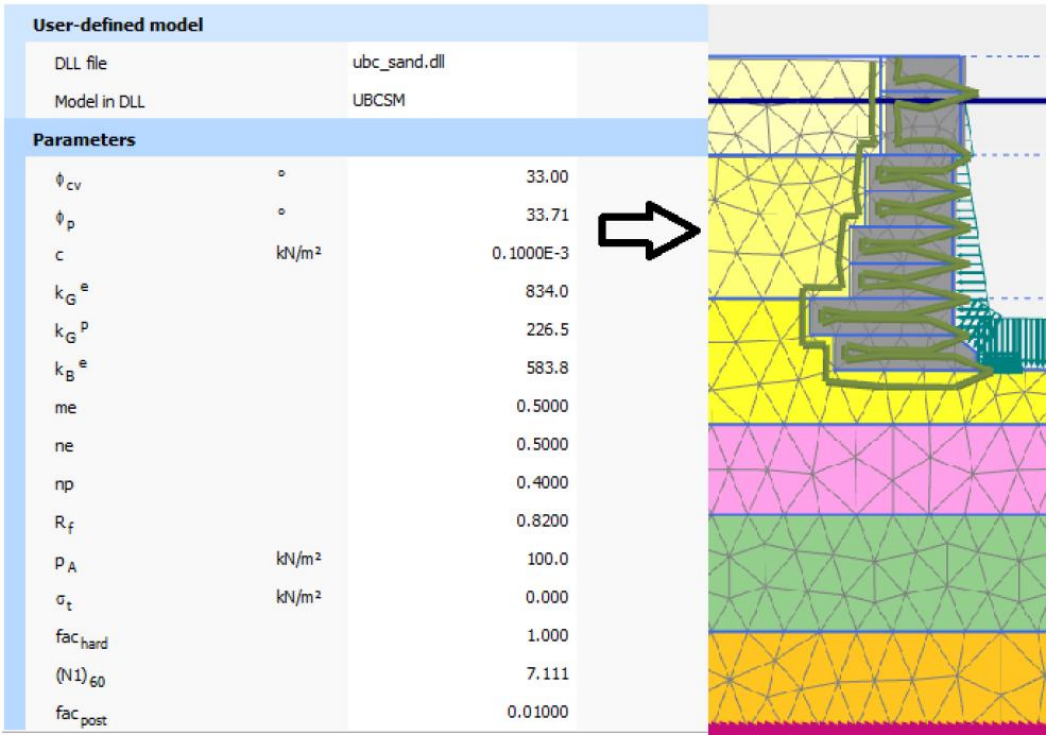

Figure 4.7: Parameters of sandy gravel 2 (Dr=40%)

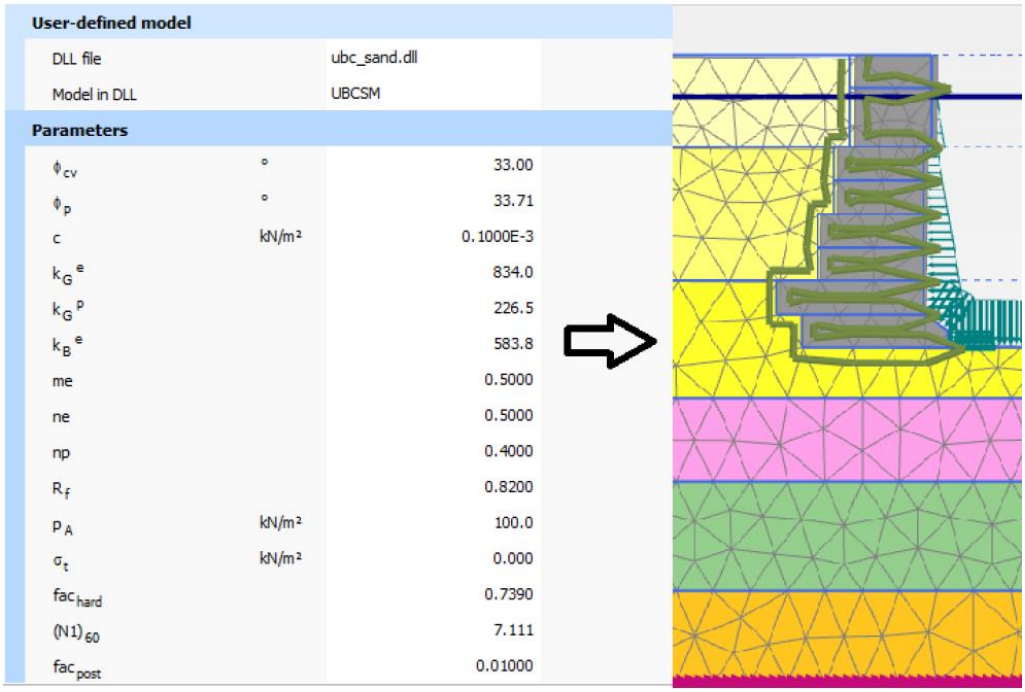

User-defined model		
DLL file		ubc_sand.dll
Model in DLL		UBCSM
Parameters		
ϕ_{cv}	°	33.00
ϕ_p	°	33.71
c	kN/m²	0.1000E-3
k_G^e		834.0
k_G^p		226.5
k_B^e		583.8
me		0.5000
ne		0.5000
np		0.4000
R_f		0.8200
p_A	kN/m²	100.0
σ_t	kN/m²	0.000
fac_{hard}		0.7390
$(N1)_{60}$		7.111
fac_{post}		0.01000

Figure 4.8: Parameters of sandy gravel 3 (Dr=40%)

Dr=65%

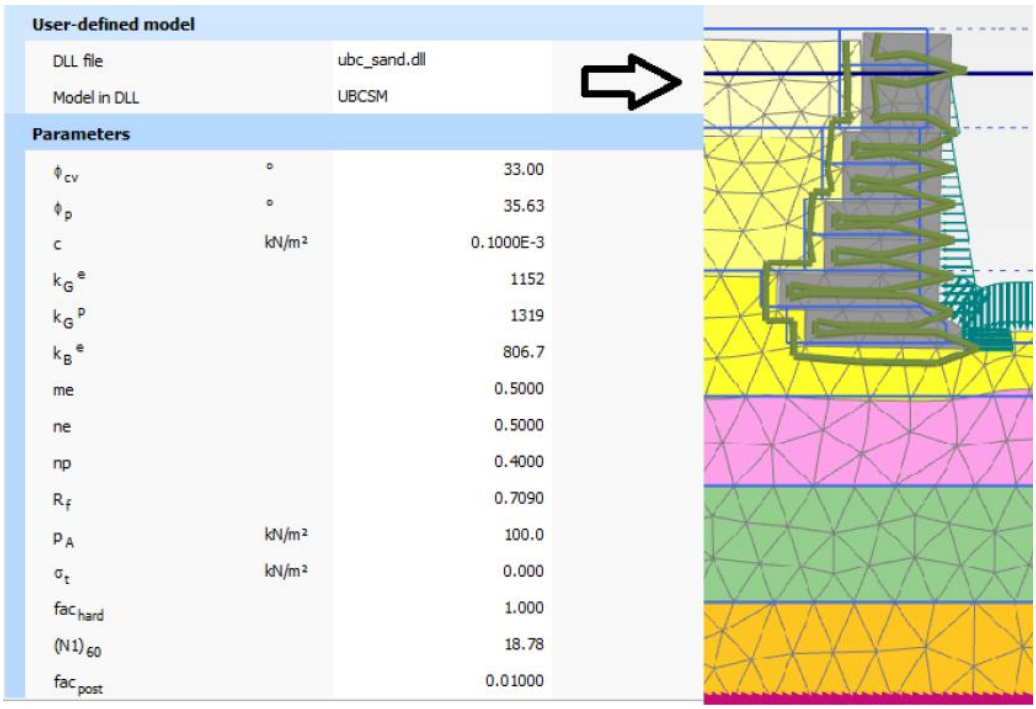

User-defined model		
DLL file		ubc_sand.dll
Model in DLL		UBCSM
Parameters		
ϕ_{cv}	°	33.00
ϕ_p	°	35.63
c	kN/m²	0.1000E-3
k_G^e		1152
k_G^p		1319
k_B^e		806.7
me		0.5000
ne		0.5000
np		0.4000
R_f		0.7090
p_A	kN/m²	100.0
σ_t	kN/m²	0.000
fac_{hard}		1.000
$(N1)_{60}$		18.78
fac_{post}		0.01000

Figure 4.9: Parameters of sandy gravel 1 (Dr=65%)

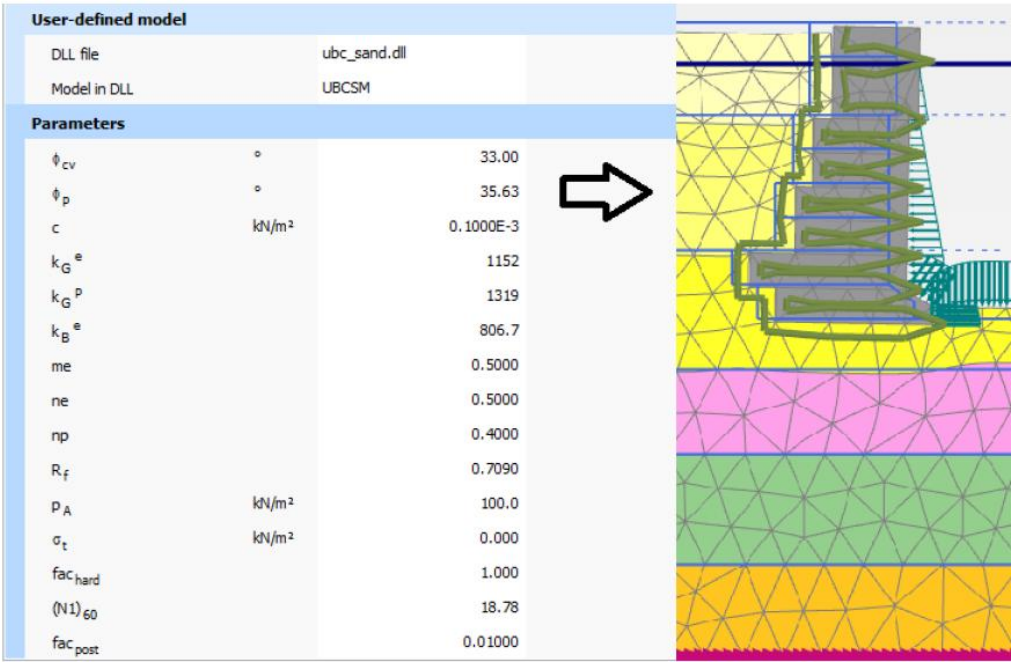

User-defined model		
DLL file		ubc_sand.dll
Model in DLL		UBCSM
Parameters		
ϕ_{cv}	°	33.00
ϕ_p	°	35.63
c	kN/m²	0.1000E-3
k_G^e		1152
k_G^p		1319
k_B^e		806.7
me		0.5000
ne		0.5000
np		0.4000
R_f		0.7090
p_A	kN/m²	100.0
σ_t	kN/m²	0.000
fac_{hard}		1.000
$(N1)_{60}$		18.78
fac_{post}		0.01000

Figure 4.10: Parameters of sandy gravel 2 (Dr=65%)

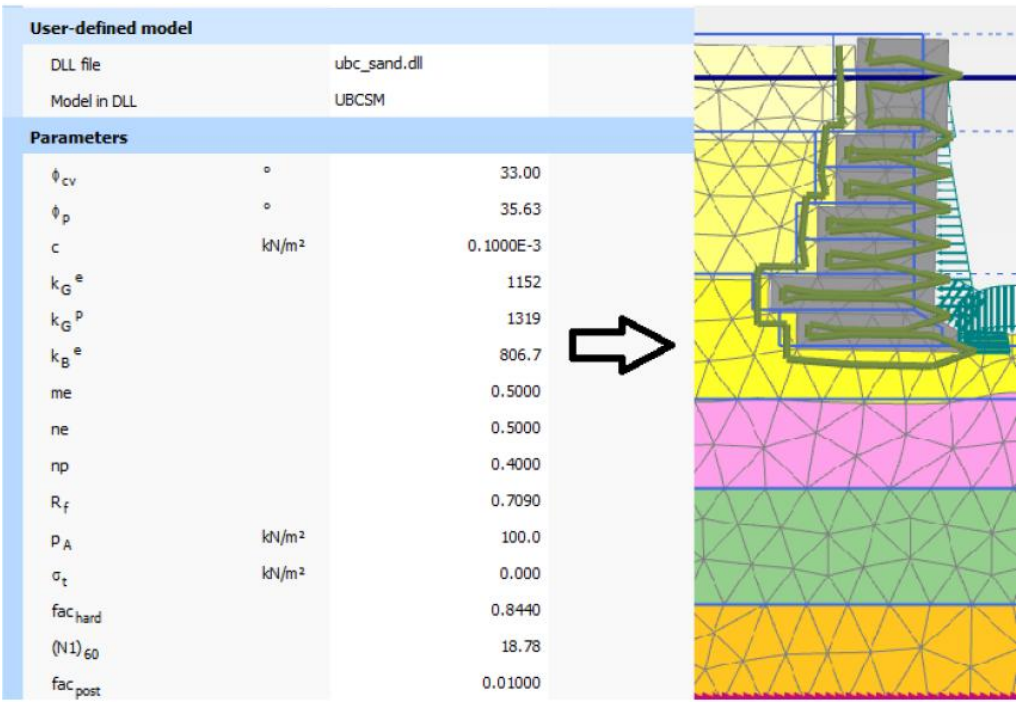

User-defined model		
DLL file		ubc_sand.dll
Model in DLL		UBCSM
Parameters		
ϕ_{cv}	°	33.00
ϕ_p	°	35.63
c	kN/m²	0.1000E-3
k_G^e		1152
k_G^p		1319
k_B^e		806.7
me		0.5000
ne		0.5000
np		0.4000
R_f		0.7090
p_A	kN/m²	100.0
σ_t	kN/m²	0.000
fac_{hard}		0.8440
$(N1)_{60}$		18.78
fac_{post}		0.01000

Figure 4.11: Parameters of sandy gravel 3 (Dr=65%)

Dr=80%

User-defined model		
DLL file		ubc_sand.dll
Model in DLL		UBCSM
Parameters		
ϕ_{cv}	°	33.00
ϕ_p	°	38.53
c	kN/m²	0.1000E-3
k_G^e		1323
k_G^p		3312
k_B^e		926.3
me		0.5000
ne		0.5000
np		0.4000
R_f		0.6660
p_A	kN/m²	100.0
σ_t	kN/m²	0.000
fac_{hard}		1.000
$(N1)_{60}$		28.44
fac_{post}		0.01000

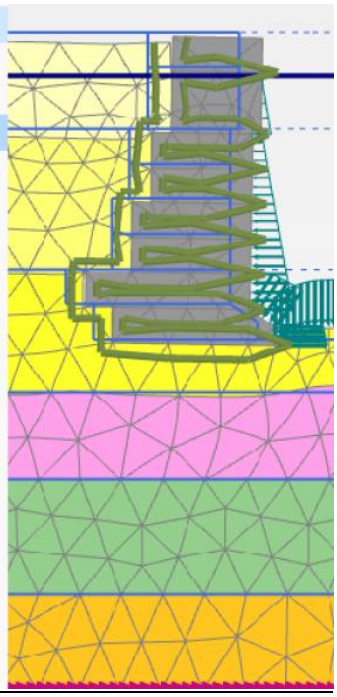

Figure 4.12: Parameters of sandy gravel 1 (Dr=80%)

User-defined model		
DLL file		ubc_sand.dll
Model in DLL		UBCSM
Parameters		
ϕ_{cv}	°	33.00
ϕ_p	°	38.53
c	kN/m²	0.1000E-3
k_G^e		1323
k_G^p		3312
k_B^e		926.3
me		0.5000
ne		0.5000
np		0.4000
R_f		0.6660
p_A	kN/m²	100.0
σ_t	kN/m²	0.000
fac_{hard}		0.7830
$(N1)_{60}$		28.44
fac_{post}		0.01000

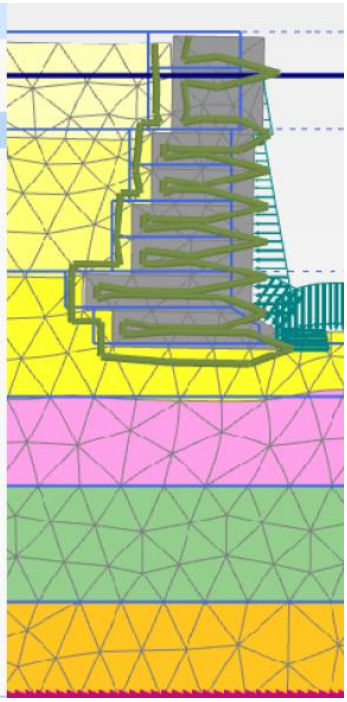

Figure 4.13: Parameters of sandy gravel 2 (Dr=80%)

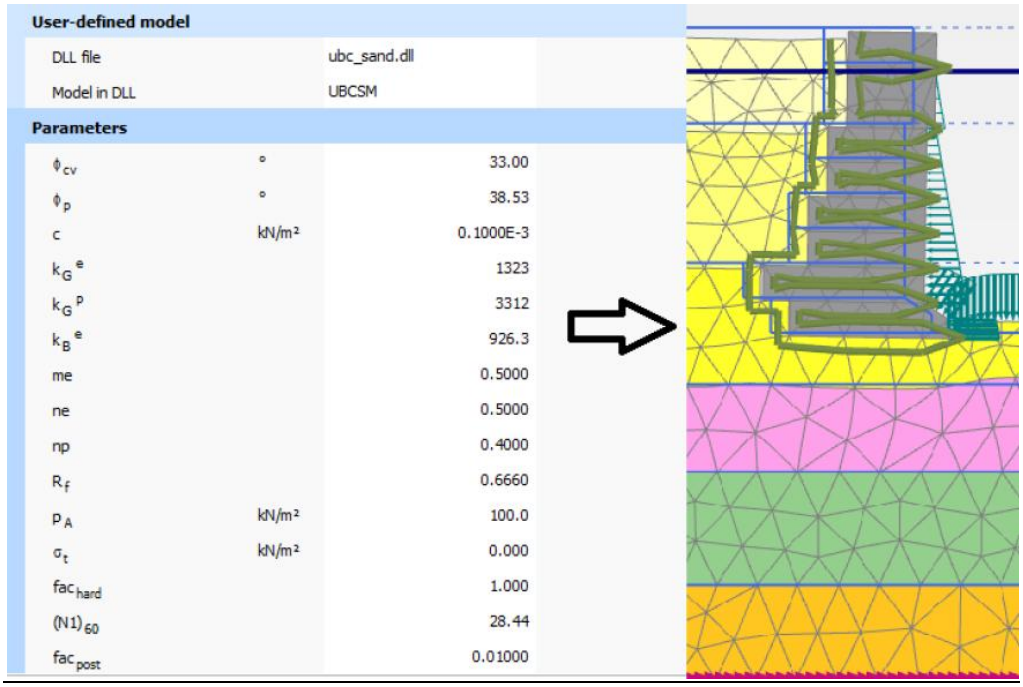

User-defined model		
DLL file		ubc_sand.dll
Model in DLL		UBCSM
Parameters		
ϕ_{cv}	°	33.00
ϕ_p	°	38.53
c	kN/m²	0.1000E-3
k_G^e		1323
k_G^p		3312
k_B^e		926.3
me		0.5000
ne		0.5000
np		0.4000
R_f		0.6660
p_A	kN/m²	100.0
σ_t	kN/m²	0.000
fac_{hard}		1.000
$(N1)_{60}$		28.44
fac_{post}		0.01000

Figure 4.14: Parameters of sandy gravel 3 (Dr=80%)

Dr=40%, 65% & 80%

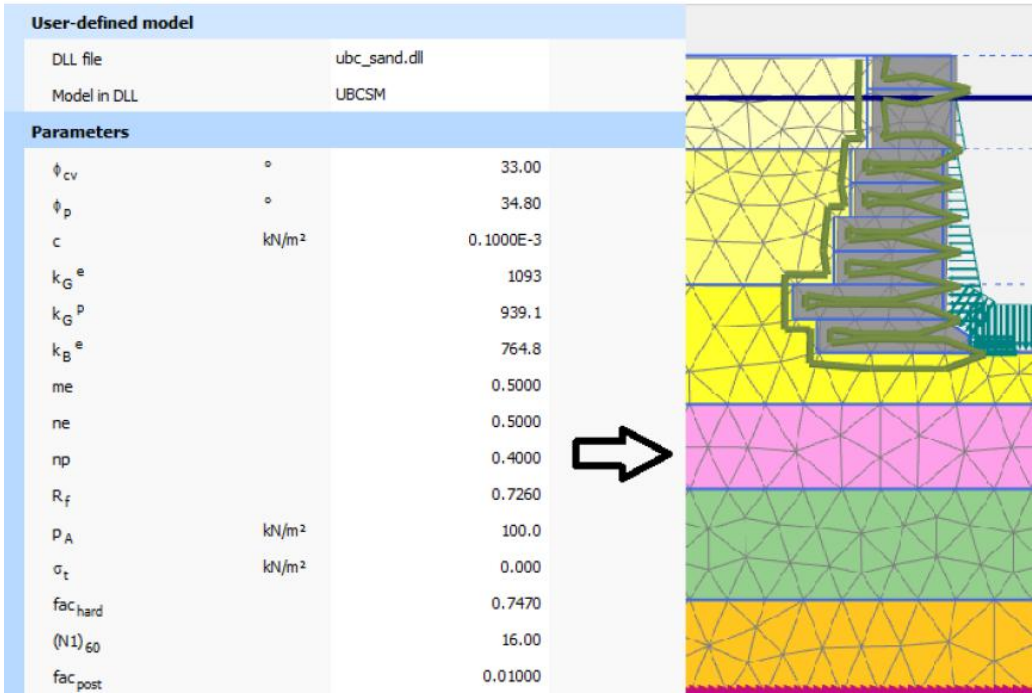

Figure 4.15: Parameters of sandy silty sand (Dr=40%, Dr=65% and Dr=80%)

Figure 3.16: Parameters of gravelly sand (Dr=40%, Dr=65% and Dr=80%)

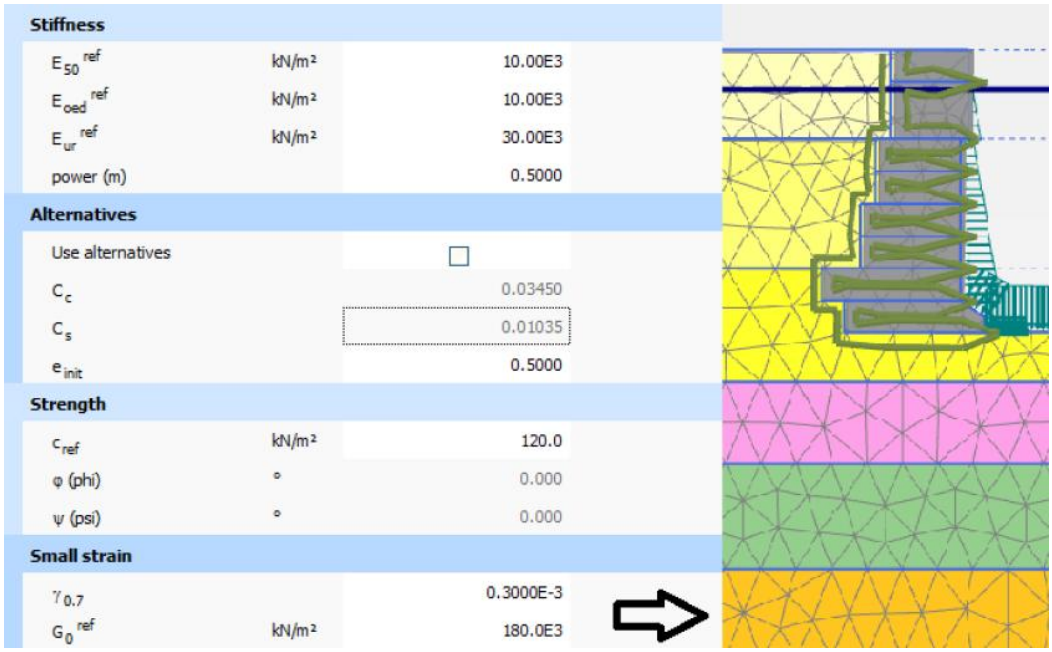

Figure 4.17: Parameters of soft marl (Dr=40%, Dr=65% and Dr=80%)

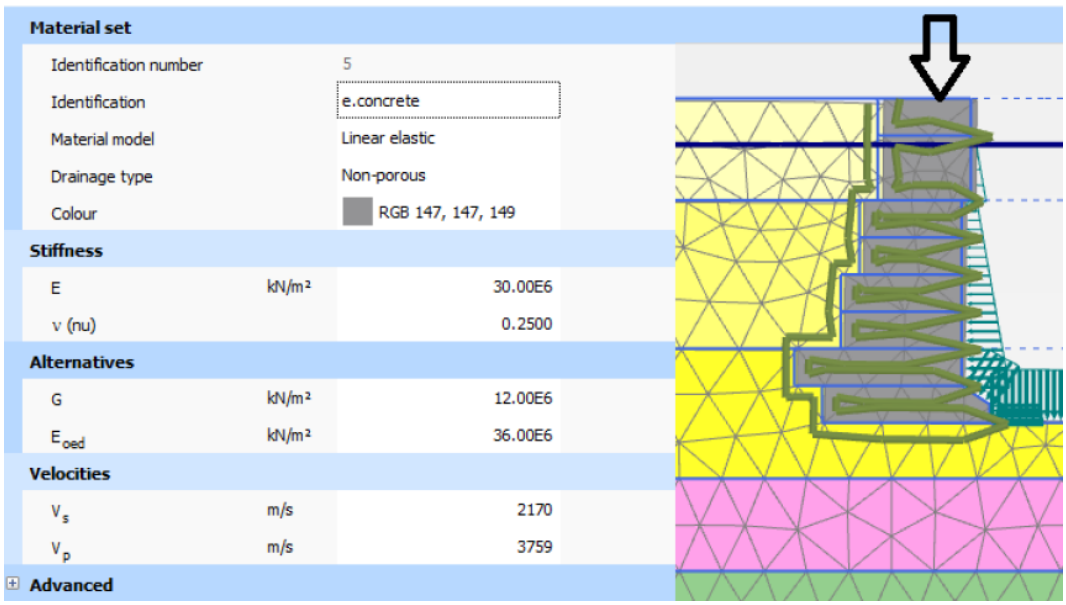

Figure 4.18: Parameters of concrete (Dr=40%, Dr=65% and Dr=80%)

Chapter 5

Excitation

5.1 Input excitations

The following figures reveal the horizontal ground motions, which have been used in the numerical dynamic analyses.
They have been selected fifteen excitations, recorded from notable seismic incidents throughout the world.

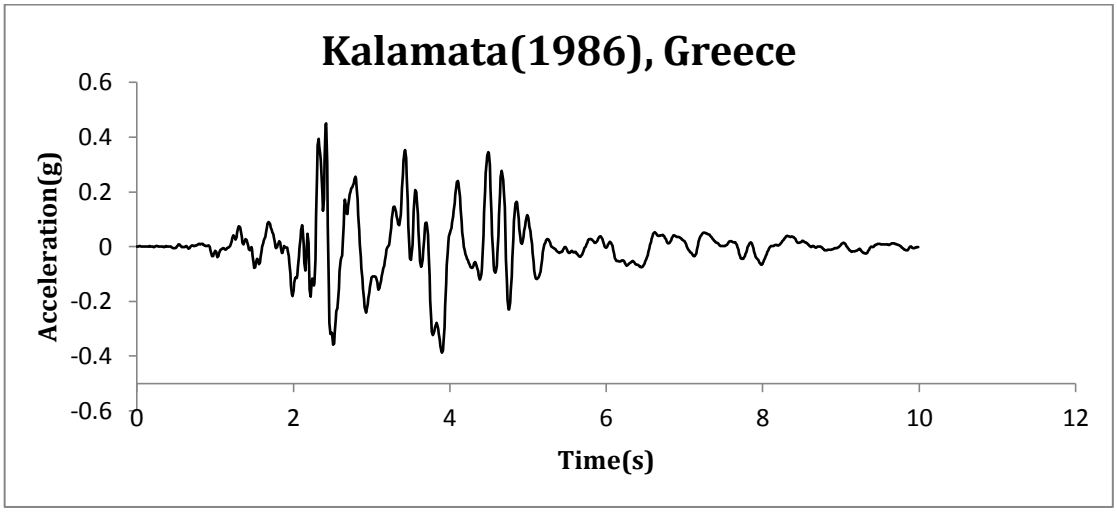

Figure 5.1: Excitation of Kalamata(1986), Greece

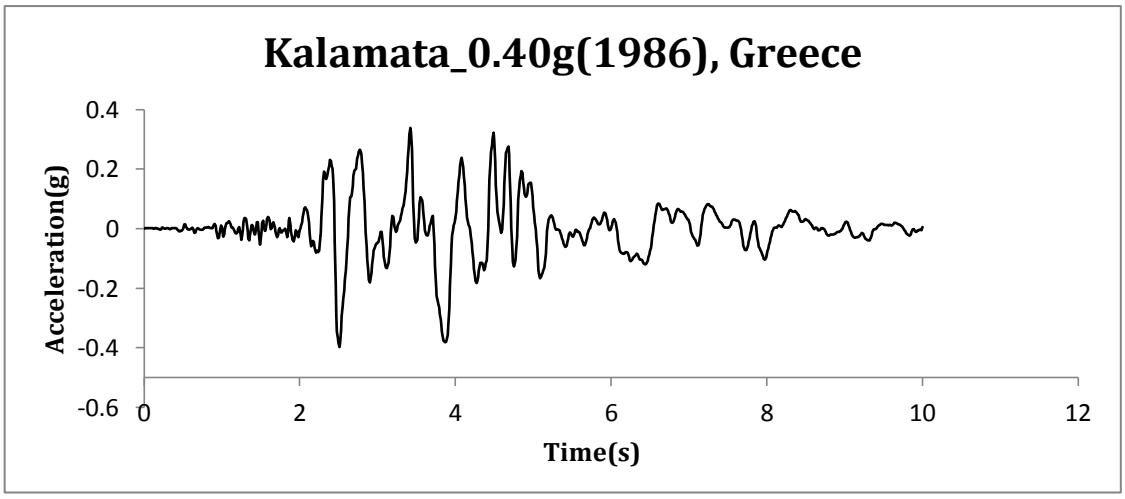

Figure 5.2: Excitation of Kalamata_04g(1986), Greece

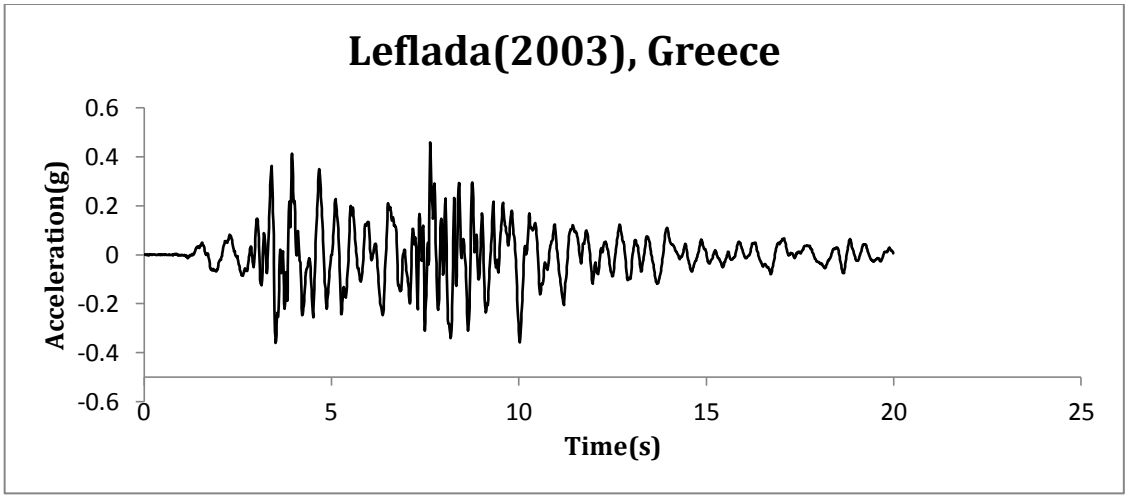

Figure 5.4: Excitation of Lefkada(2003), Greece

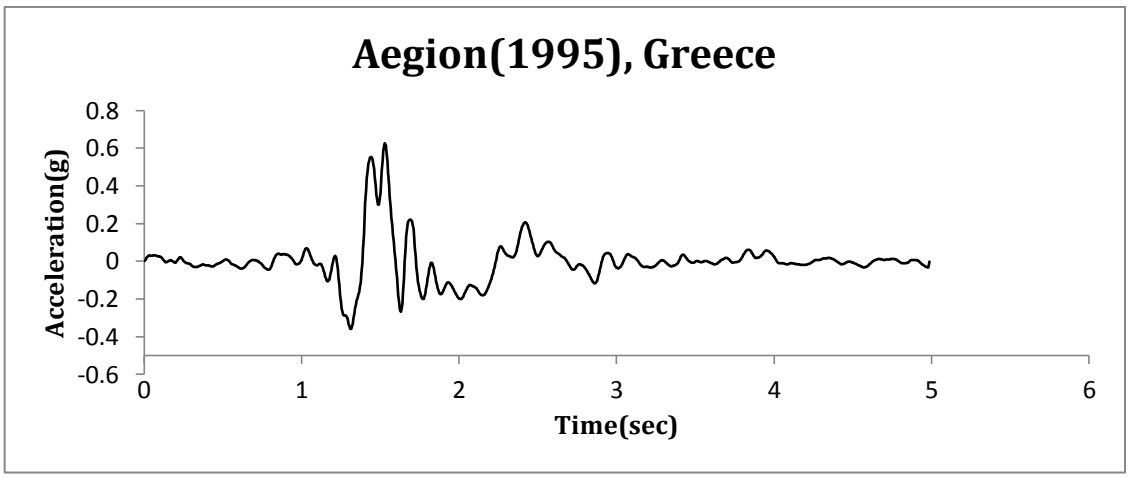

Figure 5.5: Excitation of Aegion(1995), Greece

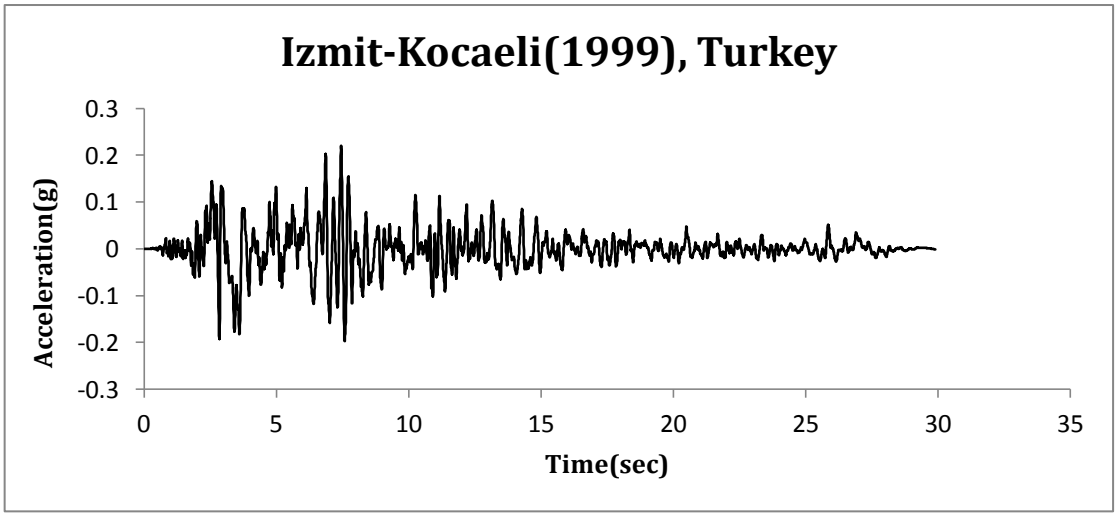

Figure 5.6: Excitation of Izmit-Kocaeli(1999), Turkey

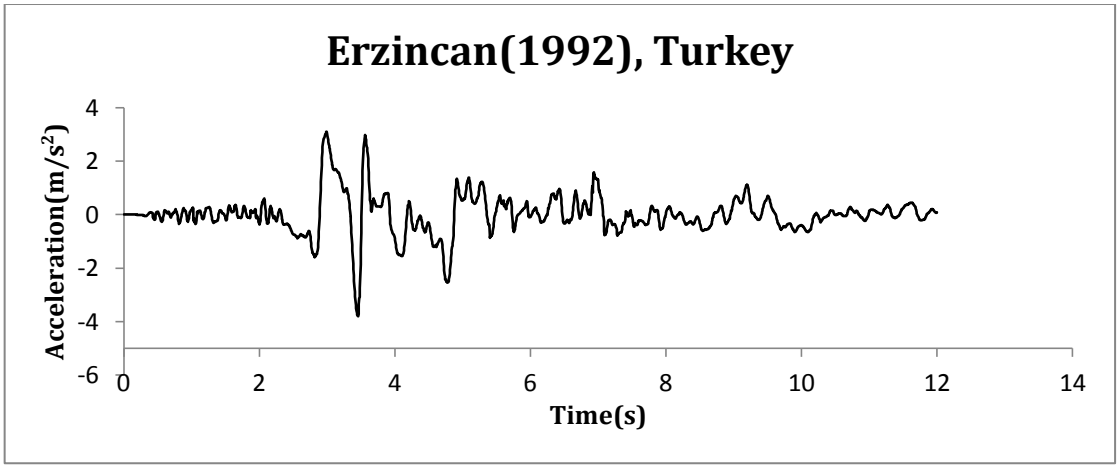

Figure 5.7: Excitation of Erzincan(1992), Turkey

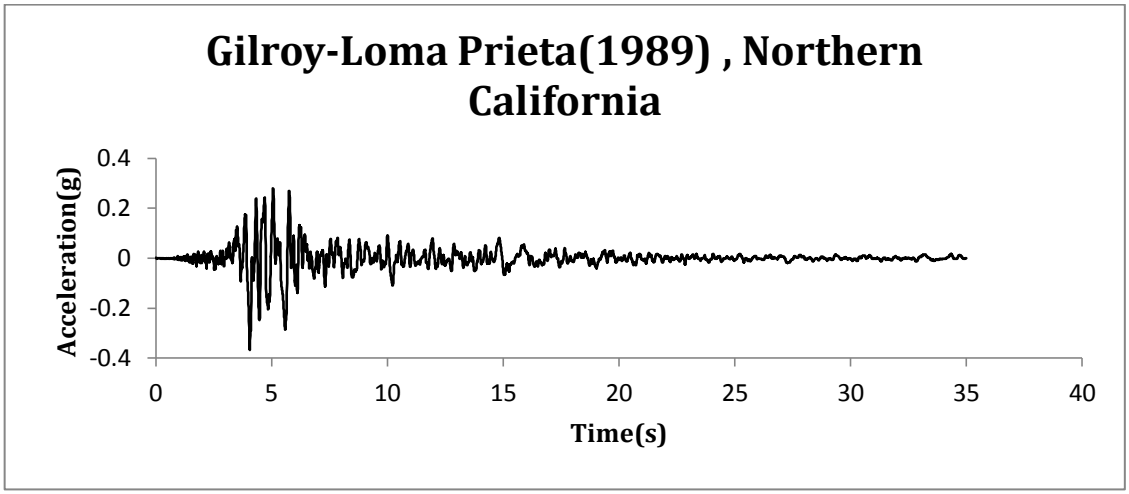

Figure 5.7: Excitation of Gilroy-Loma Prieta(1989), Northern California

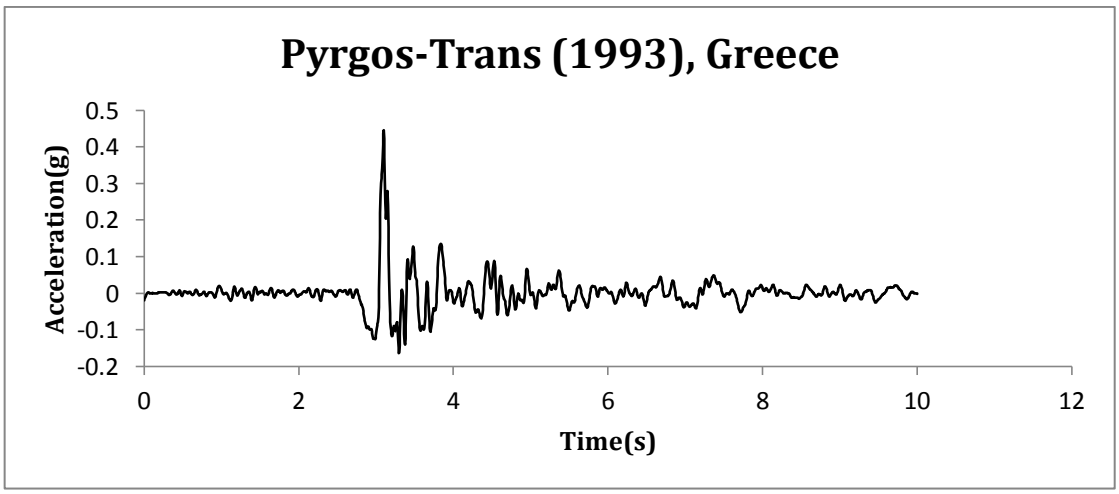

Figure 5.8: Excitation of Pyrgos-Trans (1993), Greece

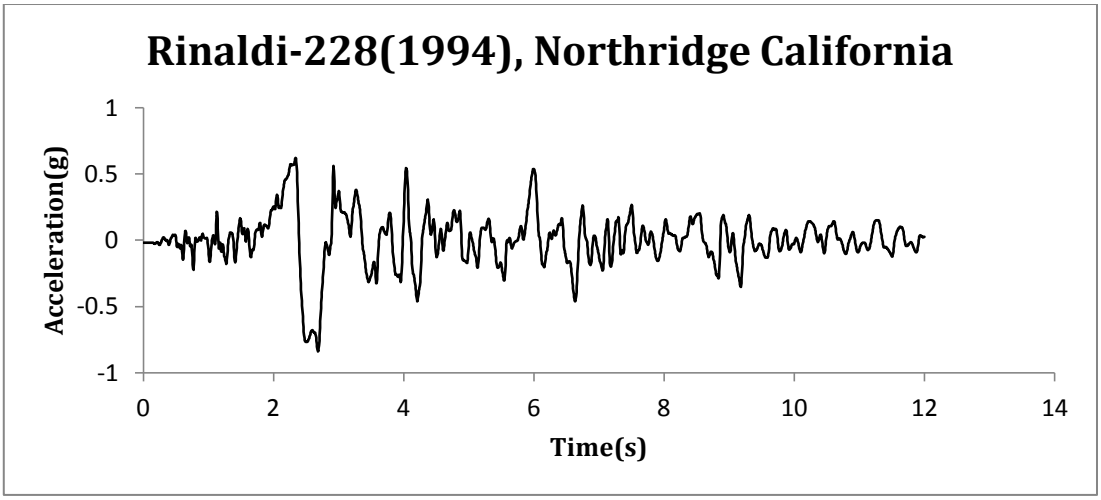

Figure 5.9: Excitation of Rinaldi-228(1994), Northridge, California

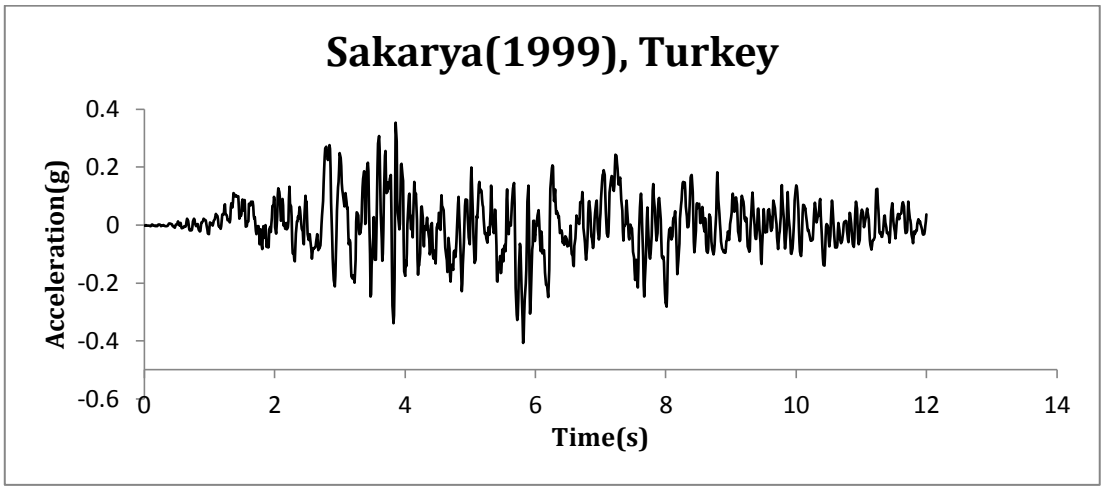

Figure 5.10: Excitation of Sakarya(1999), Turkey

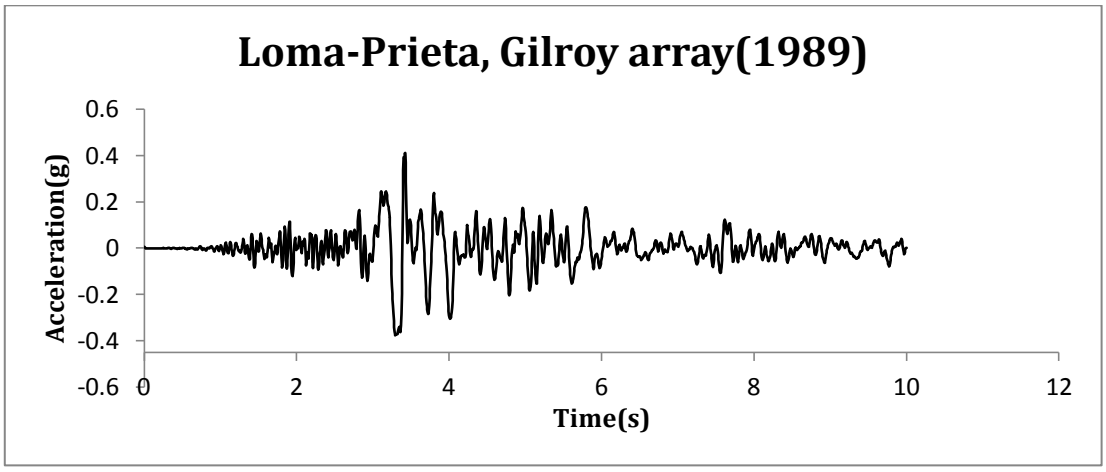

Figure 5.11: Excitation of Loma-Prieta, Gilroy array(1989), Northern California

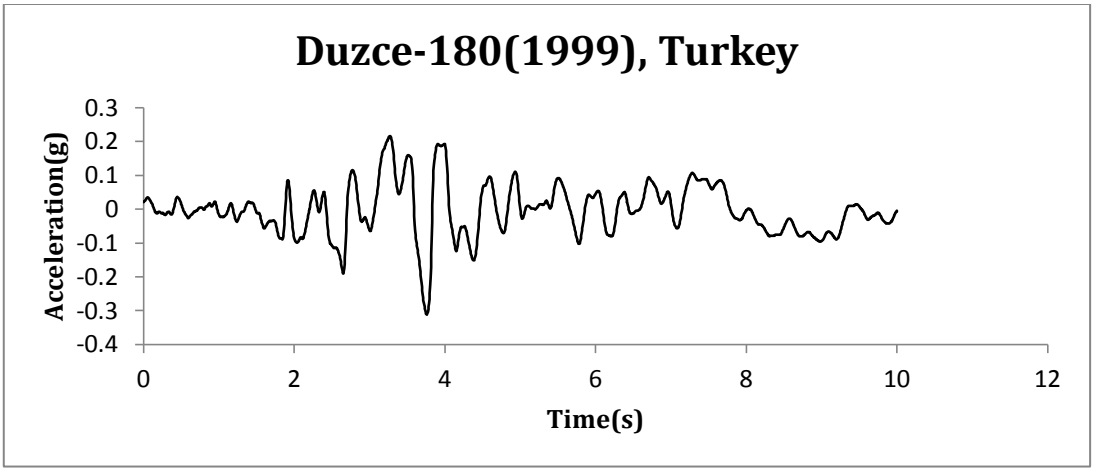

Figure 5.12: Excitation of Duzce-180(1999), Turkey

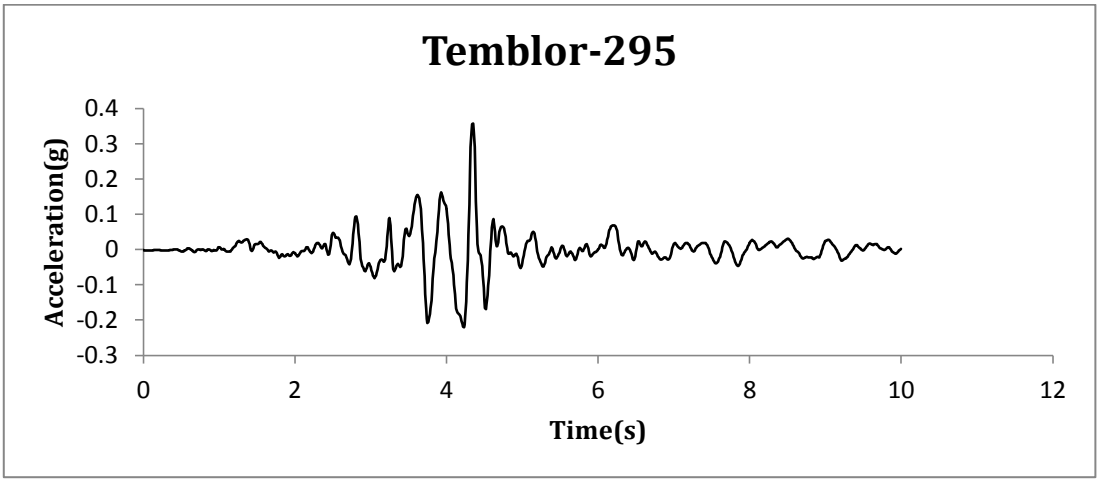

Figure 5.13: Excitation of Temblor-295

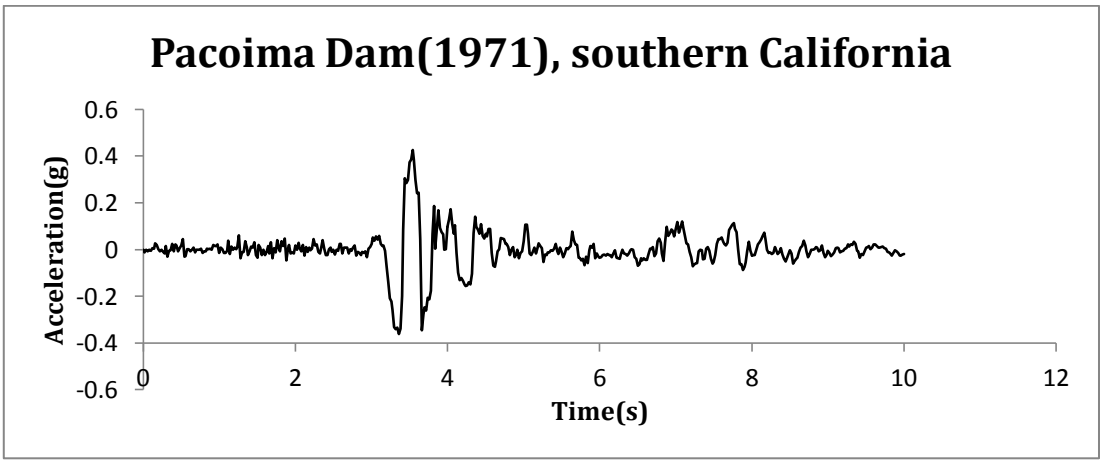

Figure 5.14: Excitation of Pacoima Dam(1971), southern California

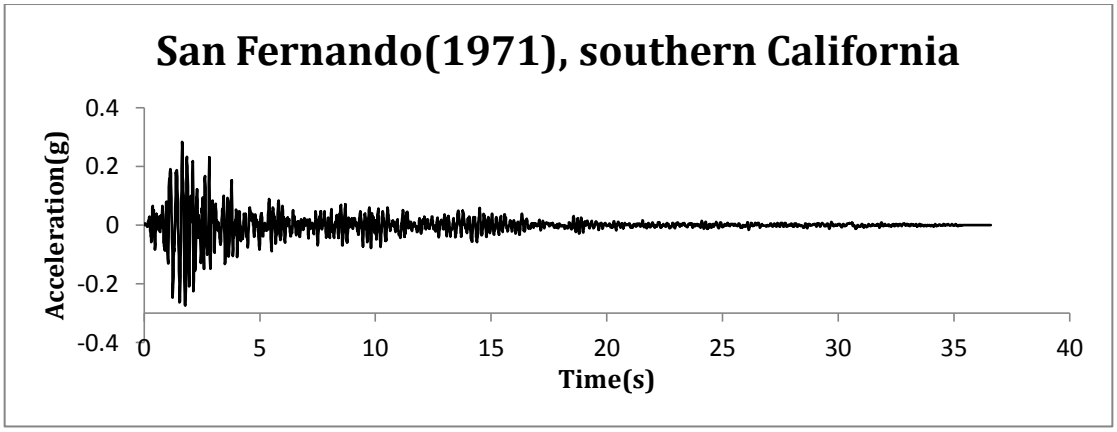

Figure 5.15: Excitation of San Fernando(1971), southern California

5.2 Reduction of excitations

In order to derive the *Fragility Curves* hinged on the maximum ground acceleration, it has been required to discretize the input accelograms by placing their maximum value on the scale of 0.1g, 0.2g, 0.4g and 0.6g. An example of this reduction is shown in Figure 5.16.

As a consenquence, besides the fact that the appropriate discretization of ground acceleration is succeeded, as well the influence of shear amplitude in saturated soil it is figured.

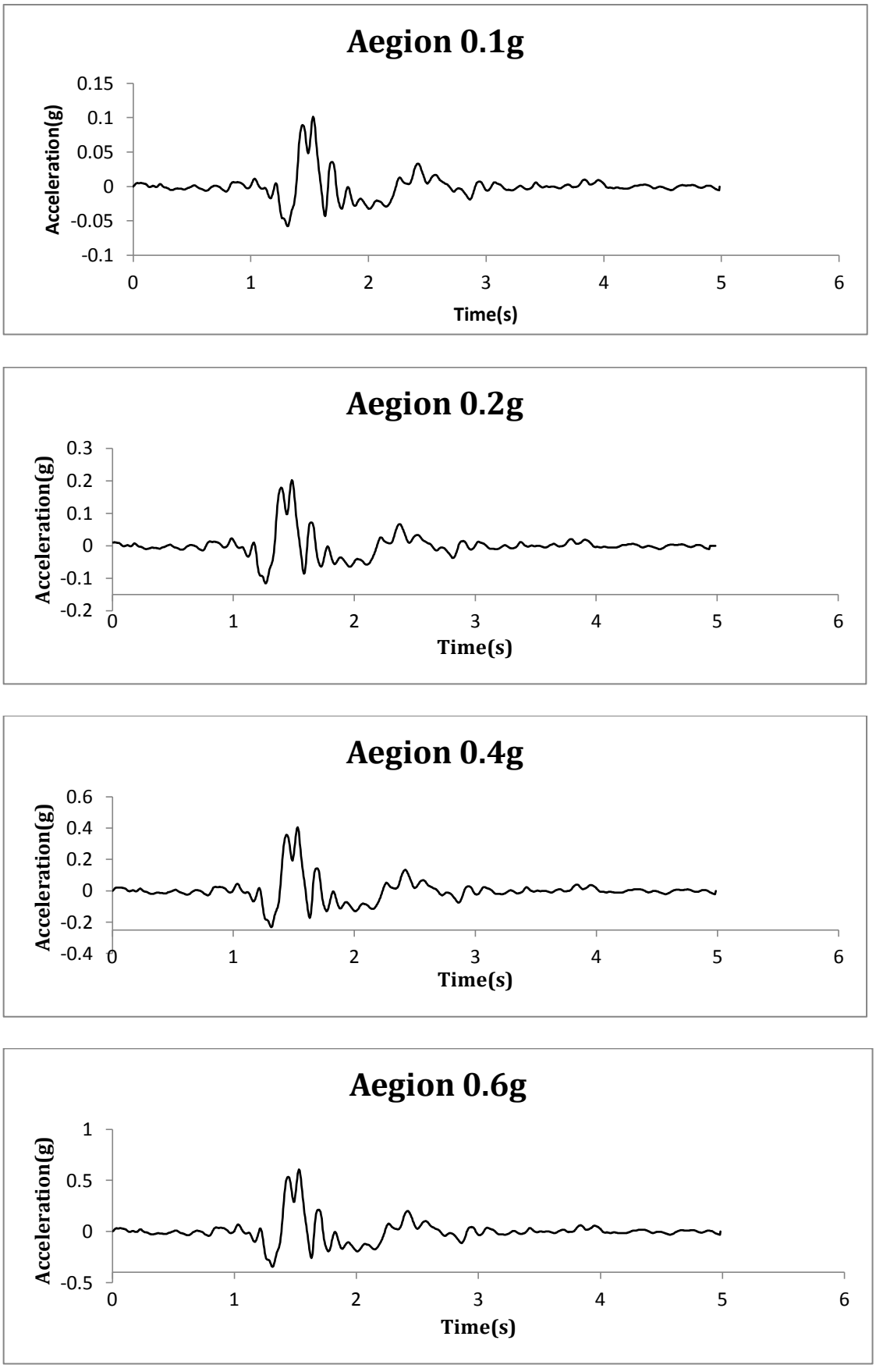

Figure 5.16: Application of excitation reduction on Aegion(1995), Greece earthquake

5.3 Direction of base excitation

As already mentioned before, in this model the X-axis boundaries were chosen to be *Tied degrees of freedom.* This resulted in the development of a model symmetrical to the vertical axis as is revealed in Figure 5.17 [Plaxis2D, Knowledge Base].

Despite the fact that the number of finite elements has been doubled, likewise the calculation time, an importand benefit has been gained. The direction of the base excitation can be of great significance. Figure 5.17 portrays for two excitation directions (+) and (-) the response of a sliding block subjected to a directivity-affected ground motion
[Gazetas G., Garini E., I. Anastasopoulos and T. Georgarakos].

The fifteen excitations, which were used in the analyses, cause a comletely different responce of quay wall, based on the direction of ground motion and therefore, information is obtained from aparently thirty excitations.

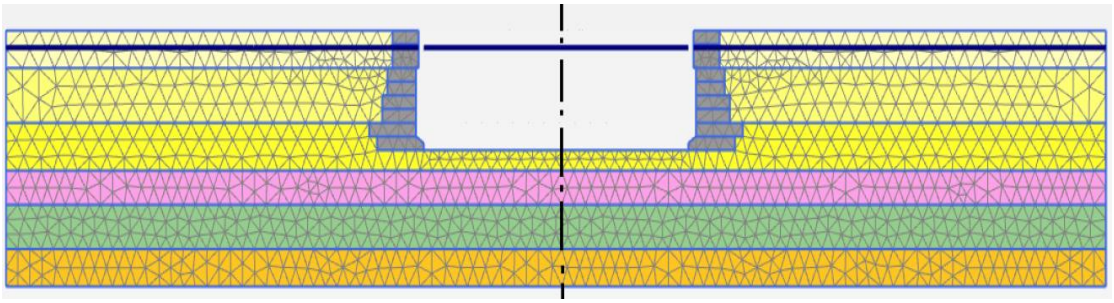

Figure 5.17: Symmetrical to the vertical axis model

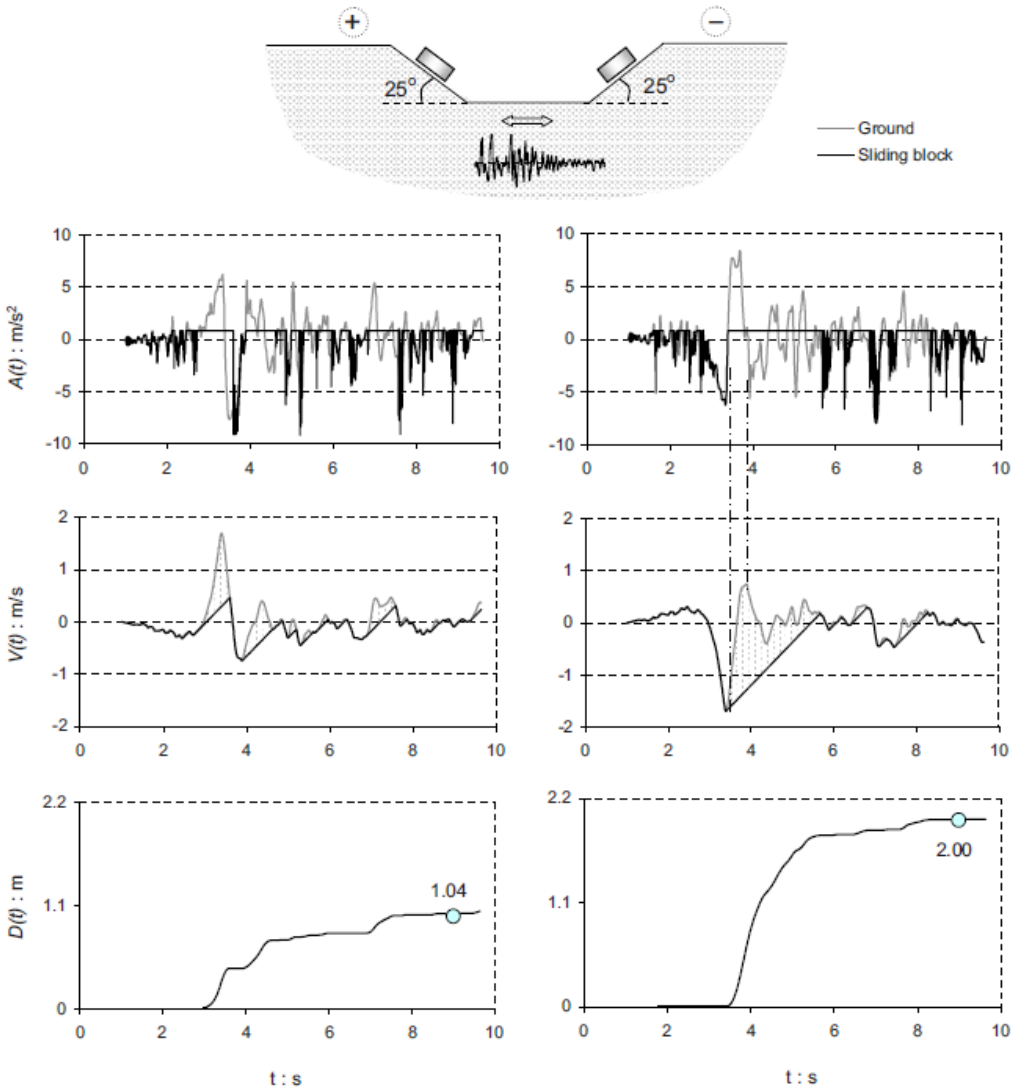

Fig. 17. Acceleration, velocity, and displacement time histories for the Rinaldi record (228° component) when imposed parallel to the sliding interface (inclination angle β=25° and a_C/a_P=0.1). Notice the asymmetric response of the block when the excitation is inverted (plots in right) the well-shaped forward-directivity pulse, shown between the dotted lines, now causes a major slippage of 2 m [Gazetas G., Garini E., I. Anastasopoulos and T. Georgarakos].

Chapter 6

Numerical results

6.1 Fragility Curves

6.1.1 Introduction

Quay wall's *Fragility Curves* are presented in order to evaluate its seismic dispacements according to the already operational damage critiria for port structures, likewise to obtain an overlook in the way, parameters as the relative density and the amplitude of the peak ground acceleration, affect its dynamical response.
They are revealed *Fragility Curves* for quay wall's horizontal displacement, tilt and backfill settlement behind the wall.

Attaching the former damage levels, which are meantioned in the paragragh 2.4.2, to the Piraeus Port quay wall, the fragility criteria according to PIANC are the following:

- Degree I - "Serviceable" : the residual horizontal displacement level of exceedance should be 0,25m and the residual tilt level of exceedance should be 3^{o}
- Degree II - "Repairable" : the residual horizontal displacement level of exceedance should be 1,0m and the residual tilt level of exceedance should be 5^{o}
- Degree III - "Near collapse" : the residual horizontal displacement level of exceedance should be 1,7m and the residual tilt level of exceedance should be 8^{o}
- Degree IV - "Collapse" : the residual horizontal displacement level of exceedance should be 3,5m and the residual tilt level of exceedance should be 12^{o}

In order to figure the curves more comprehensively, lower fragility levels have been selected for for the Degrees I, II, III and IV, which are 0,25m, 0,75m, 1,5m and 2,5m for the residual horizontal displacement, correspondingly, and 1^{o}, 2^{o}, 3^{o} and 4^{o}, respectively, for the residual tilt.

6.1.2 Fragility curves according to PIANC criteria

6.1.2.1 Backfill soil with Dr=40%

Horizontal displacement

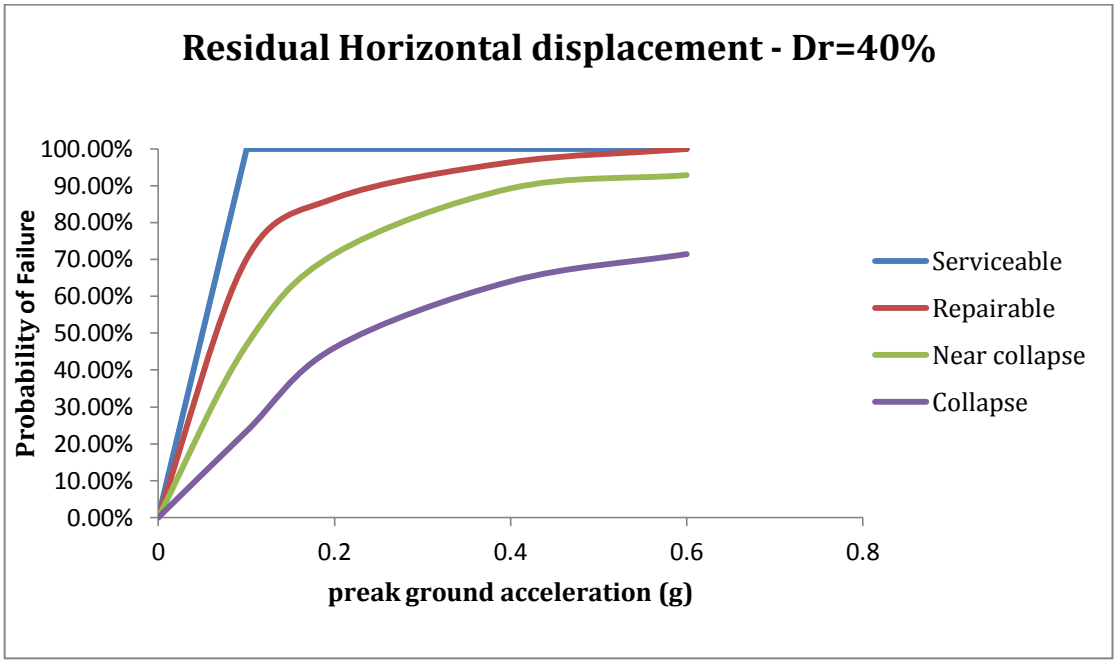

Quay wall tilt

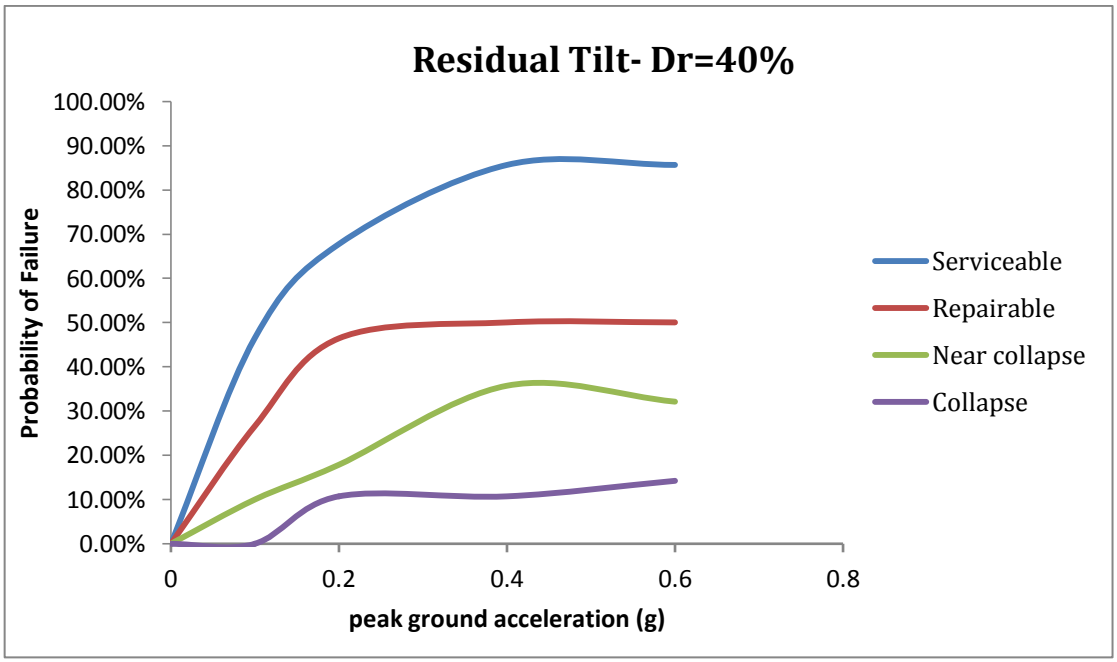

Backfill soil settlement

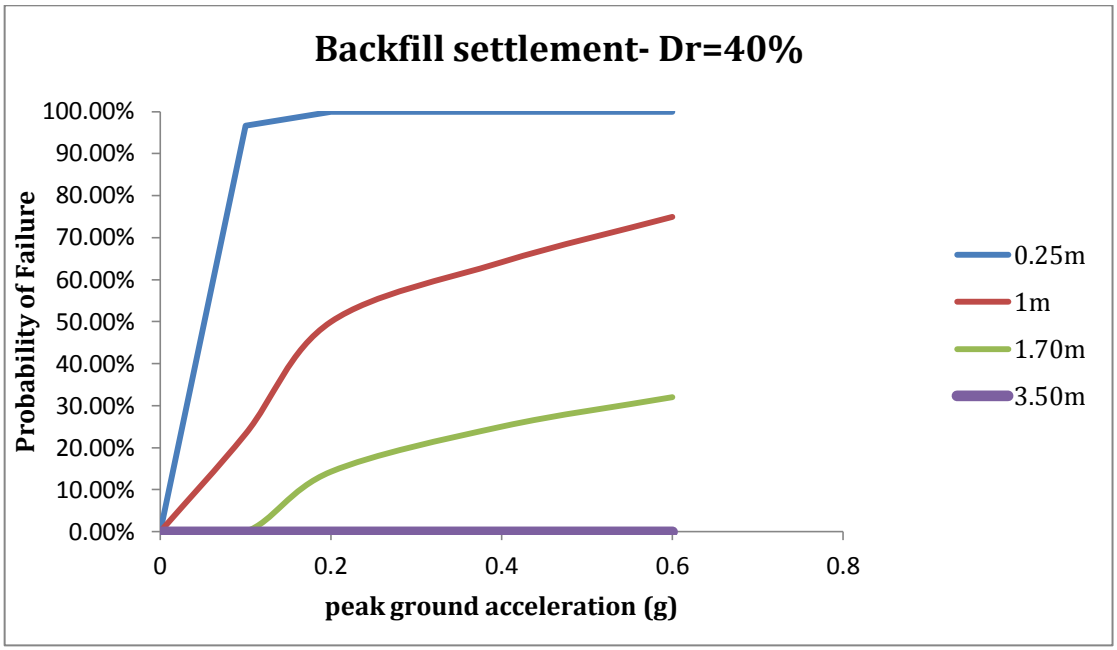

6.1.2.2 Backfill soil with Dr=65%

Horizontal displacement

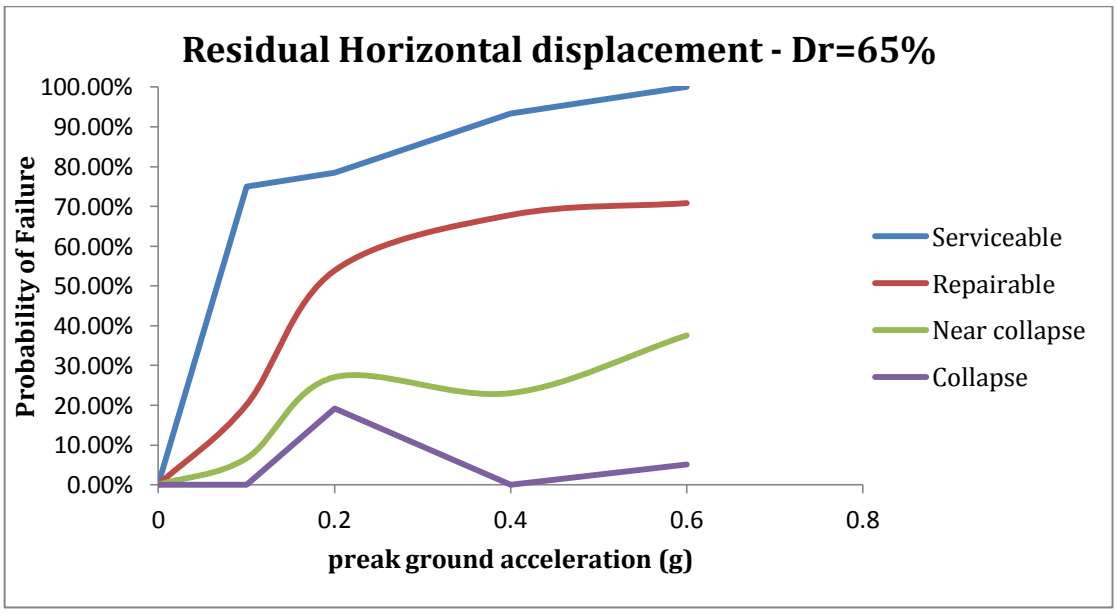

Quay wall tilt

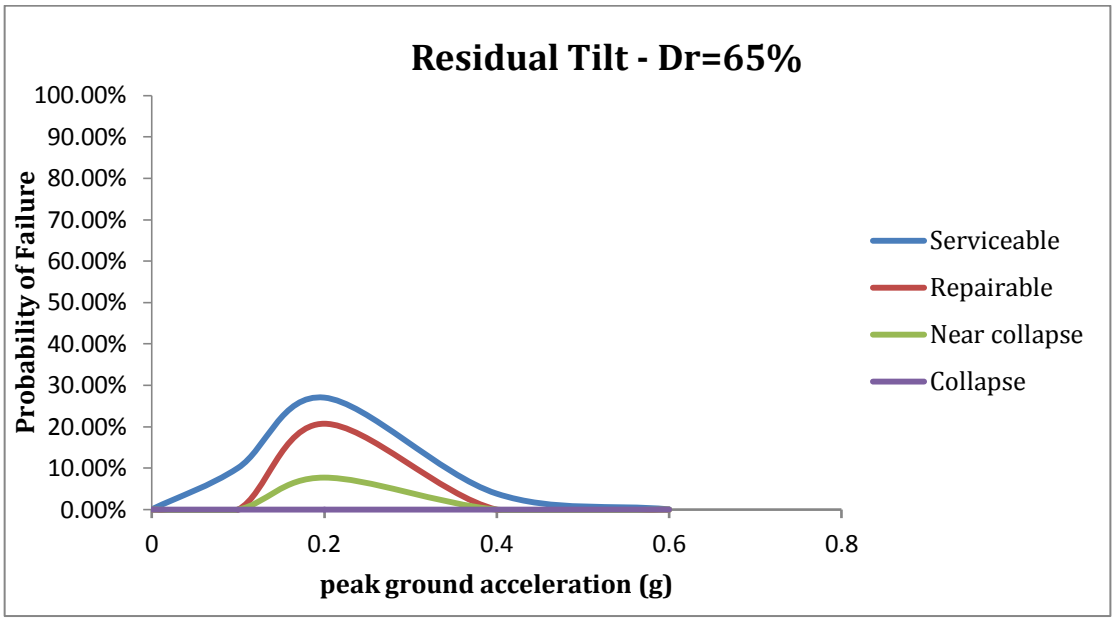

Backfill soil settlement

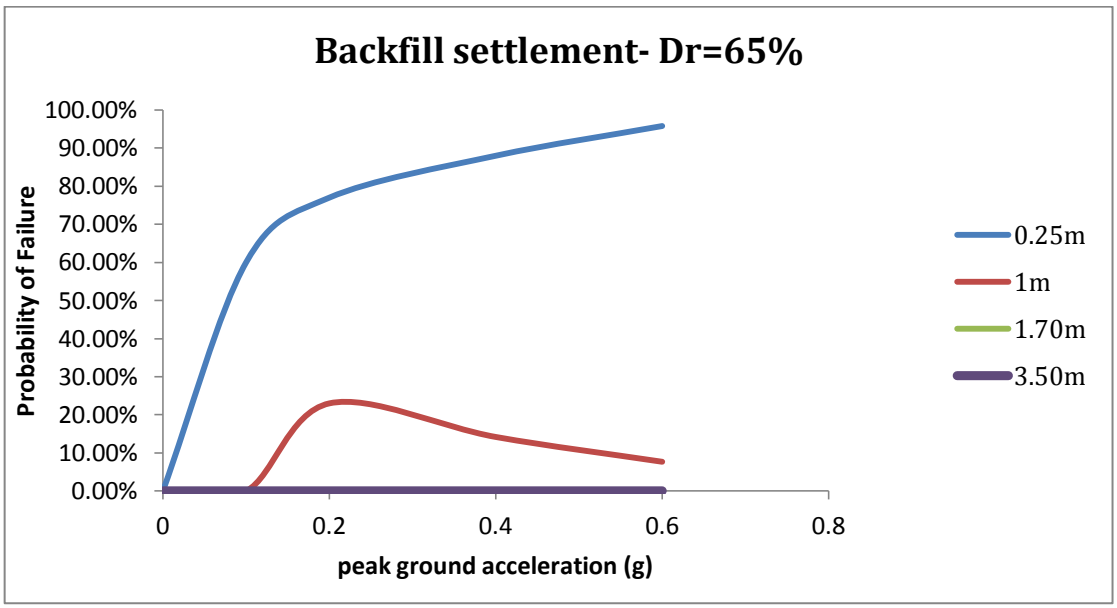

6.1.2.3 Backfill soil with Dr=80%

Horizontal displacement

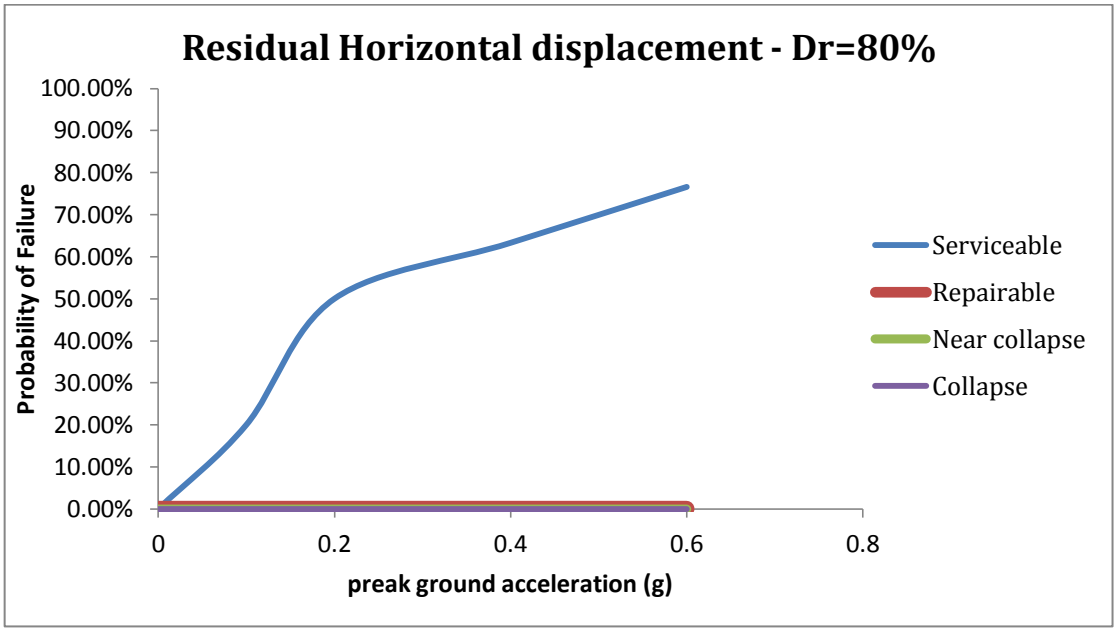

Backfill soil settlement

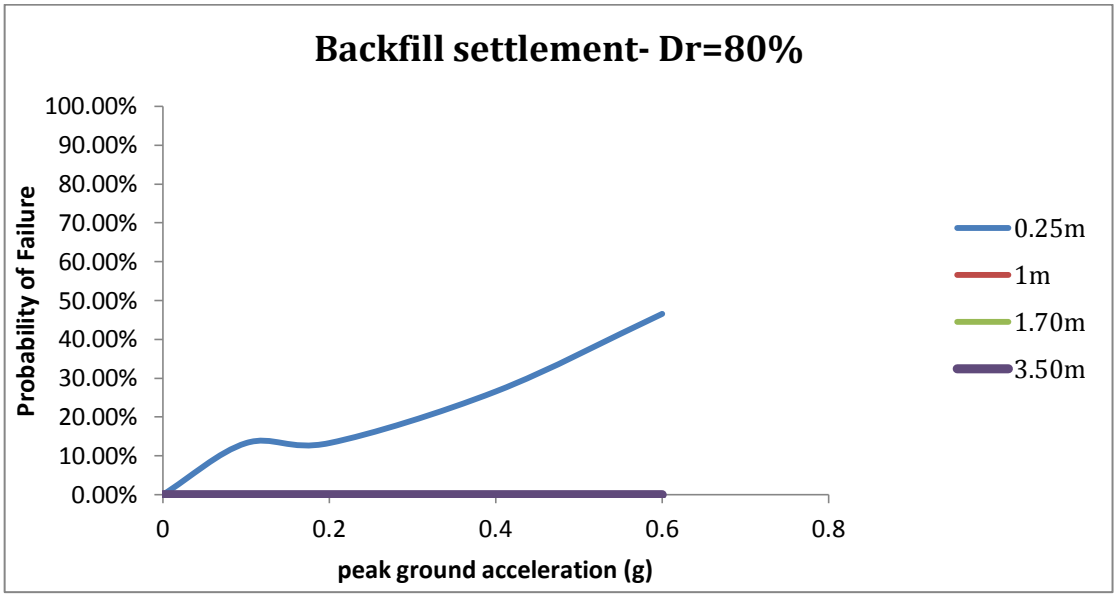

6.1.3 Fragility Curves with lower fragility levels

6.1.3.1 Backfill soil with Dr=40%

Horizontal displacement

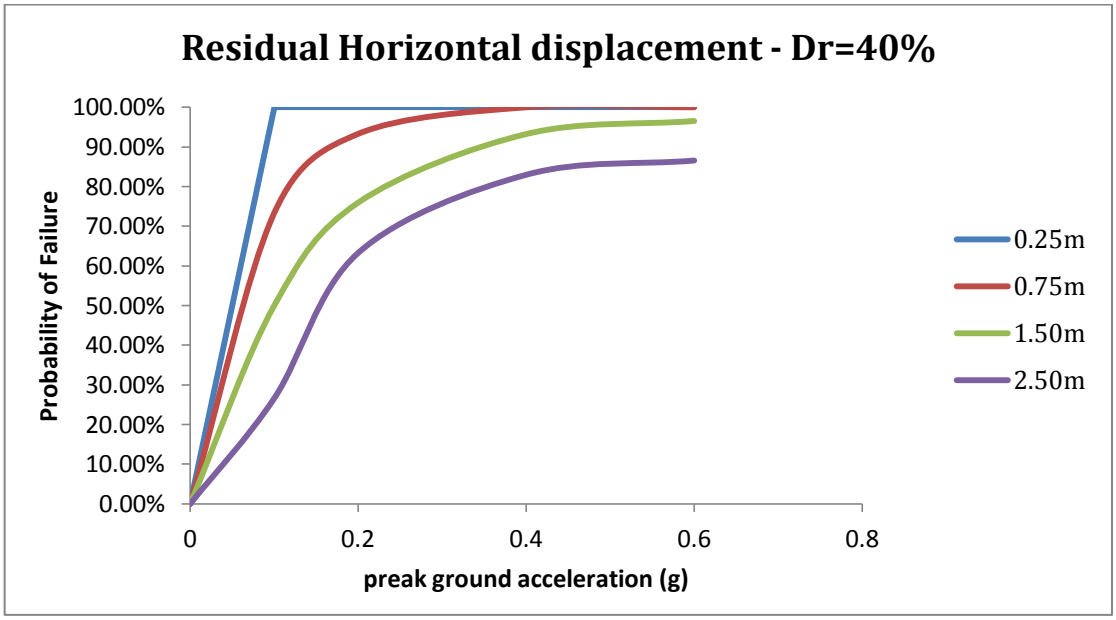

Quay wall tilt

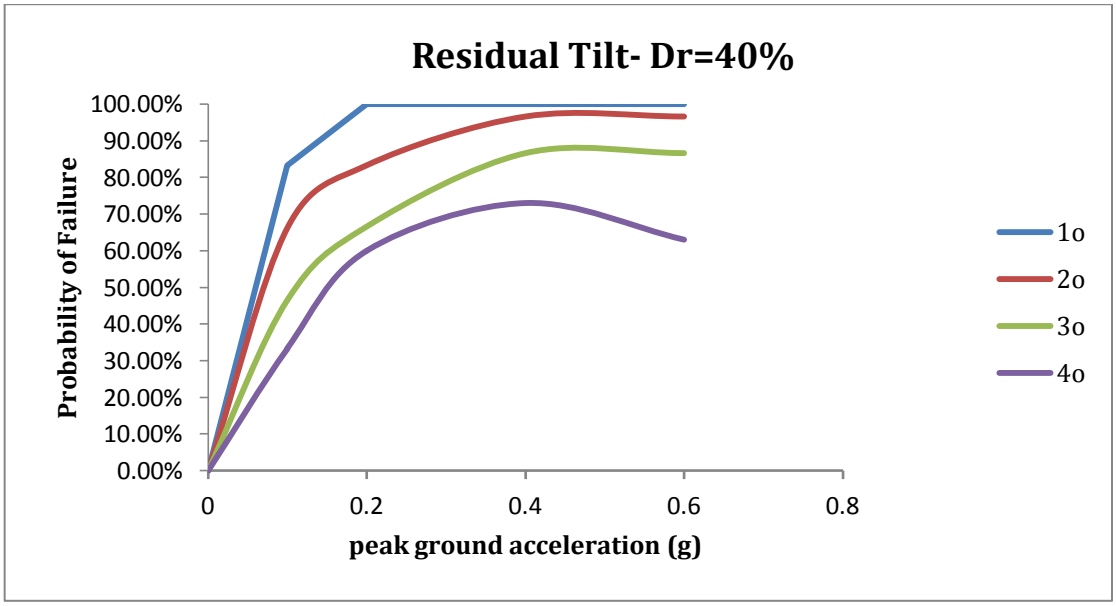

Backfill soil settlement

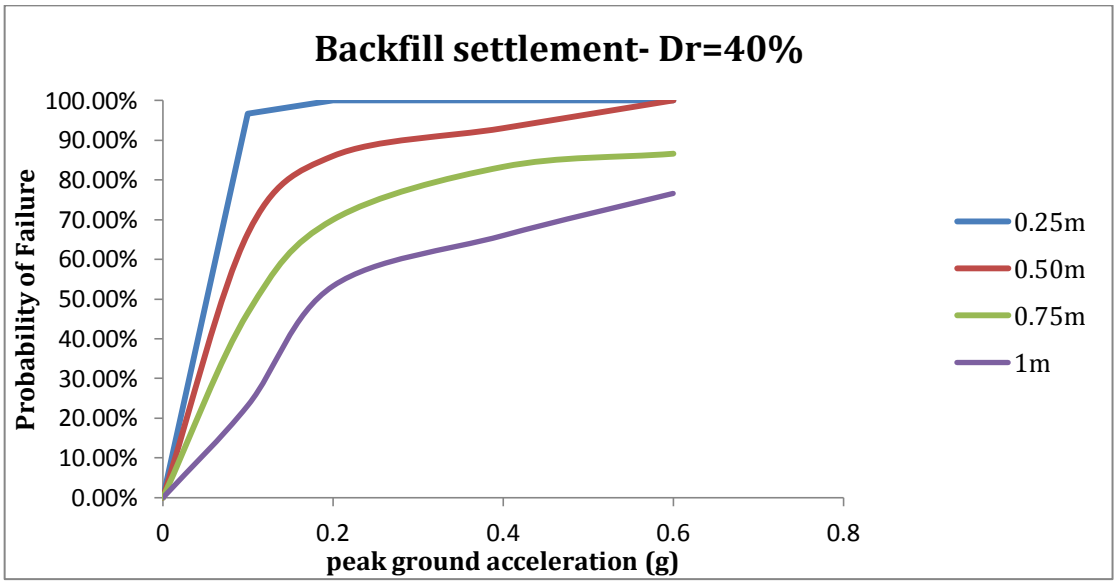

6.1.3.2 Backfill soil with Dr=65%

Horizontal displacement

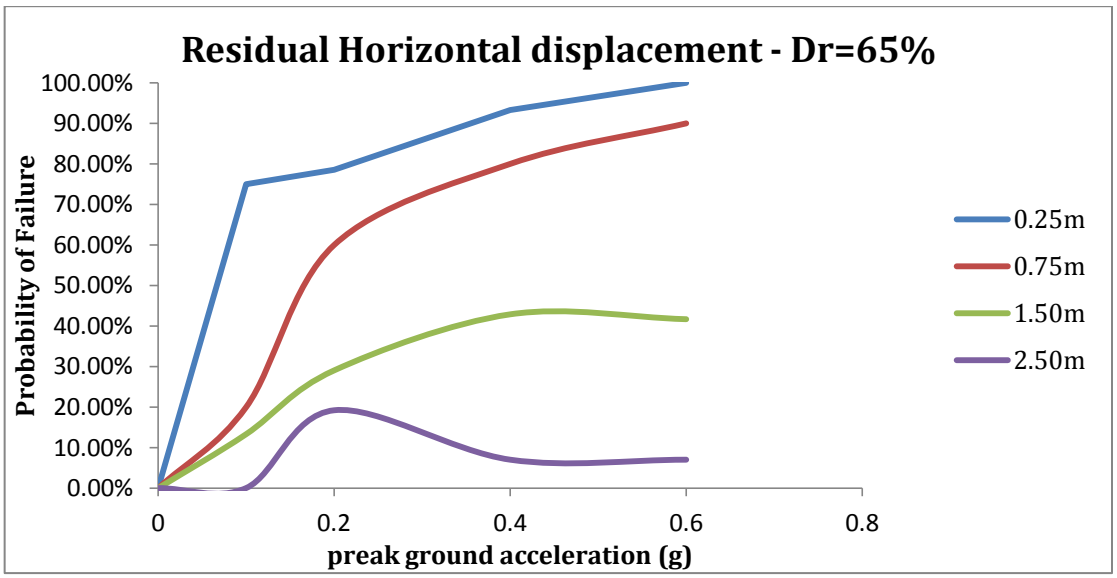

Quay wall tilt

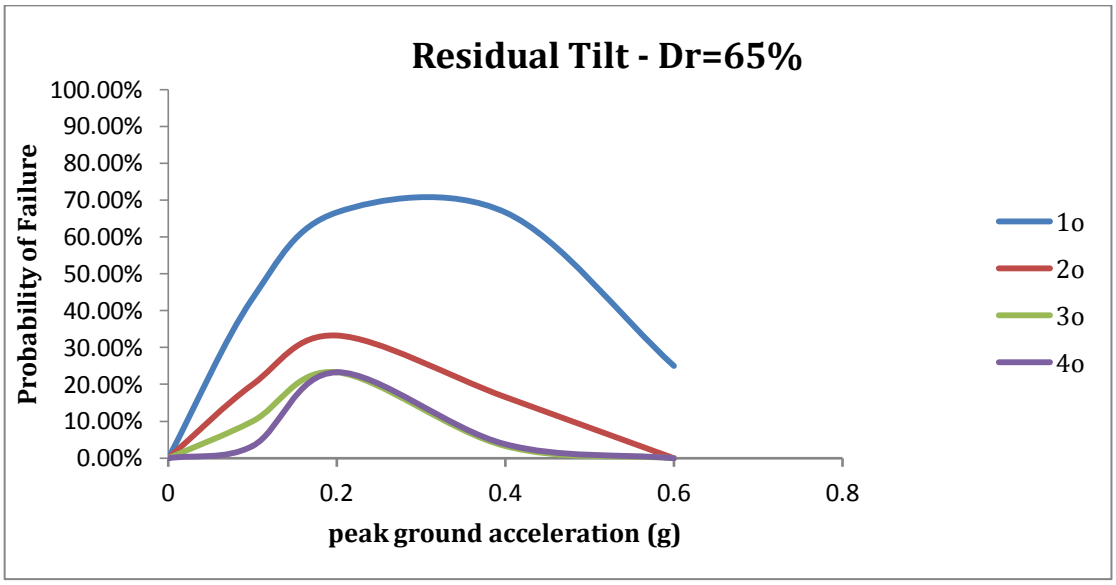

Backfill soil settlement

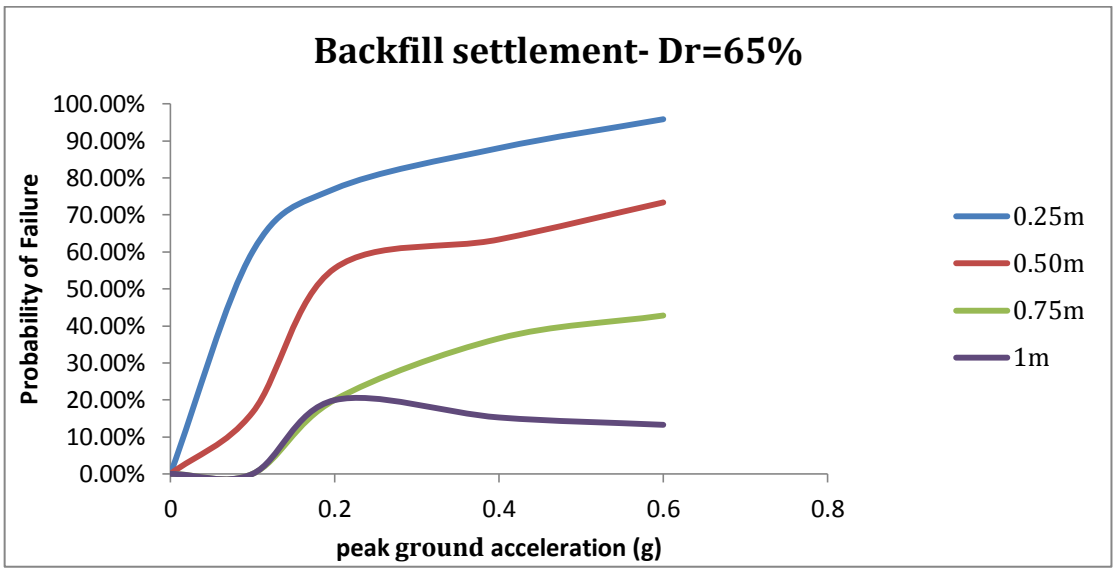

6.1.3.3 Backfill soil with Dr=80%

Horizontal displacement

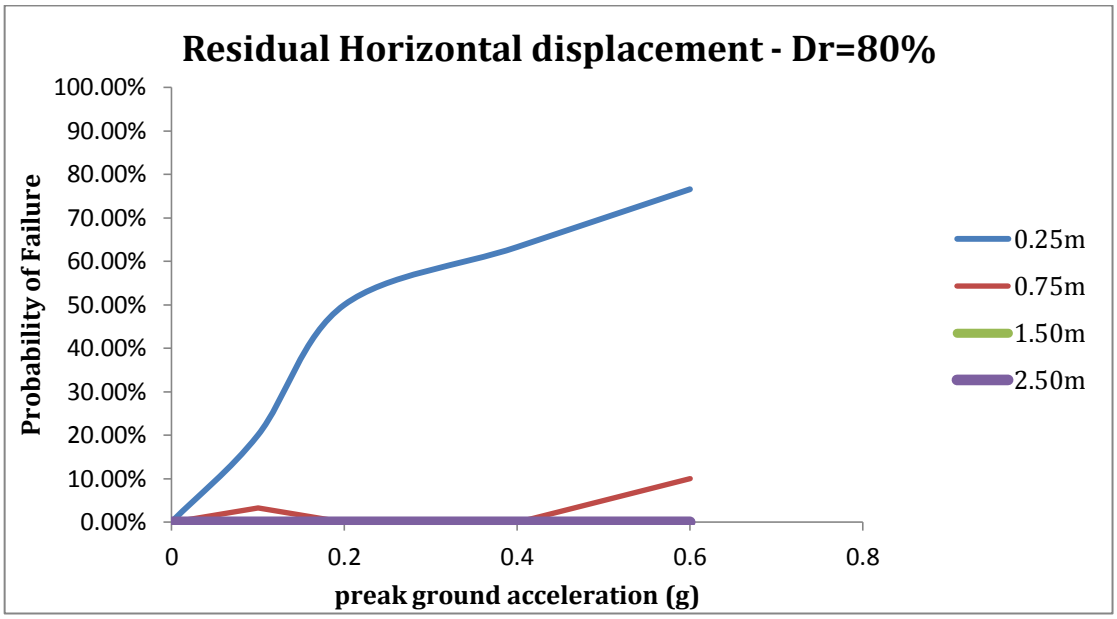

Backfill soil settlement

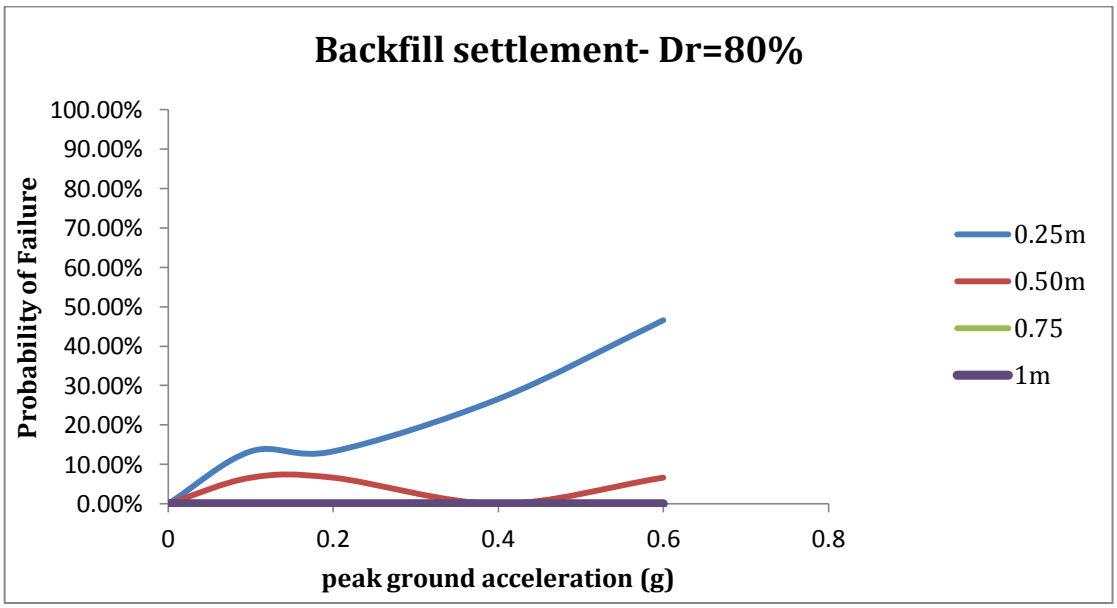

6.2 Results of dynamic analysis and discussion

6.2.1 Displacements

Data of the dynamic process could arguably verify that quay walls suffered detrimental displacements, alike with them, which were caused from real seismic insidents. Figures 6.1-6.3 portrays the contours of horizontal displacement of quay wall at the Models 1, 2 and 3 correspondingly, caused by four powerful ground motions, at the end of shaking.

Obviously, the enxtent of quay wall's and soil's deformations varied throughout the different relative density of backfill soil and the value of peak ground acceleration because of the range that liquefaction occurs at the retained soil behind the wall and at the foundation zone.

Therefore, it is vitally importand to performe a more closer look at these two parameters, relatively with their role at soil-quay way interaction

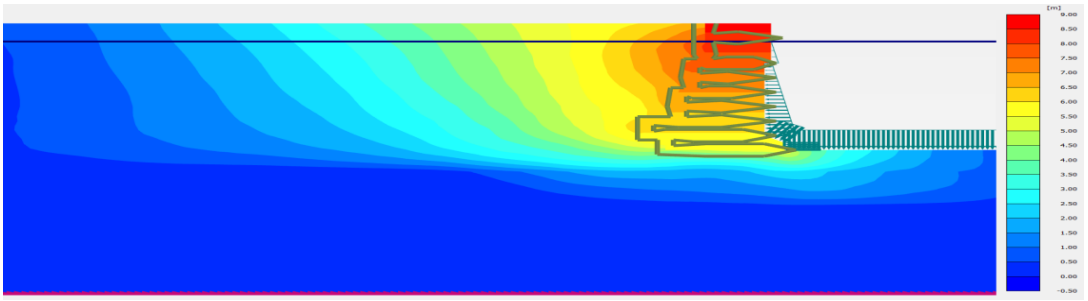

(a)

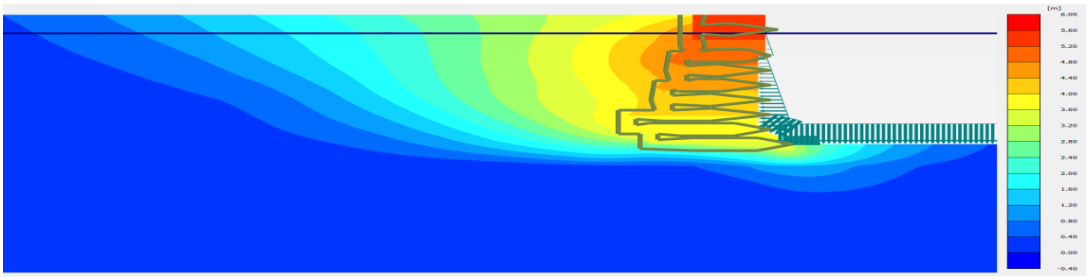

(b)

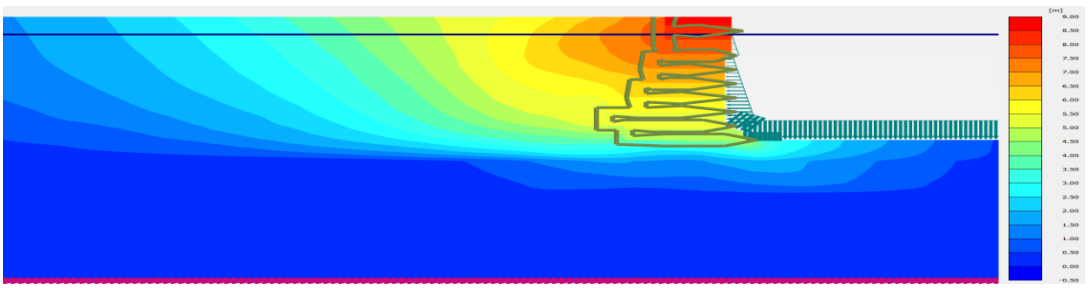

(c)

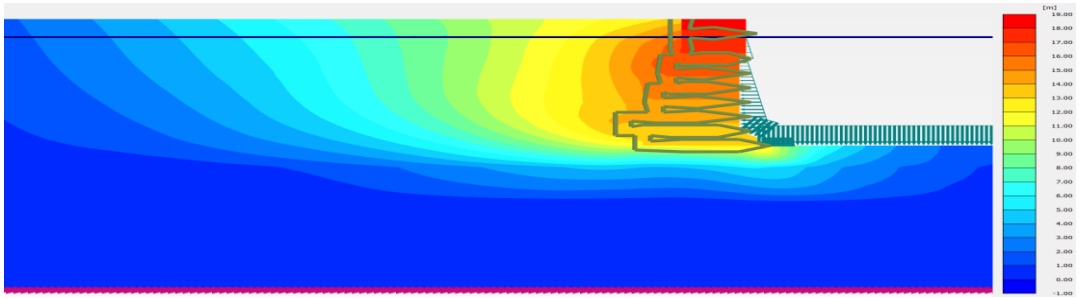

(d)

Figure 6.1: Contours of horizontal displacements of quay wall and soil - Model 1(Dr=40%) at (a) Lefkada(2003)_0.4g, (b) Erzincan(1992)_0.4g, (c) Gilroy-Loma Prieta_0.4g and (d) Izmit(1999)_0.4g

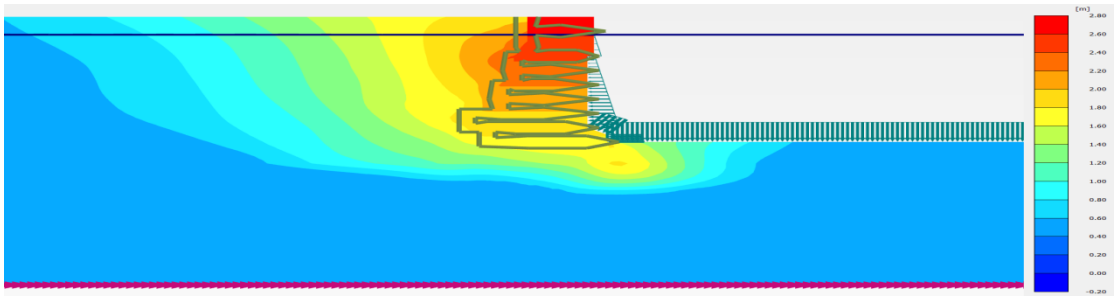

(a)

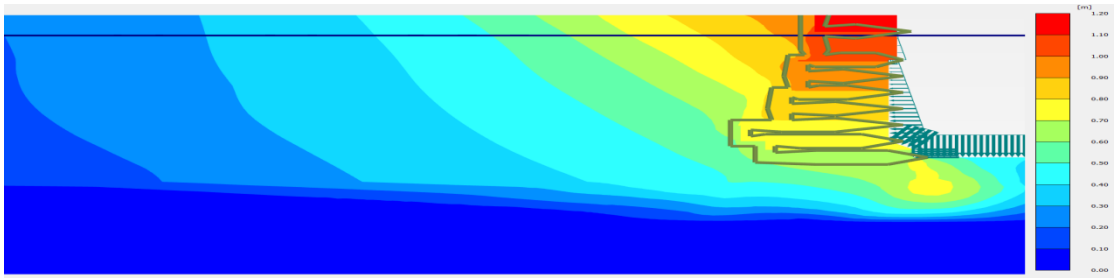

(b)

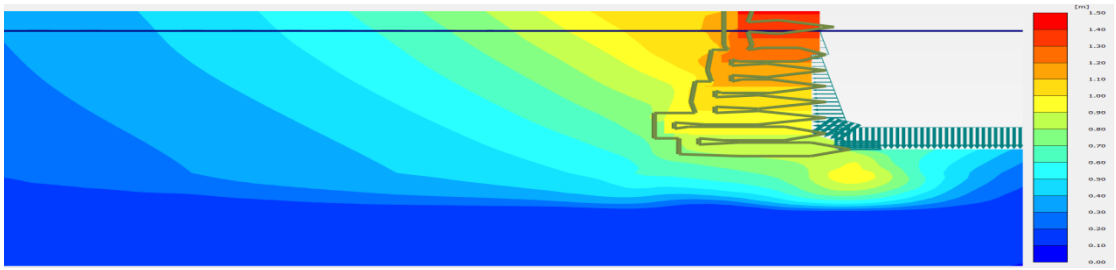

(c)

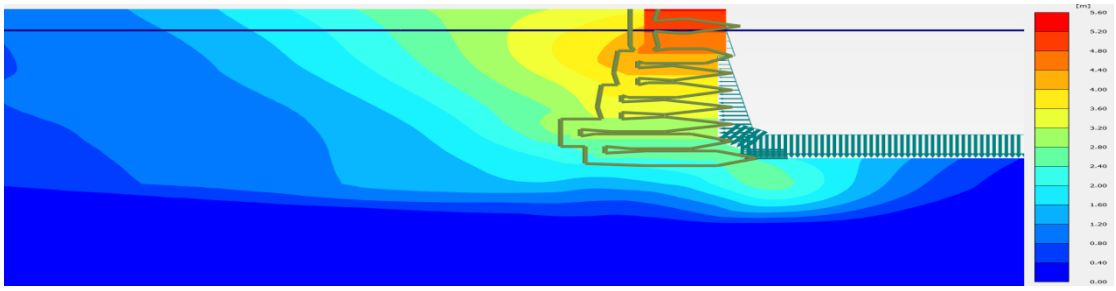

(d)

Figure 6.2: Contours of horizontal displacements of quay wall and soil - Model 2(Dr=65%) at (a) Sakarya_0.4g, (b) Templor_0.6g, (c) Rinaldi_0.2g and (d) Lefkada_0.6g

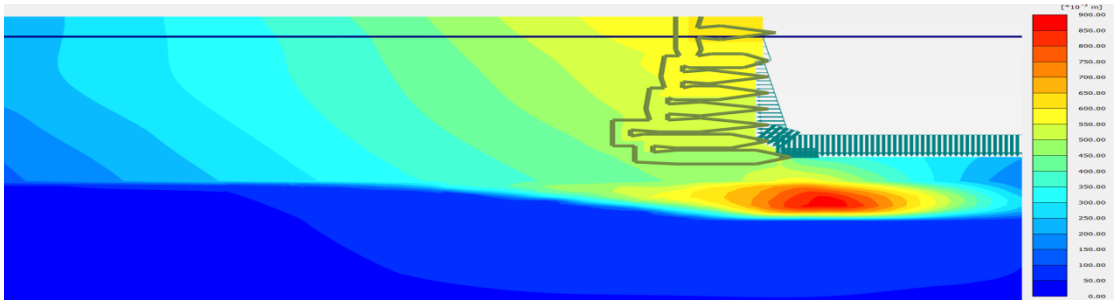

(a)

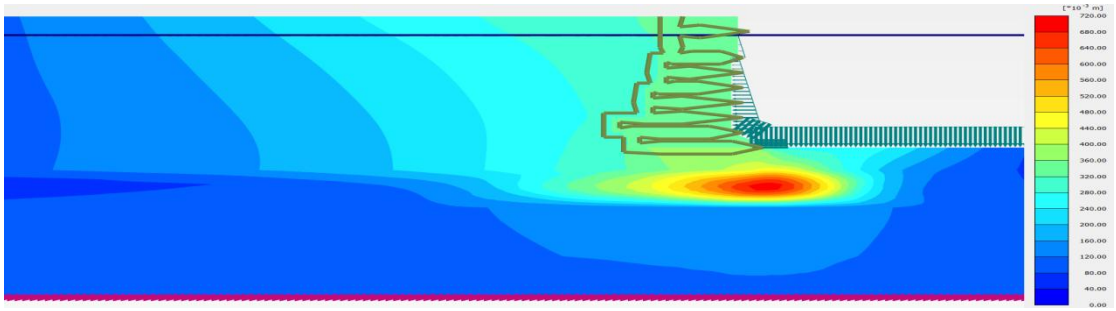

(b)

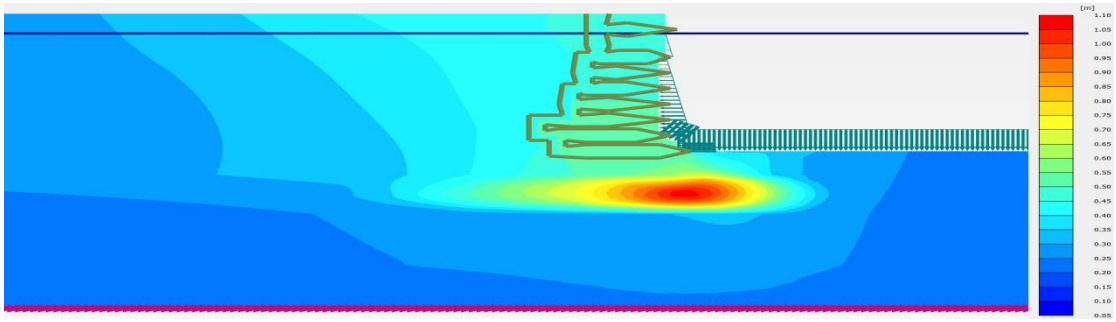

(c)

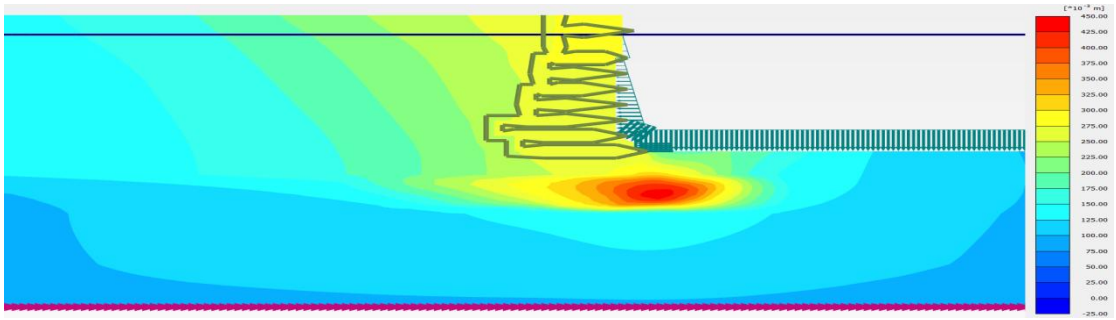

(d)

Figure 6.3: Contours of horizontal displacements of quay wall and soil - model 3(Dr=80%) at (a) San Fernando_0.4g, (b)Kalamata(1986)_0.6g, (c) Rinaldi_0.6g and (d)Loma-Prieta_0.6g

6.2.2 Influence of Relative Density

The relative density of the backfill soil reveals a major role in quay wall's horizontal displacement and tilt, since it is responsible for its liquefaction potential and as a consequence for significan soil deformation. Figures 6.4 -6.6 plot the excess pore water pressure ratio $r_u=\Delta u/\sigma'_{om}$ - where Δu is excess pore water pressure and σ'_{om} is the initial mean effective stress - in relationship with the increasing relative desity of backfill soil during the same ground motion.

The loose soil, which has high trend to expand its volume, face a considerable increase of excess pore water pressure ratio r_u and, as it is liquefied, develope substaintially strong horizontal pressures, which cause lange displacement and tilt on quay wall. The dense soil moderates the extent of liquefaction and therefore quay wall does not deformed at a high level.

Furthermore, it is also importand to define the provenance of the quay wall's displacements, referencially with the relative density of backfill soil. From the contours of horizontal displacements of Figures 6.1-6.3 has already been shown that the significant horizontal displacements and tilts of quay wall, in loose soil cases, were caused by the backfill soil due to its liquefacton. An completely opposite picture it is shown in dense soil cases. Since the foundation material has the same relative density with the backfill soil, the applied increased forces upon the wall could be easily supported by the dense foundation but they weaken the above soil layer - Silty Sand - which undergo liquefaction and develop minute deformations (red contours of Figure 6.3 and ratio of excess pore water pressures of Figures 6.4-6.6 at dense soils).

Computed distributions of excess pore water pressure ratio for the backfill soil with Dr=40% and Dr=80% throughout time, during the same earthquake are ploted in Figure 6.7. From the figure it could be noticed a coprehensive view of the development of liquefaction through the maximum pore pressures, at various times, in these two different cases.

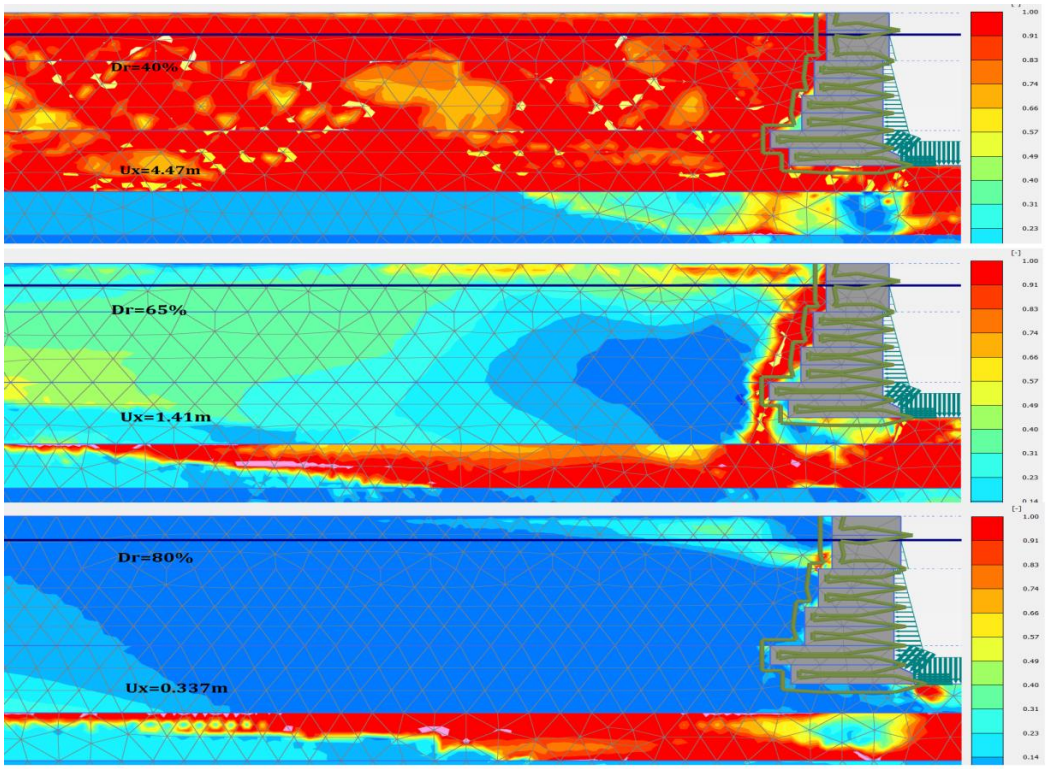

Figure 6.4: : Contours of excees pore water pressure ratio, while relative density increases, for the same excitation (Rinaldi-228 - 0.2g).

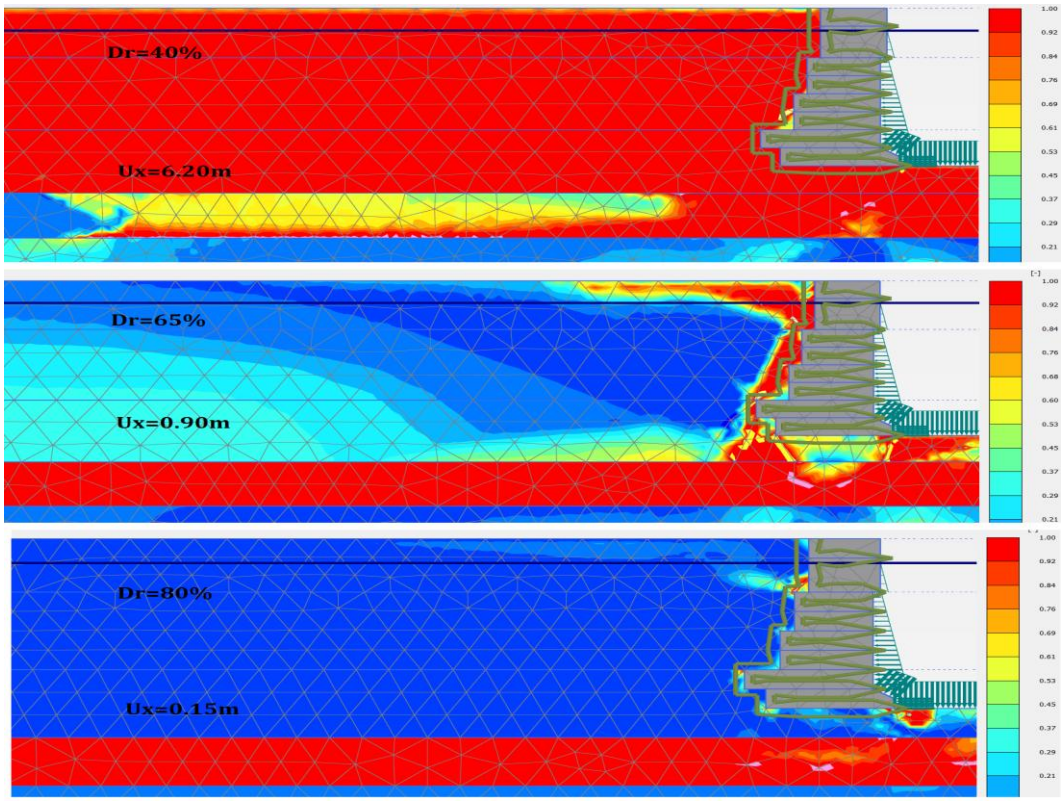

Figure 6.5: Contours of excees pore water pressure ratio, while relative density increases, for the same excitation (Erzincan, 1992 - 0.4g).

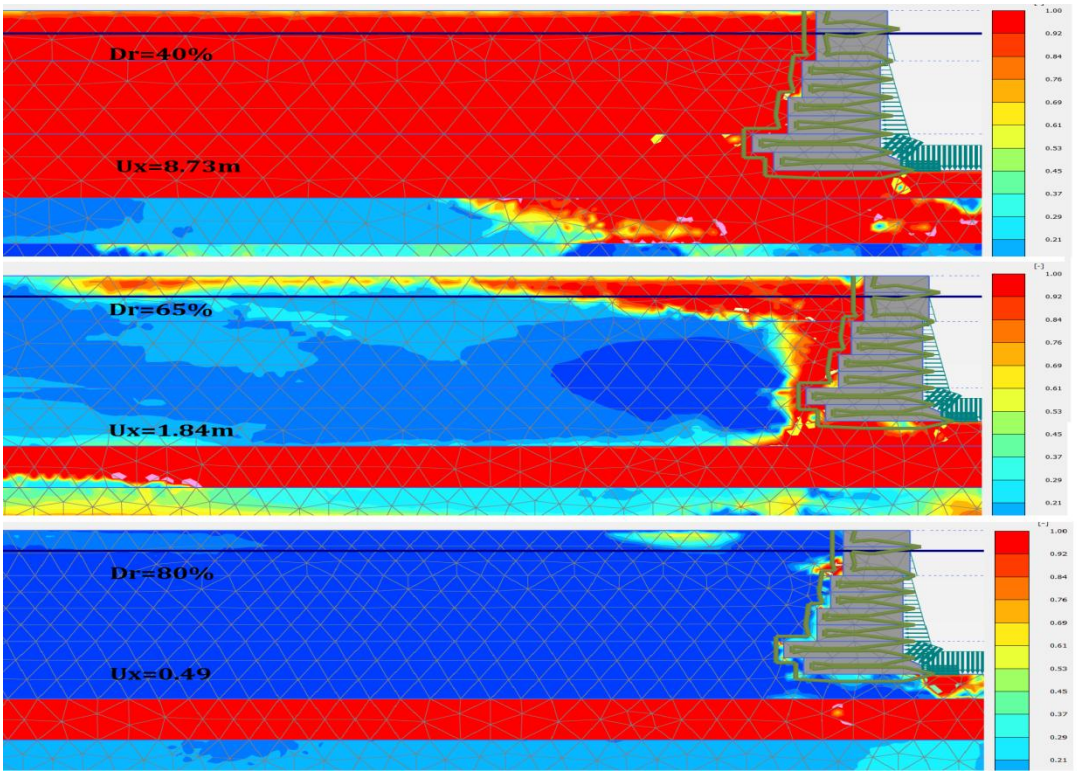

Figure 6.6: : Contours of excees pore water pressure ratio, while relative density increases, for the same excitation (Lefkada,2003 - 0.4g)

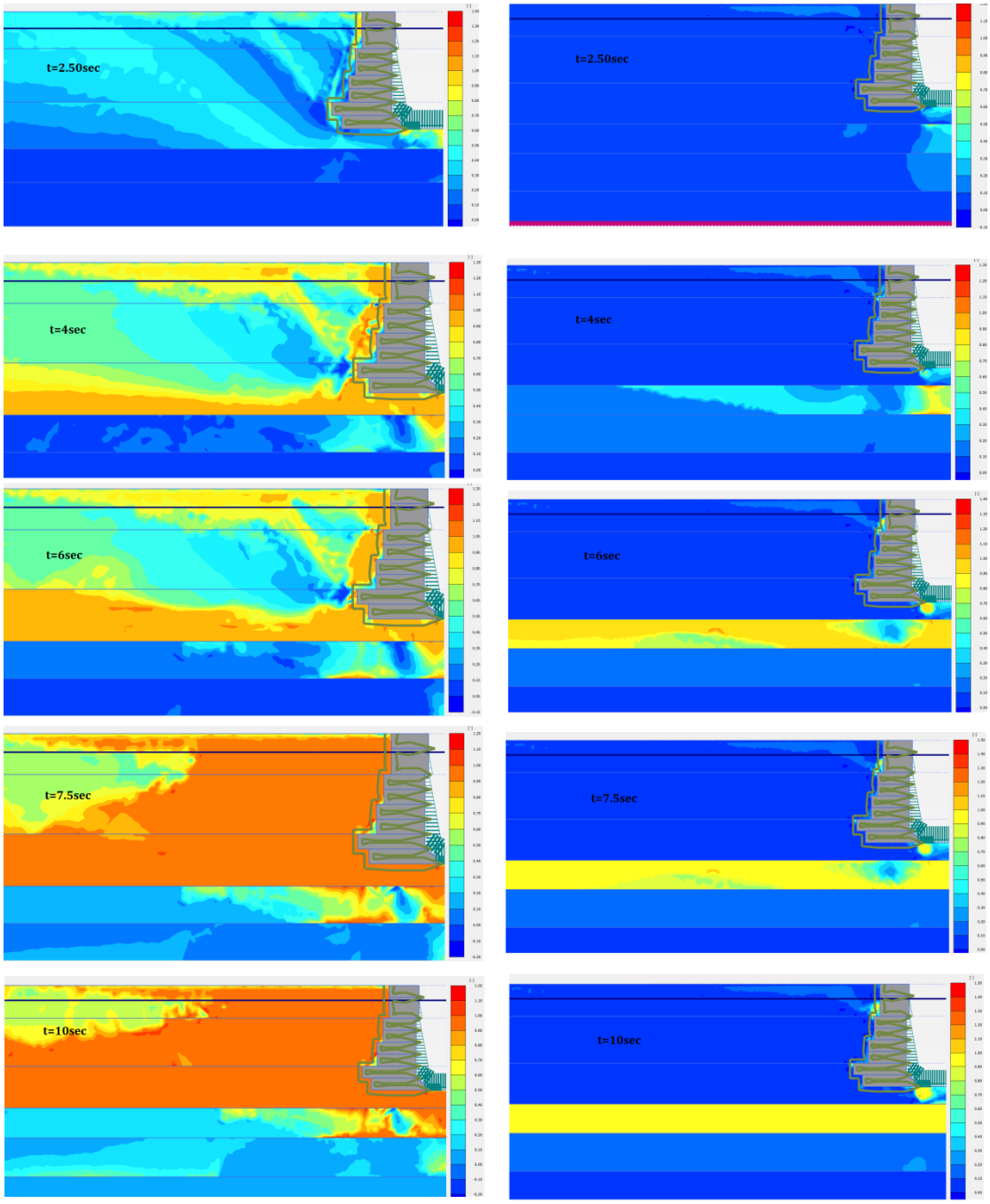

(a) (b)

Figure 6.6: Time history of excees pore water pressure ratio for backfill soil with (a) Dr=40% and (b) Dr=80% in Duzce-180_0.4g

6.2.4 Influence of excitation

The dynamic response of quay wall-soil also varied, at high rank, throughout the amplitude of accelograms. In all likelihood, it could be expected that, for the same earthquake, the reduction of excitation would produce the more detrimental displacements on quay wall the higher the value of peak ground acceleration would be. Nevertheless, in cases of backfill soil with Dr=40% and Dr=65%, diverse accelograms caused the largest horizontal diplacement and tilt when their maximum value was weakened at 0.2g, instead of demonstrating the highest at 0.4g or 0.6g. Representional examples of this paradox are the backfill soil with Dr=40% in Erzincan(1992) and backfill soil with Dr=65% in Izmit-Kocaeli(1999), which are portrayed in Figures 6.7 and 6.8 in relationship with the rise of acceleration amplitude.

This extraodinary phenomenon could be determined along with a more closer look at contours of excees pore water pressure ratio. In cases of maximum acceleration 0.1g and 0.2g liquefaction occures at backfill and foundation layer due to their loose relative density, with the already acquainted detrimental consequences . On the other hand, stronger seismic loads cause the below soil layer to lose their shear strenth and undergo liquefaction as well.

Hence, the retained soil layer is slightly isolated from the strong vibration and the extent of liquefaction is considerably expanded in a scale that the amplitude of strong shear waves is weakened. This is further confirmed by the recorded responce acceleration of the same point in amplitude 0.2g and 0.6 g of the same accelogram, as it is presented in Figure 6.9. Despite the fact that the base acceleration differs by 300%, the responce acceleration of free field it's almost equal in both cases for T=0, likewise for T =2, in 0.6g, the nonlinear behavior, due to liquefaction, becomes obvious with the amplification of acceleration to 0.55g.

Furthermore, considerably stong vibrations subject the soil to incurs liquefaction at initial stages of dynamic loading. Therefore, the energy, which is transfered by shear waves as inetria force to quay wall, is lowered.

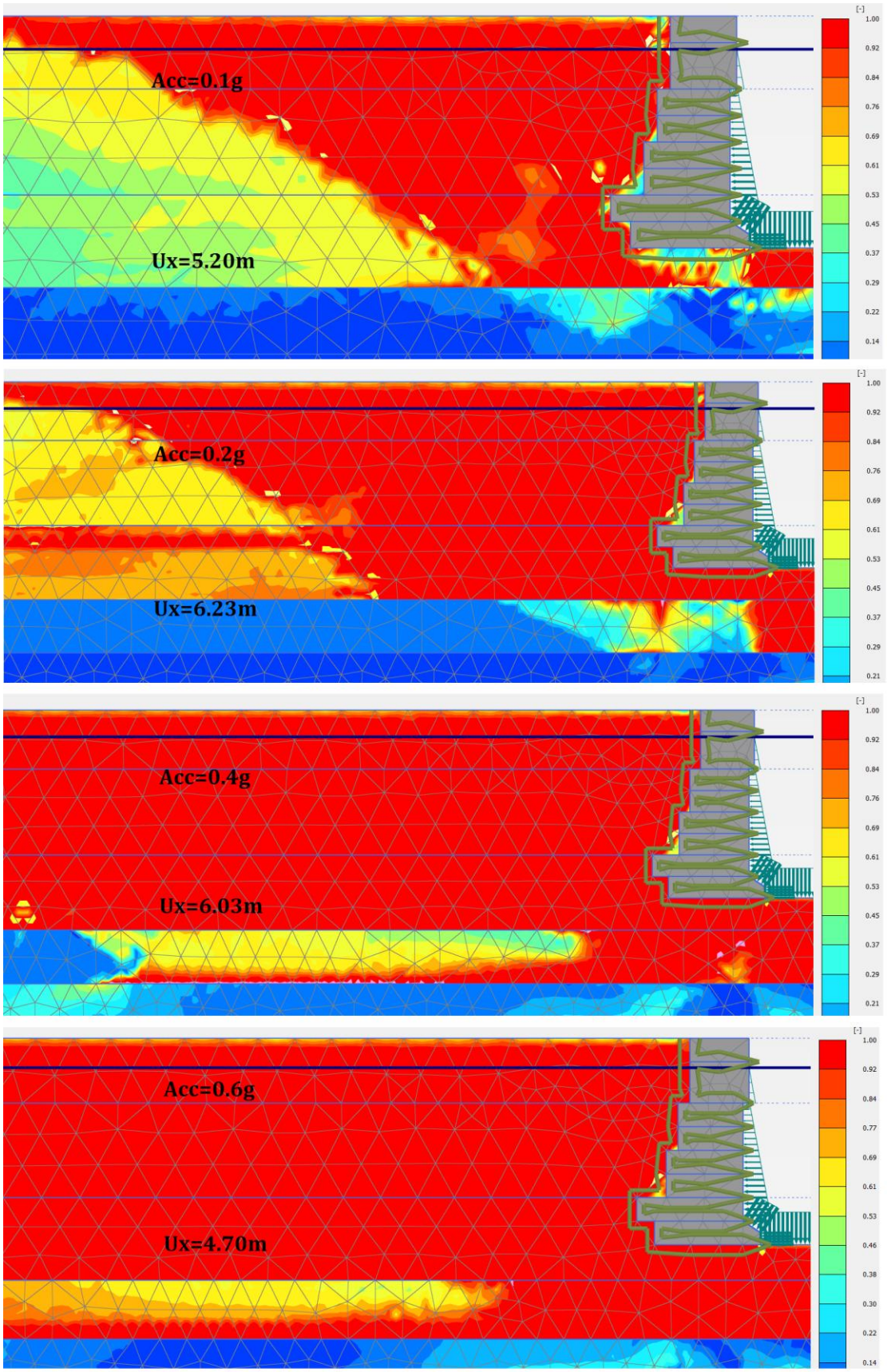

Figure 6.7: Contours of excees pore water pressure ratio, for relative density 40% (Erzincan, 1992).

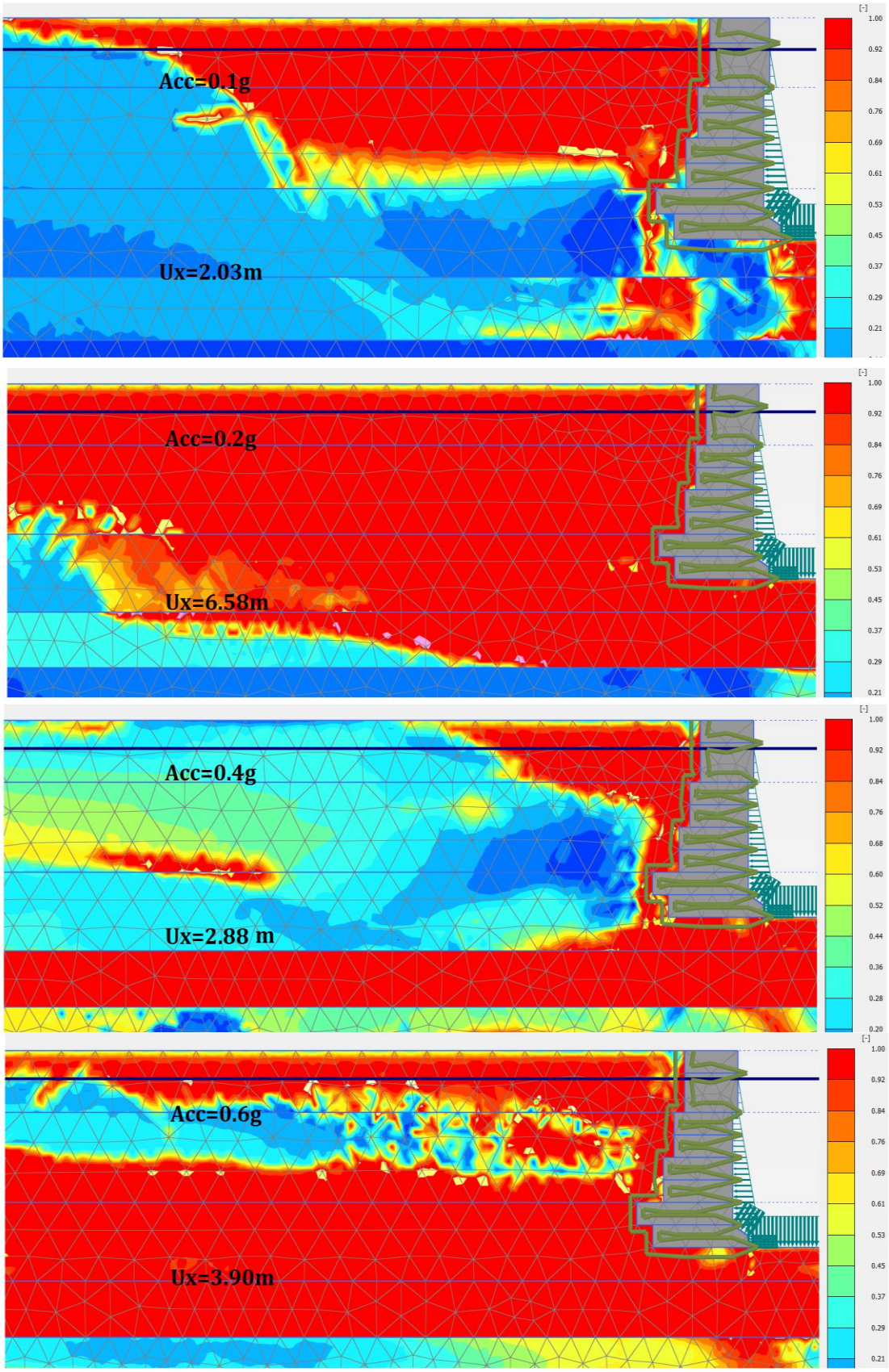

Figure 6.8: Contours of excees pore water pressure ratio, for relative density 40% (Izmit-Kocaeli,1999)

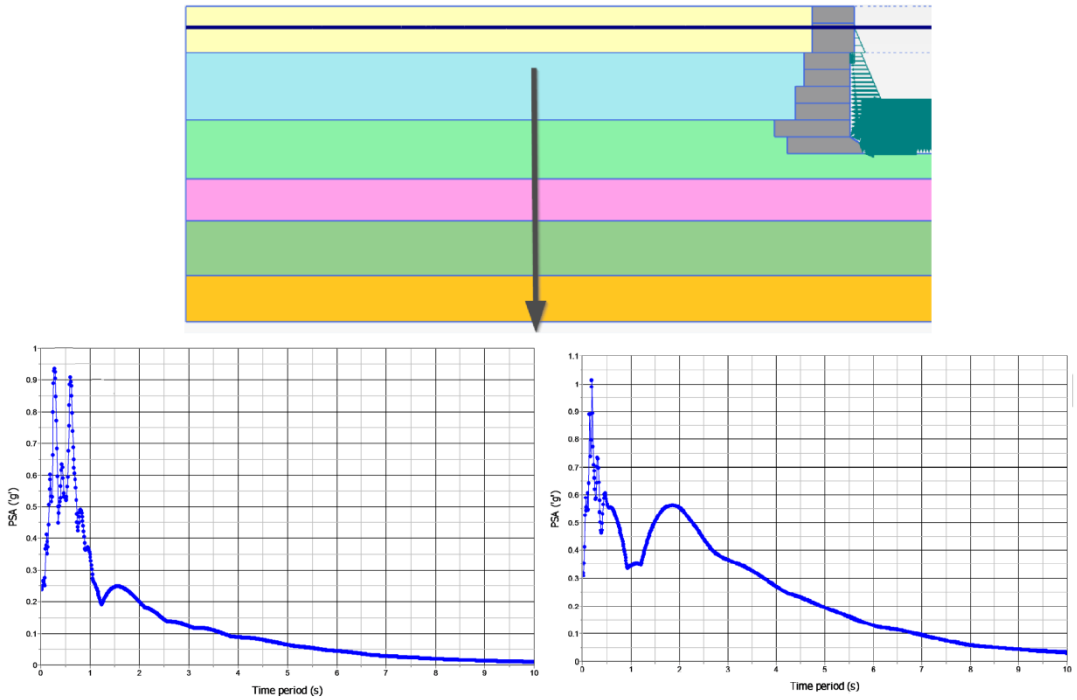

(a) (b)

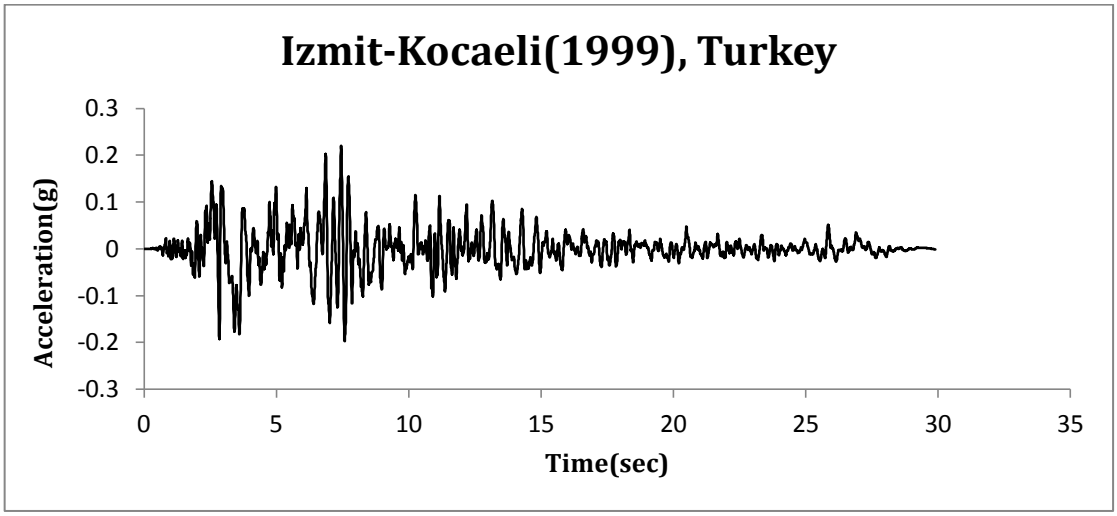

Figure 6.9: Responce acceleration of free field with Dr=65% for Izmit-Kocaeli(1999) (a) 0.2g and (b) 0.6g

6.3 General notes

6.3.1 Influence of boundaries' type

A commonplace boundary condition which is used for the dynamic stage of numerical modeling is the *Free field* boundaries. For operating reasons and for higher precision, this type of X-axis boundry should be accompanied with an elastic soil collumn next to them as Figure 6.10 displays. Investigating how they affect the deformations of the model, it is assumed that they overestimate quay wall's displacements over 10% , in comparison with *Tied degrees of freedom* boundary condition, as it is shown in figure 6.11. In order to consider a correlation between these two types of boundaries, the damping ration of *Free field* model was increased from 0.03 to 0.05. However, a notable difference has still remained (Figure 6.11)

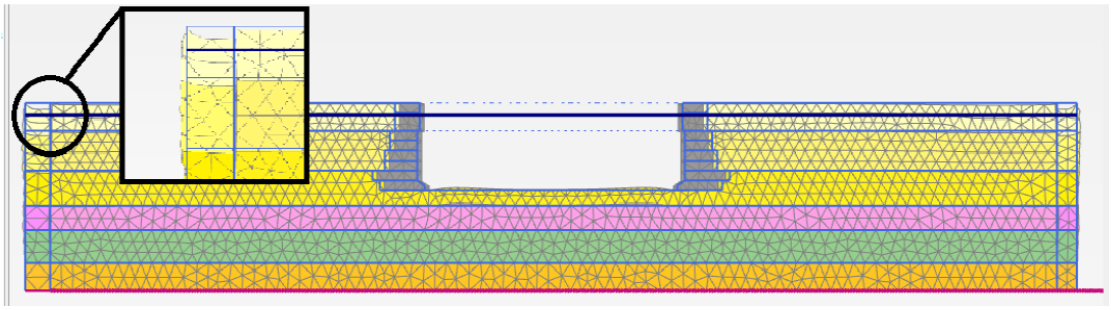

Figure 6.10: Free field procedure with soil column in the boundaries

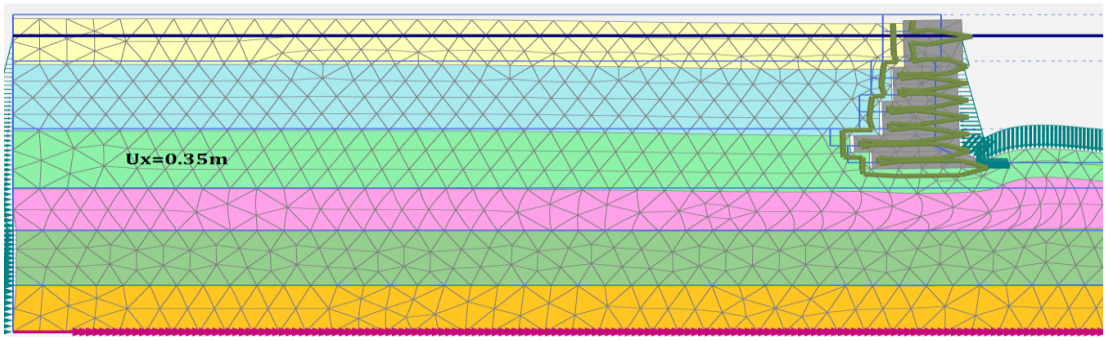

(a)

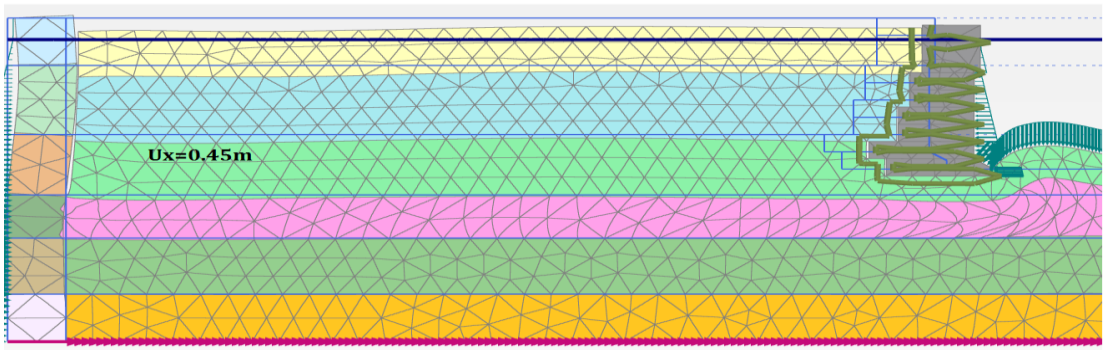

(b)

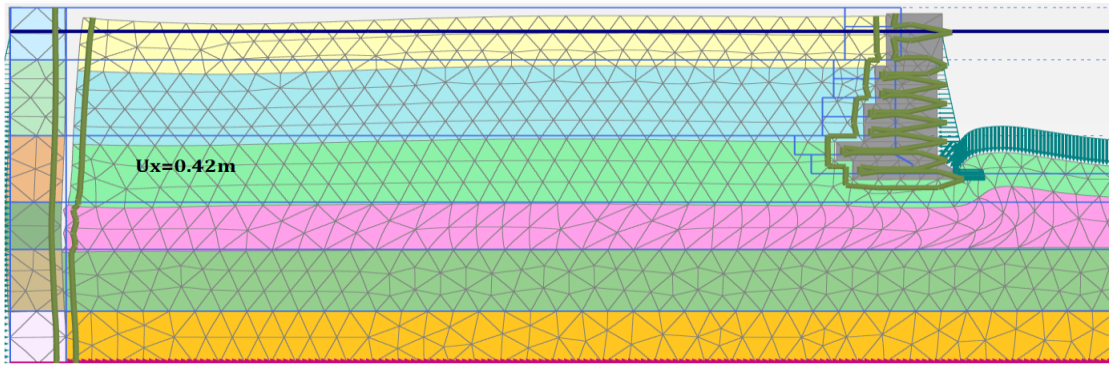

(c)

Figure 6.11: Analysis with (a) *Tied degrees of freedom* , (b) *Free field* with ξ=3% and (c) *Free field* with ξ=5% , boundaries in Kalamata_0.6g excitation

6.3.2 Quay wall's tilt for dense backfill soil

This Diploma Thesis does not conclude fragility curves for quay wall's tillt for backfill soil with relative density 80% because of their infinitesimal or, in many cases, negative-inward (Figure 6.12) value.

The cause which triggered the opposite rotation of quay wall was the strong amplitude of 0.6g. As it could be noticed from the time history of excess pore water pressure ratio, which is displayed in Figure 6.6 for dense backfill soils, the soil layer below the foundation layer is liquefied at the early stages of vibration, while the excess pore water pressure behind and in base of quay wall becomes negative. Therefore, quay wall is consider to be displaced horizontally - sliding lengthwise the silty sand layer - as it may rotated or not, depending on the undrained conditions (settlement on foundation-heaving in front of its toe).

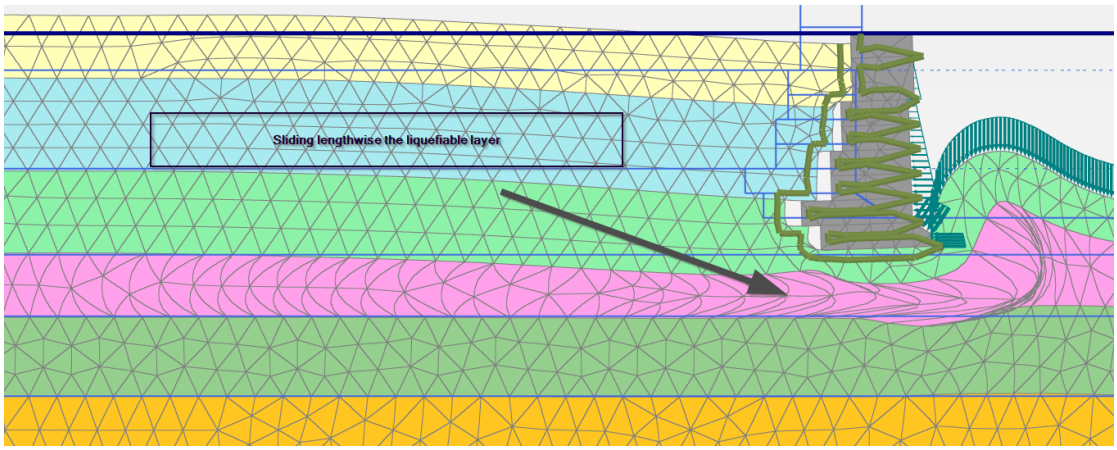

Figure 6.12: Example of quay wall's inward tilt in Izmit_0.6g earthquake

Chapter 7

Conclusion

Upon completing the numerical analyses and designing the fragility curves, for all the simulations of the dynamic interplay between the quay wall and the backfill soil, we summarise the following conclusions.

- The dynamic behaviour of gravity quay wall is a complicated phenomenon, which demonstrates significant differentiations in the residual displacements, referentially with the soil materials' relative density, the peak ground acceleration and the circles of loading.

- Materials with low relative density produced significant horizontal displacement and tilt on quay wall as it was expected. The combination of loose backfill soil and foundation layer, since they have the same properties, is considerably detrimental, as the developed displacements overcome all the allowance damage states.

- Loose materials evolve high possitive excess pore water pressures, which trigger liquefaction initially in the free field and in the foundation of quay wall. The range of liquefaction is expanded, with the circles and the amplitude of loading, in a large area behind the quay wall and in the silty sand below the backfill. While the relative density increases from a loose to a dense soil for the same excitation, the range of liquefaction is moderated, likewise it is contained only in silty sand for Dr=80%

- The provenance of the quay wall's displacements is profoundly connected with the backfill soil's relative density. The highest values of its horizontal displacement and tilt are forced by the significant deformation of the liquefiable soil behind the quay wall and the compliant foundation soil. On the other hand, the lowest values comes from the horizontal displacement of silty sand, which is the only liquefiable layer in cases with Dr =80%. Quay wall, apparently, sliding on silty sandy and occasionally is rotated inwards, especially for amplitudes of 0.6g.

- The amplification of peak gound acceleration, in loose soils, occures more intensively for ground motions with maximum acceleration 0.1g and 0.2g. Stronger amplitudes of 0.4g and 0.6g cause significant strains, mainly, in the surface soil layers and therefore their responce value is weakened.

References

Abdollah Shafieezadeh, seismic vulnerability assessment of wharf structures

Alyami M, Rouainia M, Wilkinson SM, Numerical analysis of deformation behaviour of quay walls under earthquake loading

Atsushi NOZU, Koji ICHII, and Takahiro SUGANO seismic design of port structures

BrajaM. Das G.V.-Ramana Principles of Soil-Dynamics Second Edition 2010

Byrne P. M. & Park S.S., Beaty M.: Seismic liquefaction: centrifuge and numerical modeling

Gazetas G., Dakoulas P., Anastasopoulos I.: Failure of Harbor Quaywalls in the Lefkada 14-8-2003 Earthquake

Gazetas G., Dakoulas P., Anastasopoulos I.: Failure of Harbor Quaywalls in the Lefkada 14-8-2003 Earthquake

Gazetas G., Garini E. (2014): Notes, Sliding Rocking Soil Dynamics

H. Heidary Torkamani*, K. Bargi, R. Amirabadi, Fragility Curves Derivation for a Pile-Supported Wharf

Kramer S. L. (1996): Geotechnical Earthquake Engineering

Panagiota Tasiopoulou Nikos Gerolymos Takashi Tazoh and George Gazetas, Pile-Group Response to Large Soil Displacements and Liquefaction: Centrifuge Experiments versus a Physically Simplified Analysis

Panagiota TASIOPOULOU, Nikos GEROLYMOS and George GAZETAS Seismic effective stress analysis of gravity block type quay walls: application to piraeus port

PIANC, (World Association for Waterborne Transport Infrastructure): Seismic Design Guidelines for Port Structures

PLAXIS Liquefaction Model UBC3D-PLM

PLAXIS2D, 2014, Reference Manual

PLAXIS2D, 2014, Scientific Manual

PLAXIS2D, Knowledge Base: http://kb.plaxis.com/tips-and-tricks/use-dynamic-boundary-conditions

Rebecca L. Johnson, Theory of Response Spectrum Analysis

H. Karakus , A. Ergin , I. Guler , K. Cihan and Y. Yuksel Dynamic response of block type quay wall